Exploring Magnetic Collective modes and 2D Heterostructures with Raman

Yiping Wang

A dissertation

submitted to the Faculty of

the department of Physics

in partial fulfillment

of the requirements

for the degree of

Doctor of Philosophy

Boston College

Morrissey College of Arts and Sciences

Graduate School

May 2022

Exploring Magnetic Collective modes and 2D Heterostructures with Raman

Yiping Wang

Advisor: Kenneth S. Burch, Ph.D., D.Sc.

In quantum materials, quantum mechanical effects survive over a wide range of temperatures and length scales, which leads to fascinating phenomena, such as charge density waves, spin liquids, and magnetism. These remarkable properties originate from a delicate balance among many interacting degrees of freedom. Even small perturbations such as temperature and doping can induce many diverse phases and colossal changes in the materials' functionalities. It remains a mystery how to detect these novel phenomena without complicated fabrication and extreme conditions.

This thesis contributed to this field by studying collective modes in quantum materials via inelastic light scattering. After fabricating the devices in a glovebox, we directly transfer them to the measurement platform under a high vacuum. Using Raman spectroscopy, a new quasi-particle–axial Higgs mode in charge density wave systems was discovered and further symmetry breaking accompanied with it suggests the charge density wave is unconventional. In addition to symmetry analysis breakthroughs, this thesis also provided direct evidence of the fractional nature as well as the energy and temperature limits of Kitaev interactions in quantum spin liquid candidate systems, which is the building block for topological quantum computers. Not limited to 2D Kitaev materials, the non-Fluery-Loudon single magnon scattering process was detected in a 3D Kitaev system. Other than using Raman to probe the fundamental nature, we also employed it to reveal, for the first time, a clean way to realize modulation doping in 2D materials, where the acceptor carrier density has reached 10^{14} cm^{-2}. This method can be applied to dope magnetic materials or twisted heterostructures to find new phases.

Dedicated to all the people that are still following their dreams.

TABLE OF CONTENTS

LIST OF FIGURES

Figure

LIST OF ABBREVIATIONS

QSLs Quantum spin liquids

CDW Charge density wave

a.u. arbitrary units

QMC Quantum Monte Carlo

TEM Transmission Electron Microscope

JDos Joint density of states

SW spectral weight

QES quasi-elastic scattering

mlg monolayer graphene

blg bilayer graphene

MINT mismatched interface theory

CHAPTER I

Introduction

Quantum materials have an explossive progress in the past decades and play an important role in condensed matter physics. These systems contributes to uncover many novel phenomena, such as new phases and applications of new generation photonic and electronic devices. However, the properties of quantum materials are extremely sensitive to external stimuli. The interactions of spin, charge, lattices and quantum pathways can be changed/affected during the fabrication or extreme experimental conditions, such as high magnetic field or electric bias.

This thesis aims to contribute to the long term goal- detecting new emergent quantum phases and their properties without extreme external stimuli. In spite of these, a intriguing route is studying collective modes in quantum materials.

Without complicated fabrication and external extreme conditions, Raman scattering, since its first discovery, is an indispensable tool in condensed matter physics. In fact, Raman scattering provides one of the most convenient way to probe elementary excitations, such as phonons, magnons, plasmons, anynons and electronic excitations in both bulk and Van der Waals materials.

The scattering process occurs mainly through virtual intermediate electronic transitions and the scattering energy are determined by the difference of incident and scattering light frequency. Depending on the pathways to the intermediate states and cross section,

one can detect the symmetry/energy of phonons, magnons and electronic excitations. In addition to that, the excited particles can form fractionalized quasi-particles in specific frustrated magnetic states.

This thesis has been focused on using Raman to study the fundamental properties of electronic scattering, novel magnetic phases as well as their use in potential applications.

In chapter 2, we investigate the scattering light pathway interference and for the first time discover the axial Higgs mode in CDW system RTe_3.In RTe_3 (R=La,Gd), the electronic ordering couples bands of equal or different angular momenta. As such, the Raman scattering tensor associated to the Higgs mode contains both symmetric and antisymmetric components that are excited via two distinct, but degenerate pathways. This leads to constructive or destructive interference of these pathways, depending on the choice of the incident and Raman scattered light polarization. The qualitative behaviour of the Raman spectra is well-captured by an appropriate tight-binding model including an axial Higgs mode. Elucidation of the antisymmetric component is direct evidence that the Higgs mode contains an axial vector representation (i.e. a pseudo-angular momentum) and hints the CDW in RTe_3 is unconventional. Thus we provide a means for measuring collective modes quantum properties without resorting to extreme experimental conditions.

In chapter 3, we report the magnetic fractional excitation in spin liquid systems. We identify the energy and temperature boundaries of non-Kitaev interactions by direct comparison of the Raman susceptibility of α-$RuCl_3$ with quantum Monte Carlo (QMC) results for the Kitaev QSL. Moreover, we further confirm the fractional nature of the magnetic excitations, which is given by creating a pair of fermionic quasiparticles. Interestingly, this fermionic response remains valid in the non-Kitaev range. Our results and focus on the use of the Raman susceptibility provide a stringent new test for future theoretical and experimental studies of QSLs.

In chapter 4, measurements of the modulation doping in Van der Waals heterostruc-

tures are discussed. Our Raman, photovoltage, and electrical conductance measurements combined with ab initio calculations establish the large work function and narrow bands of α-$RuCl_3$ enable modulation doping of exfoliated single and bilayer graphene, chemical vapor deposition grown graphene and WSe2, and molecular beam epitaxy grown EuS. We further demonstrate proof of principle photovoltage devices and charge transfer through hexagonal boron nitride. Short-ranged lateral doping (<65 nm) and high homogeneity are achieved in proximate materials with a single layer of α-$RuCl_3$. This leads to the best-reported monolayer graphene mobilities (4900 cm2/(V s)) at these high hole densities (3 × 10^{13} cm^{-2}) and yields larger charge transfer to bilayer graphene (6 × 10^{13} cm^{-2}).

In chapter 5, we focus on the Raman scattering of bulk Kiteav QSL system β-Li_2IrO_3. The spectra exhibit a coexistence of a broad scattering continuum and two sharp low-energy peaks at 2.5 meV and 3 meV, with a distinctive polarization dependence. While the continuum is suggestive of fractional quasi-particles emerging from a proximate quantum spin liquid phase, the sharp peaks provide the first experimental signature of the 'non-Loudon-Fleury' one-magnon scattering processes proposed recently.

CHAPTER II

Axial Higgs mode in charge density wave

2.1 Introduction

The observation of the Higgs boson solidified the standard model of particle physics. However, explanations of anomalies (e.g. dark matter) rely on further symmetry breaking calling for an undiscovered axial Higgs mode[1]. In condensed matter the Higgs was seen in magnetic, superconducting and charge density wave(CDW) systems[2, 3]. Uncovering a low energy mode's vector properties is challenging, requiring going beyond typical spectroscopic or scattering techniques. Here, we discover an axial Higgs mode in the CDW system RTe_3 using the interference of quantum pathways. In RTe_3 (R=La,Gd), the electronic ordering couples bands of equal or different angular momenta[4–6]. As such, the Raman scattering tensor associated to the Higgs mode contains both symmetric and antisymmetric components, which can be excited via two distinct, but degenerate pathways. This leads to constructive or destructive interference of these pathways, depending on the choice of the incident and Raman scattered light polarization. The qualitative behaviour of the Raman spectra is well-captured by an appropriate tight-binding model including an axial Higgs mode. The elucidation of the antisymmetric component provides direct evidence that the Higgs mode contains an axial vector representation (i.e. a psuedo-angular momentum) and hints the CDW in RTe_3 is unconventional. Thus we provide a means for measuring collective modes

quantum properties without resorting to extreme experimental conditions.

Emergent order states bring about new modes whose properties are directly linked to the associated change in topology or symmetry breaking. A well studied example is the breaking of translation symmetry in CDW systems resulting in Nambu-Goldstone (phase) and Higgs (amplitude) modes. In a superconductor the inclusion of electromagnetism results in a gapping of the phason or giving mass to the W and Z bosons of the electroweak theory. However this Anderson-Higgs mechanism leaves the amplitude mode largely unchanged, and thus by convention it is often referred to as the Higgs boson.[2, 3, 7] Despite its close resemblance to superconductivity and first prediction in 1955, all CDW to date have revealed s-wave condensation with a scalar Higgs mode. The challenge in detecting unconventional order is the requirement to probe the vector nature of the order parameter or collective excitations. One example is the attempt to extend the standard model by enlarging the symmetry breaking. This results in additional particles, including a spin-1 Higgs boson, and dark matter candidates.[1] Thus the detection of a Higgs mode with finite angular momenta (i.e. an axial Higgs) heralds the discovery of a heretofore undiscovered symmetry breaking and novel phase of matter.

Pathway interference is an elegant tool to meet this challenge by exploiting wave-particle duality to uncover the hidden quantum properties of excitations[8]. In condensed matter quantum pathway interference revealed the topological properties of band structures[9, 10], unconventional superconducting order[11–13], and the nontrivial statistics of collective excitations[14–16]. Despite the elegance of such experiments, they have not been directly applied to the Higgs mode to uncover its axial vector nature. In part, this results from the challenge of performing quantum interference in condensed matter settings, which typically require extreme experimental conditions: low temperatures, ultrafast lasers, high magnetic and/or electric fields. The need for such conditions could be overcome by CDW systems, with well defined Higgs and phase modes readily observed with optical techniques at large energy scales[5, 17–22]. Furthermore, the CDW can be

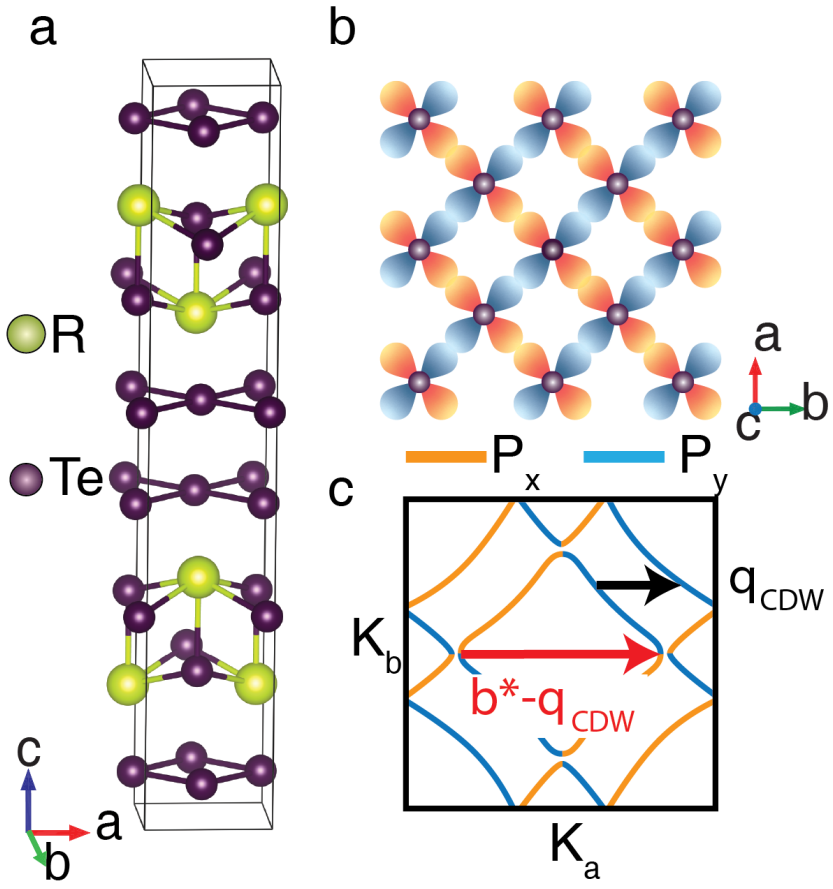

Figure 2.1: (a) RTe_3 crystal structure and unit cell (black line). (b) P_X (orange) and P_y (blue) orbitals in the Te layer. (c) Fermi surface with orbital content labeled by the same colors as in (b). The red arrow indicates the CDW vector (q_{CDW}) with the black arrow indicating the second nesting condition with the reciprocal lattice vector ($b^* - q_{CDW}$)

tuned by pressure, exfoliation, or ultrafast lasers[23–26] while offering next generation nano oscillator, logic and memory devices[27].

2.2 Methods

2.2.1 Crystal Growth

High-quality RTe_3 single crystals were grown in an excess of tellurium (Te) via a self flux technique. Te (metal basis $> 99.999\%$, Sigma-Aldrich) was first purified to remove oxygen contaminations and then mixed with the rare-earth ($> 99.9\%$, Sigma-Aldrich) in a ratio of 97:3. The mixture was sealed in an evacuated quartz ampoule and heated to 900 C over a period of 12 hours and then slowly cooled down to $550°C$ at a rate of $2°C/hour$. The crystals were separated from the flux via centrifugation at $550°C$

2.2.2 Sample Preparation and Vacuum Transfer

$GdTe_3$ and $LaTe_3$ flakes were exfoliated and characterized using unpolarized Raman in an Argon glovebox. Then they were loaded into a 10^{-6} mbar vacuum suitcase and directly transferred into a low temperature cryostat[28].

2.2.3 Angle Resolved Raman Spectroscopy

The 532nm Raman experiments were performed with a custom built, low temperature microscopy setup[29]. A 532 nm excitation laser, whose spot has a diameter of 2 μm, was used with the power limited to 10 μW to minimize sample heating while allowing for a strong enough signal. At both room and base temperature (10K), the reported spectra were averaged from three spectra in the same environment to ensure reproductability. The spectrometer had a 2400 g/mm grating, with an Andor CCD, providing a resolution of ≈ 1 cm^{-1}. Dark counts are removed by subtracting data collected with the same integration time with the laser blocked. Freshly cleaved sample is transferred to a

cryostat with optical window and pumped down to a vacuum level of 10^6 torr. The 488 nm (2.54 eV) emission line from an Argon laser is used as the excitation source. The incident laser is reflected by a 90/10 nonpolarizing cube beam splitter and then focused to a spot size of 2 μ m on the sample using a 50× objective lens (NA, 0.35). The laser power on the sample is 700uW. The incident beam and collected optical signal are linear polarization resolved using a combination Fresnel rhomb retarders and linear polarizers. Raman signal is dispersed by a Horiba T64000 spectrometer equipped with 1800g/mm gratings and and detected with a liquid-nitrogen-cooled CCD camera. We used fresnel rhomb to measure the angular dependent Raman spectra in both setup.

2.3 Raman results of Axial Higgs mode

Here we study quantum pathway interference of the axial Higgs mode to reveal the unconventional CDW phase in RTe_3. This is achieved at room temperature with Raman scattering as it can measure the energy, symmetry, and excitation pathways of fundamental modes[30–33]. We build upon previous inelastic light scattering experiments in non-interacting systems revealed the chiral nature of phonons, molecular crystal field excitations, semiconductor interband transitions, and changes in quantum pathway or coherence upon gating[34–37]. For these previous single particle experiments, the intermediate states (i.e. quantum pathways) are chosen by the combination of excitation wavelength, momentum conservation, the polarization of the incoming and outgoing light via selection rules[38, 39].

We focused on the rare earth CDW system RTe_3 (R = Gd,La) exploiting its high transition temperatures ($T_{CDW}^{Gd} = 380$ K, $T_{CDW}^{La} > 600$ K), unidirectional CDW, and multiple nesting conditions, enabling quantum pathway selection. The RTe_3 crystal structure consists of double layers of van der Waals bonded square-planar Te sheets separated by RTe slabs (Fig. 2.1a), crystallized in an orthorhombic structure with the space group Bmmb. RTe_3 is nearly tetragonal ($a - b \approx 0.01$Å)[6, 40]. The Bloch

bands near the Fermi energy are mainly composed of the P_X and P_Y orbitals of the tellurium sheet (Fig. 2.1b) as the P_Z orbital is much lower in energy. Since the RTe_3 slab is less densely packed within the ab plane, the chosen unit cell (c.f., Fig. 2.1a) results in the Fermi surface shown in Fig.2.1c, where hybridization between the two orbitals happens only at isolated points due to next-nearest neighbour interaction [41]. The incommensurate q_{CDW} determined by various techniques is $(2/7)b^*$, where b^* is the reciprocal lattice vector, consistent with nesting between the original P_X derived band of the Te sheet and the P_X band folded in due to the enlarged unit cell of the 3D structure[4, 5]. In addition, another nesting condition arises when accounting for the reciprocal lattice vector, where $b^* - q_{CDW}$ connects $P_X(P_Y)$ to $P_Y(P_X)$ derived bands. Due to the orthorhombicity, these nesting conditions are not satisfied along the a-axis, resulting in a node in the CDW gap, suggesting an unconventional order. Similarly the requirement to change angular momenta when connecting the P_X to P_Y states with $b * -q_{CDW}$ suggests the Higgs mode has finite angular momenta. The interference between the two pathways associated with this mode, the possible axial nature of the Higgs, change in sign of the gap (i.e. p-wave order) and thus unconventional CDW order have yet to be explored theoretically or experimentally.

2.3.1 Raman spectra at different polarization configuration

As seen in Fig. 2.3(a-b), the intermediate states have either the same or different angular momenta and thus follow different selection rules. The selection rules depend sensitively on polarization relative to the crystal axis, presence of single domains and clean surfaces. We achieved this with exfoliated RTe_3 flakes produced in a glovebox and rapidly transferred via vacuum suitcase to our low T Raman system. This ensured the sample surface is free from oxide contamination, atomically flat, contained single CDW domains and enabled identification of the crystal axes using the sharp edges (confirmed via TEM – see supplemental).

With this in mind, we turn to the polarization dependent Raman spectra of the Higgs mode. Fig. 2.2 shows representative measurements using a 532 nm excitation of $GdTe_3$ at 300K in both parallel and cross polarization configurations. Here ab(XY 0^o) refers to the incident (scattered) light polarized along the crystal a(b)-axis. Similarly, a'b'(XY 45^o) represents the crystal rotated by 45 degrees from the ab configuration, where a' = a+b, b' = a-b. The 5 meV broad peak is the CDW Higgs mode and all other sharp peaks are the phonons.

The Higgs mode partially overlaps with the phonons in the shaded energy region. As seen in (Fig. 2.2), both the phonons and Higgs mode are observed in parallel polarization along aa (XX 0 deg), bb (XX 90deg) or a'a'(XX 45deg) directions. As expected and typically observed, the phonon modes have the same intensity when the configuration is changed from a'b' (XY 45deg) to b'a'(XY 135deg). Indeed, the measured Raman intensities (I) for a given excitation are proportional to the square of the product of incident light polarization ($\hat{e}_i$), Raman tensor (R) and the scattered electric field ($\hat{e}_f$): $I = |\hat{e}_i \cdot R \cdot \hat{e}_f|^2$. However, as seen in the shaded region of (Fig.2.2), the scattering intensity of the CDW Higgs mode behaves quite differently, it is strong in a'b' but dramatically reduced in b'a'. Other than the CDW Higgs mode, phonons coupling with CDW mode at 7.4 meV and 10.6 meV also showed the intensity difference at a'b' and b'a' polarization. As previously established in X-ray measurement, the Higgs mode is strongly mixed with these phonons[42] and they disappear above CDW transition temperature[41].

2.3.2 Raman scattering pathway analysis

To understand the change in the Higgs mode intensity upon swapping the incident and scattered polarization, it is useful to consider the role of the CDW in the quantum pathways in RTe_3. From symmetry, the possible inelastic, $q \approx 0$ excitations must fall in one of the irreducible representations $\Gamma_{\text{Raman}} = 3A_g + B_{1g} + B_{2g} + B_{3g}$ leading

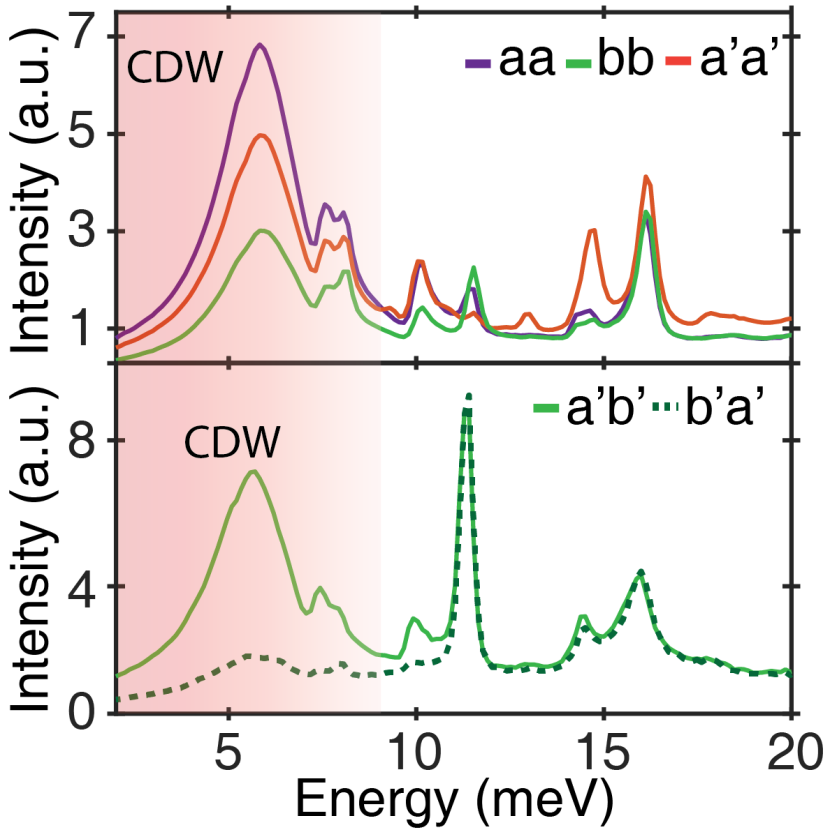

Figure 2.2: 300K Raman spectra of $GdTe_3$. Top plot is taken in parallel linear polarization, with incident and scattered light aligned with different crystal axis. The Higgs mode is shaded. The bottom plot is taken in cross linear polarization, for incident light aligned with the a'(45 deg off a-axis) direction and scattered light along b'(45 deg off a-axis) direction (green solid line). Upon swapping the incident and scattered polarization (dashed line), the response of all phonons modes is identical, while the amplitude mode is suppressed.

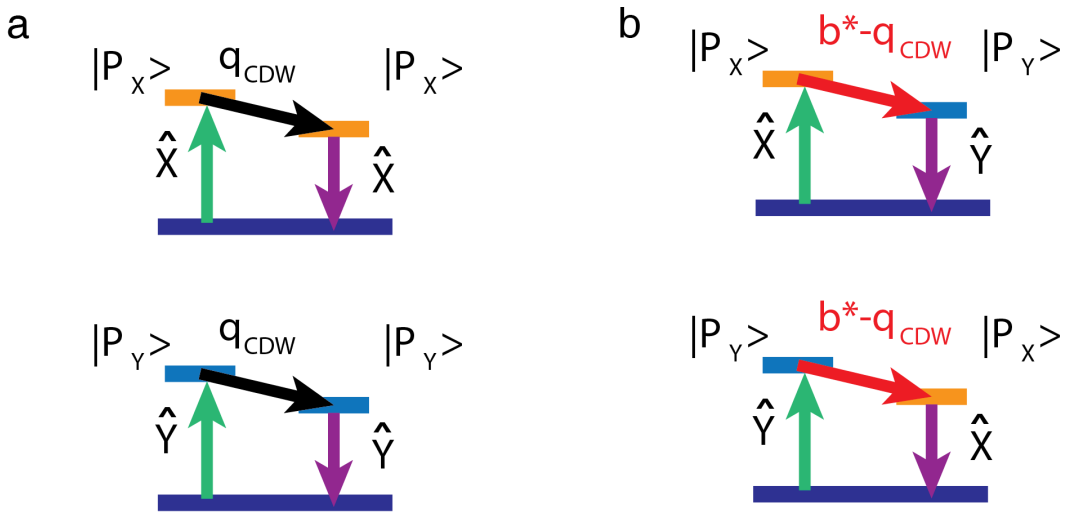

Figure 2.3: (a) CDW involved symmetric Raman scattering process. (b) CDW involved anti-symmetric Raman scattering process.

to a symmetric Raman tensor ($R_{ij} = R_{ji}$)[43]. As seen in Fig. 2.5 and2.6, this produces a four-fold angular dependence of the phonon modes intensity. However, due to the periodicity of the CDW, there are two quantum pathways that involve different intermediate states separated by $|q_{CDW}|$ or $|b^* - q_{CDW}|$ (see Fig. 2.1c, 2.3a and b). In the first, an $X(Y)$ polarized incident photon excites the electron into an intermediate state $|P_X\rangle(|P_Y\rangle)$, which is scattered to the $|P_X\rangle$ ($|P_Y\rangle$) state by the Higgs mode with wave vector q_{CDW}. Subsequently, the electron recombines with a hole and emits an $X(Y)$ polarized photon. Such a process results in a symmetric response as it involves scattering between states with identical polarization. While the symmetric response could be a Raman tensor with the form of A_g, B_g or a sum of the two, in fitting the angular dependent Higgs mode susceptibility, we find that the off-diagonal symmetric terms (B_g vertex) are nearly zero.

The second scattering pathway involves a Higgs mode connecting $|P_X\rangle(|P_Y\rangle)$ to states with different angular momenta $|P_Y\rangle(|P_X\rangle)$ via $|b * -q_{CDW}|$. The change in

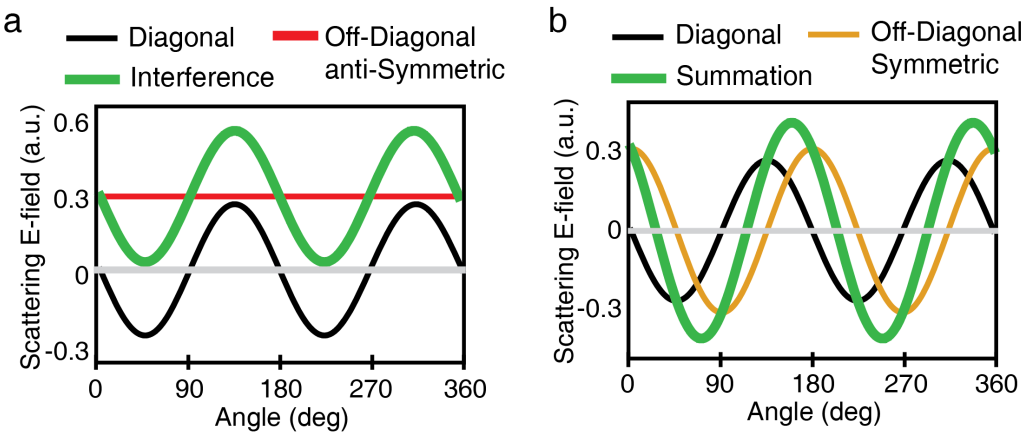

Figure 2.4: (a) Scattered electric field resulting from quantum interference of a diagonal (R_{ii}) and antisymmetric off-diagonal ($R_{ij} = -Rji$) Raman processes. (b) Scattered electric field resulting from quantum interference of a diagonal (R_{ii}) and symmetric off-diagonal ($R_{ij} = Rji$) Raman processes. The presented angle is the polarization rotation angle relative to the crystal a-axis.

angular momenta of the states associated with this nesting vector suggests that the Higgs mode is unconventional, requiring an axial vector representation. Nonetheless, upon recombination, a Y (X) polarized photon is produced. Noting that the excitation from the $|P_Z\rangle$ band to $|P_X\rangle$ or $|P_Y\rangle$ bands matches the visible excitation laser energy,[5] the Higgs mode is a resonant electronic response. This resonance combined with the angular momentum change induces a nonzero antisymmetric (i.e. $R_{ij} = -R_{ji}$) contribution to the Raman tensor [34], which by itself would produce a signal only in XY and not XX configurations. Ultimately it is the interference of this antisymmetric process with the symmetric, diagonal component that produces the two-fold response in the cross-polarized Raman. In the supplemental material we calculate the Raman susceptibility from resonant processes using a low energy model in the presence of a CDW gap and amplitude mode and find an asymmetric transition, depending on the chosen pathway. This asymmetry primarily comes from the points in the Fermi surface with nesting vector $b * -q_{CDW}$ and is enhanced by the orbital mixing due to next-nearest neighbour

interaction [41]. Fitting to the experimental data we arrive at a Raman tensor for the Higgs mode:

$$R_{CDW} = \begin{pmatrix} 0 & d & 0 \\ -d & 0 & 0 \\ 0 & 0 & 0 \end{pmatrix} + \begin{pmatrix} e & 0 & 0 \\ 0 & f & 0 \\ 0 & 0 & g \end{pmatrix} = \begin{pmatrix} e & d & 0 \\ -d & f & 0 \\ 0 & 0 & g \end{pmatrix}$$

, where d, e, f, g are independent coefficients. The detailed calculations of the angular dependence of the Raman response are shown in the supplemental but we briefly describe the key results here. The $|P_X\rangle \rightarrow |P_X\rangle$ pathway gives the same response for a'b' and b'a' configurations: $I = |(e-f)|^2$. However, $|P_X\rangle \rightarrow |P_Y\rangle$ pathways give $I = |2d|^2$ under a'b' polarization and $I = |-2d|^2$ under b'a' polarization. As such if the two pathways did not interfere (i.e. we add their intensities) we would not observe any difference when swapping the incident and scattered polarization (i.e. four-fold response of Raman vertex diagonal term and off-diagonal symmetruc term - Fig.2.5). However the indistinguishablity and thus pathway interference leads to the CDW intensity $I_{a'b'} = |(e-f)+2d|^2$ producing the constructive interference term and $I_{b'a'} = |(e-f)-2d)|^2$ the destructive interference term, and thus a purely two fold angular response in cross-polarized Raman (2-fold response of Raman vertex diagonal term and off-diagonal anti-symmetric term Fig.2.4).

To reveal the suggested quantum interference of pathways, we focus on the angular dependence of the Raman response. The colormaps in Fig.3a and b present parallel and cross polarization data and the green lines are the selected spectra in Fig.2.2. The shaded region indicates the response from the Higgs mode. Consistent with quantum interference, these maps clearly show the Higgs mode has a two fold response. To examine in detail the Higgs and phonon mode angular dependence, we plot the intensity versus crystal angle for representative phonons of A_g and B_g symmetry alongside the response from the Higgs mode (Fig.2.6,2.7). In the supplemental material we derive the

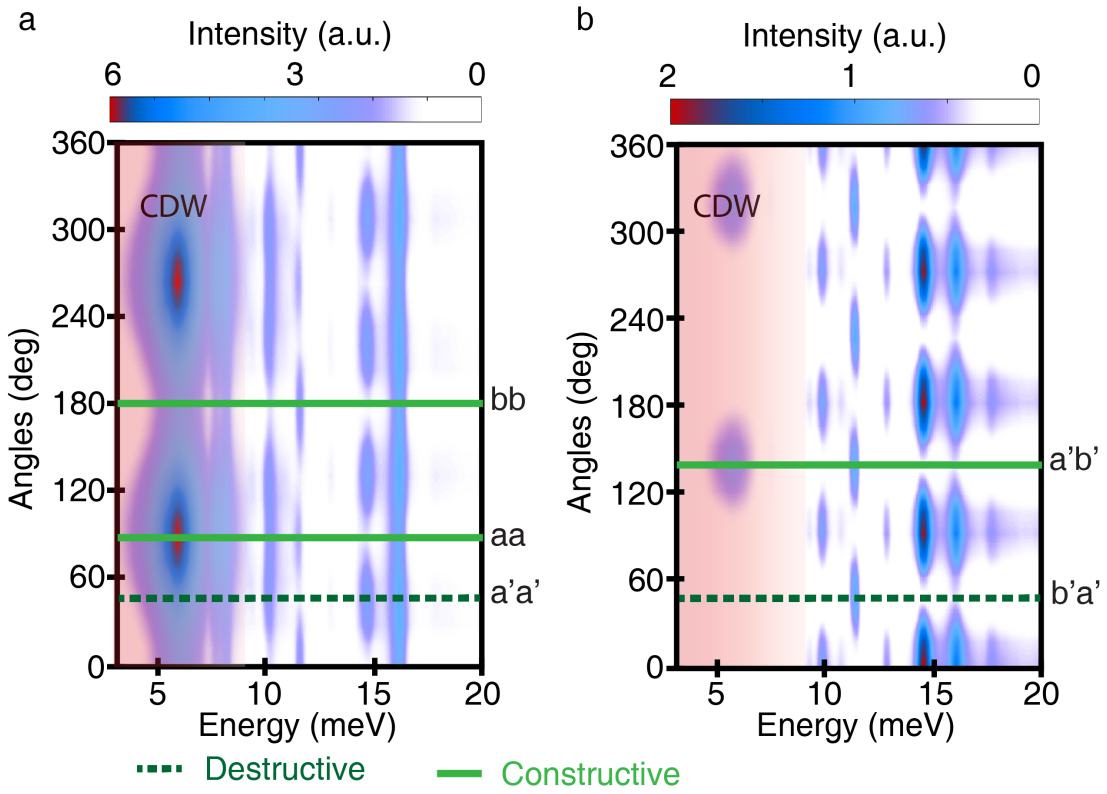

Figure 2.5: Color map of angular resolved Raman at 300K in parallel (a) and cross (b) linear polarization. The green lines indicate the angles of the representative spectra in previous figure

Raman tensor associated to each mode using a generic representation in the orthorombic crystal group where the parameters are optimized to best fit the experimental data. We find that both the A_g and B_g phonons follow the expected angular dependence with four fold modulation when the associated Raman tensor is purely symmetric, reflecting the fact that the structure is nearly tetragonal.

On the other hand, the Higgs mode reveals clear two fold modulated intensities in both parallel and cross polarization (Fig. 2.7) that is well-described by the Raman tensor R_{CDW}, where both pathways are summed. To the best of our knowledge this is the first such observation in any Raman experiment. This result highlights the utility of the full angular dependence of the Raman in revealing and potentially controlling the quantum

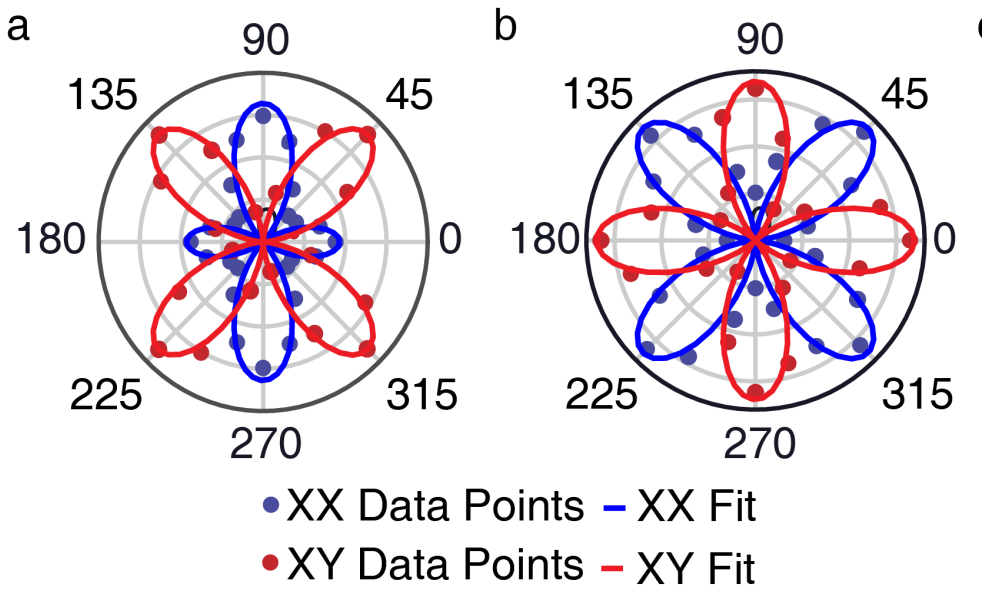

Figure 2.6: (a.b)Angular dependence of the ampltiudes of the Raman modes extracted from Voigt fits of the spectra in parallel (red dots) and cross (blue dots) linear polarization. (c) A_g mode of $GdTe_3$. (d) B_g mode of $GdTe_3$.

pathways in a CDW system. Indeed, by simply rotating the light polarization we vary the different pathways relative phase from 0 to π (i.e. constructive and destructive interference).

2.3.3 Control experiment and temperature dependent data

We now discuss alternative origins of the anomalous Higgs response. One is intrinsic angular momentum from the Gd moments. Another could be the competing phase with a secondary CDW in $GdTe_3$. This is seen by tuning the rare earth, where a bidirectional CDW appears at low temperatures for rare earths smaller than Gd. The role of fluctuations of this bidirectional CDW are unclear. In our TEM measurements some $GdTe_3$ flakes revealed very weak secondary CDW (see supplemental).

Therefore to eliminate the complexities from Gd (magnetism and multidomains), we tested the response of $LaTe_3$, which possesses T_{CDW} >600 K and contains no magnetic moments. Nonetheless, since all the RTe_3 have a similar electronic structure[5],

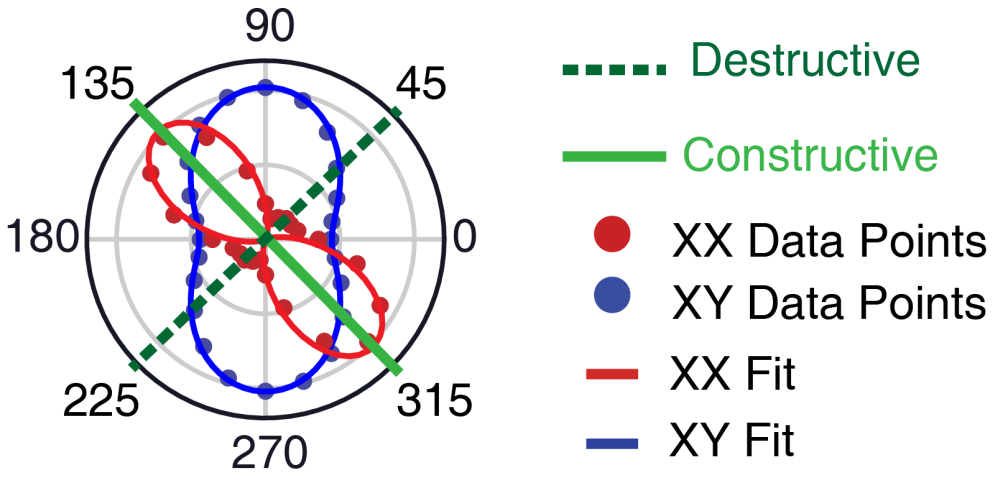

Figure 2.7: Angular dependence of the ampltiudes of the CDW mode of $GdTe_3$ extracted from Voigt fits of the spectra in parallel (red dots) and cross (blue dots) linear polarization. This reveals the constructive (green a'b') versus destructive (dashed green b'a') interference.

the quantum pathway interference should remain. As shown in Fig.2.8a, the angular dependence of the Higgs mode in $LaTe_3$ also reveals a two fold symmetry in both parallel and cross polarization, while the B_g phonon shows the expected four fold response (Fig. 2.8b). The $LaTe_3$ result thus confirms the interference is not due to intrinsic moments or competing phases, but from the band structure and quantum pathway selection. To ensure the reproducibility and intrinsic nature of our results, we also tested another flake, exfoliated from a different $GdTe_3$ crystal from another growth using a separate Raman setup with shorter wavelength excitation laser (488 nm). Since the 488 nm is still in resonance, it reveals the same angular dependence of the modulation of the intensity (Fig. 2.8c).

As a final check of the robustness of the quantum interference, we turned to the temperature dependence. Due to a large change in the Higgs mode energy, its interaction with a nearby phonon varies with temperature[19]. As shown in Fig. 2.9a and consistent with previous measurements, the Higgs mode softens from 10 meV to 3 meV when increasing temperature from 8 K to 300 K, along with a decrease in intensity. This is a

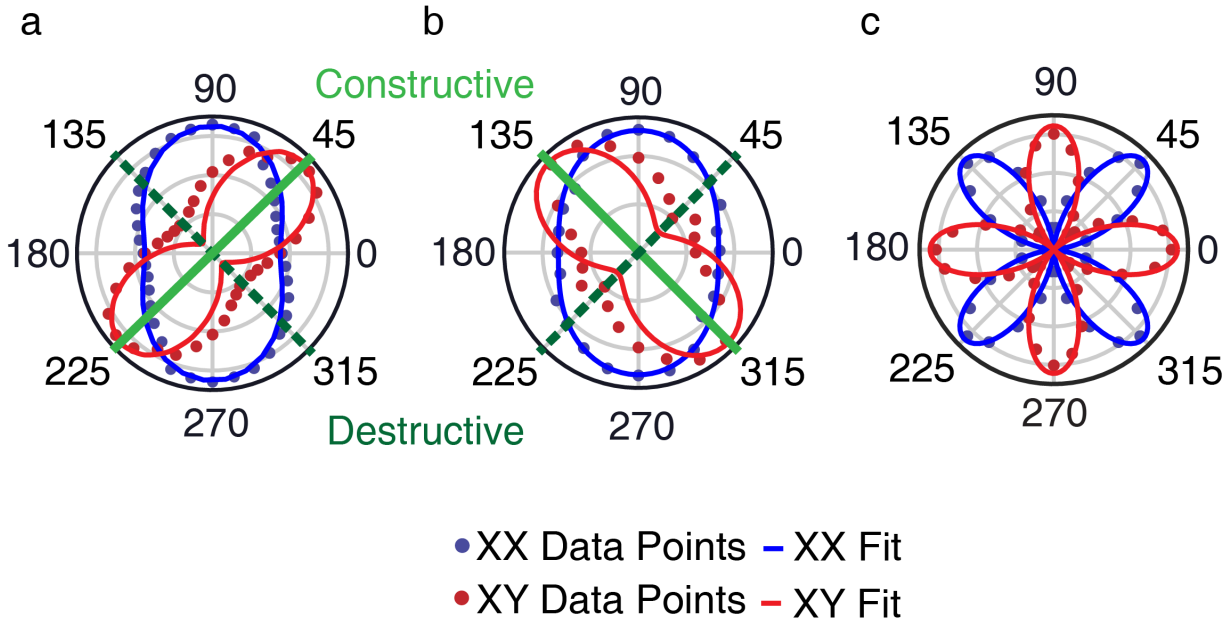

Figure 2.8: (a) Angular dependence of the Higgs mode in $LaTe_3$ measured with a 532 nm excitation laser. (b) B_g mode of $LaTe_3$ with 532 nm laser following the expected angular dependence. (c) $GdTe_3$ Higgs mode measured with a 488 nm excitation laser on a different system.

typical temperature dependence for a Higgs mode, resulting from the potential landscape of the free energy being reduced as the CDW transition temperature is approached. In addition, the Higgs mode displays an avoided crossing with the 7.4 meV phonon consistent with it revealing the the same symmetry as the Higgs. This is due to the fact that this mode is folded to $q = 0$ by the CDW and thus can undergo the same quantum pathway interference[19, 42, 44]. Therefore, we choose three temperatures to test the quantum interference via the cross polarization modulated intensities: 8K, slightly below (140K) and well above the avoided crossing (300K). As seen in the polar plot in Fig. 2.9b, the Higgs mode has the exact same angular dependence at all temperatures. This demonstrates that the quantum interference is robust to the mixing of the Higgs mode with nearby phonons.

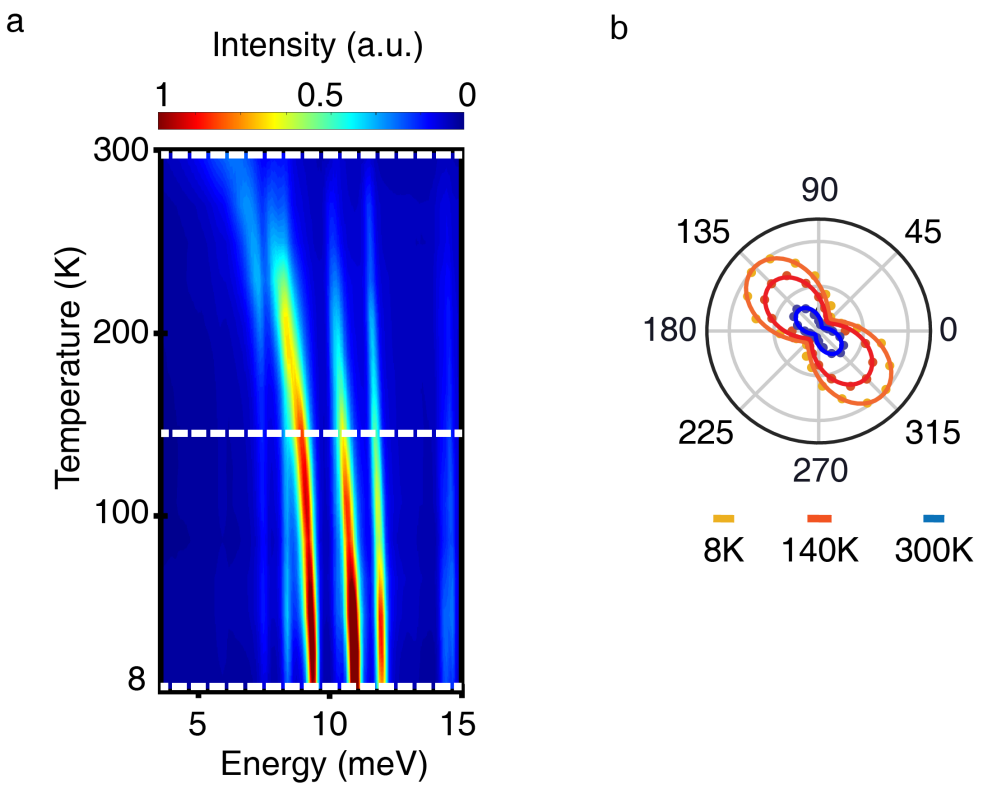

Figure 2.9: (a) The angular dependence of the Higgs intensity (dots) and fitting from Raman tensors(lines) at different temperatures, demonstrating the effect is insensitive to mixing with the neighboring phonon mode. (b) Temperature dependent Raman color map of $GdTe_3$.

2.4 Summary and outlook

Our study provides the first detection of an axial Higgs mode, exploiting the quantum pathway interference in Raman scattering. The finite angular momentum of the Higgs provides compelling evidence that the charge density wave order in RTe_3 is unconventional. Using a phenomenological description of the Fermi surface we elucidate the role of next-nearest neighbour interaction in the observed asymmetry of Raman transitions involving a change of angular momentum. The methodology employed, can be applied to search for new symmetry broken and topologically ordered states via their novel collective modes. Furthermore the straightforward application of tuning the interference

with light polarization could enable manipulating the quantum properties of collective excitations towards new non-equilibrium states.

CHAPTER III

Magnetic fractional excitation in spin liquid systems

3.1 Introduction

Exotic excitations with fractional quantum numbers are a key characteristic of quantum spin liquid systems(QSLs)[45–48]. It results from the long range entanglement of these non-trivial topological phases[49–51]. Originating from frustrated magnetic interactions, the fractional nature inspires an overarching goal of studying QSLs. Great process has been made in the last decade towards identifying the fractional excitations of QSLs[52–60].

Kitaev spin liquid was proposed by Kitaev[56] in 2006, which provides the exactly solvable ground states. Fig. 3.1 shows the cartoon of frustrated spins on kitaev honeycomb lattice. This makes the realizing of topological quantum computing immune to decoherence via high operating temperatures from large exchange interactions with in reach[61, 62]. Attention has focused on relativistic Mott insulators that are close to the exactly solvable Kitaev model with a QSL ground state. In materials such as A_2IrO_3 (A = Cu, Li or Na)[48, 61, 63–67] and α-$RuCl_3$[68–71], the large spin-orbit coupling and Coulomb repulsion result in $j_{eff} = 1/2$ moments on a honeycomb lattice[46, 62, 72–79]. According to the pure Kiteav model, in these materials spin flips could produce Z_2 gauge fluxes and dispersive Majorana fermions.[56, 80]. A scrach of the top view of $RuCl_3$ is provided in Fig. 3.2.

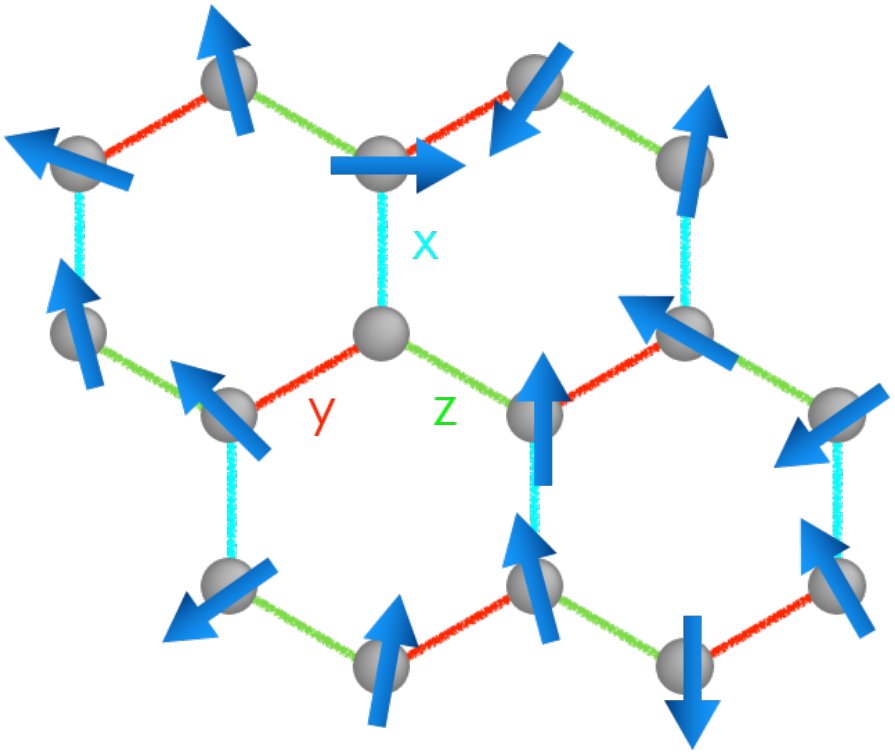

Figure 3.1: Cartoon of frustrated spins on honeycomb lattice

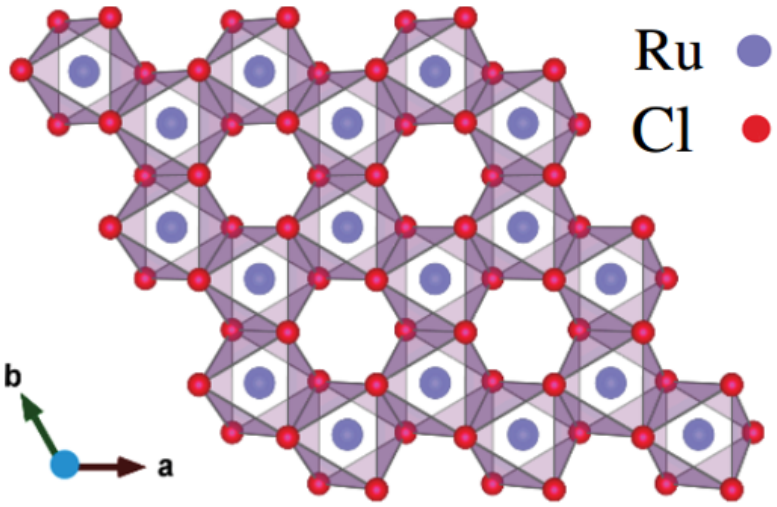

Figure 3.2: Lattice structure of $RuCl_3$

In these materials, as with other QSL candidates, the presence of additional symmetry allowed terms (Heisenberg and bond-dependent off-diagonal interactions in this case), produces long range magnetic order.[52, 73, 81] Despite extensive studies and evidence for fractional particles,[53, 78, 82, 83] the relative size of the non-Kitaev terms and the range over which they are relevant remains controversial[81, 84]. In α-$RuCl_3$, these non-Kitaev terms lead to a magnetically ordered phase below 7 K, which could be destroyed by an in-plane magnetic field[85–89]. The exact nature of the field induced QSL state remains unclear[71, 82, 86] as the zero field Hamiltonian is still unresolved. In particular, non-Kitaev interactions dominant energy and temperature ranges have not yet been experimentally established. Additionally, there is a need to determine if excitations in these ranges maintain their fractional nature.

Raman scattering is a powerful probe detecting magnetic materials, which can reveal the presence of long range order, symmetry and statistics of the excitations, as well as the strength and nature of the exchange, even in single 2D atomic layers[47, 90–97]. Indeed, Raman scattering was the first to reveal the continuum from magnetic excitations in α-$RuCl_3$[53]. The Raman scattering process of fractional particles are presented in Fig. 3.3. However, a careful study of the Kitaev term's temperature and energy dependence is still a challenge, as one requires a very high temperature and energy resolution to show the spectral change and directly compare the spectra with theoretical calculations[98]. Previously, Raman efforts relied on spectral integration over a certain energy range which averaged out the energy dependence of the excitations, and the low scattering intensity made it difficult to directly compare the spectra with theoretical calculations from the exact Kitaev model. As such the role of the non-Kitaev terms, and their size, could not be identified in previous efforts. Furthermore, demonstration of the fractional nature relied on the integrated Raman intensity and thus required subtraction of a bosonic background, without justification. This approach also meant fitting the data with an average energy in the fermi function, further limiting the ability to uncover if

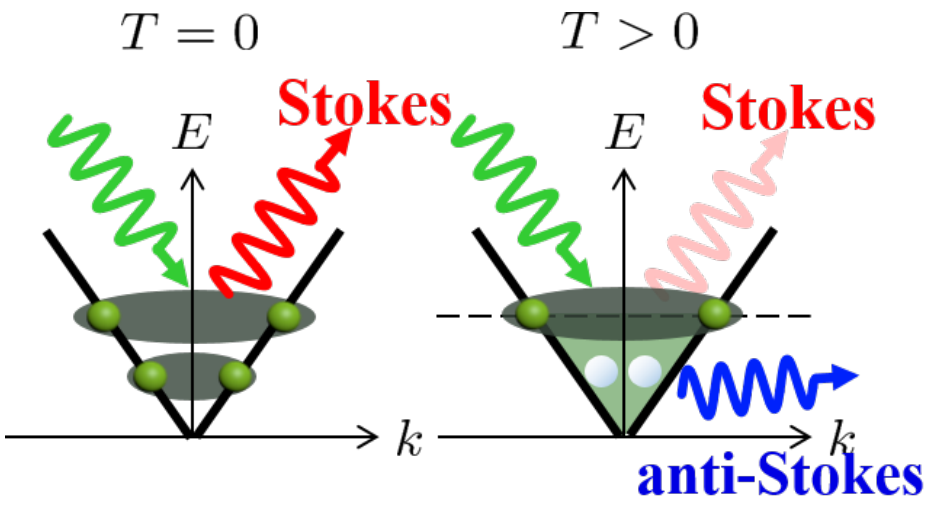

Figure 3.3: Stokes and anti-Stokes Raman scattering process of QSLs at $T = 0K$ and $T > 0K$

the non-Kitaev terms affected the statistical response of the excitations.[70, 78].

Here, we overcome all these previous limitations with new Raman spectra with dramatically improved signal levels, high temperature and energy resolution. Firstly, having improved the optics, our Raman measurements now obtain a signal level 18 times larger than before[53]. This high signal level provides enough anti-Stokes response to ensure the temperature is correct and allows us to directly extract the Raman susceptibility by taking the difference between Stokes and anti-Stokes intensities, after the dark counts have already been removed. In this way, the role of the non-Kitaev terms is revealed via a direct comparison of the full temperature and energy dependence of the α-$RuCl_3$ Raman susceptibility with a QMC calculation for the pure Kitaev model. Furthermore, we provide compelling evidence for the fermionic nature of the excitations without the need to subtract a bosonic background. Our results show that the Raman susceptibility of α-$RuCl_3$ is consistent with QMC calculations at higher temperatures and energies ($>$40K & $>$6meV). The deviation between them in the low temperature and energy range ($<$40K & $<$6meV) results from the non-Kitaev terms. Via these temperature and energy boundaries, we directly measure the ratio of J_K and Γ interactions in the Hamiltonian.

Moreover, the high temperature($> 150K$) difference between the Raman susceptibility and the QMC indicates the presence of quasi-elastic scattering (QES) induced by thermal fluctuations in the system, commonly observed in frustrated systems[51, 53, 70]. With our enhanced signal the anti-Stokes spectra for all temperatures can be compared with the Stokes response to prove the sample is in detailed balance without laser heating (see Fig. 3.8). To further explore the effect of non-Kitaev interactions, we fit the Raman susceptibility with a Fermi function containing half the measured energy. The very good overlap shows the excitations are governed by Fermi statistics even beyond the Kitaev dominant range.[99] We also checked that the susceptibility integration is governed by a Fermi function with half energy, which further confirms each fractional particle holds one half of the scattering energy in both Kitaev and non-Kitaev dominant regimes. Interestingly this is revealed without the need to subtract the bosonic background.

3.2 Experiment methods

3.2.1 crystal growth and characterization.

Single crystals of α-$RuCl_3$ were prepared using high-temperature vapor-transport techniques from pure α-$RuCl_3$ powder with no additional transport agent. Crystals grown by an identical method have been extensively characterized via neutron scattering techniques[83, 86, 100] revealing behavior consistent with what is expected for a relativistic Mott insulator with a large Kitaev interaction[58, 68, 69, 73, 74, 76, 77, 85, 87, 89, 101–103]. The crystals have been shown to consistently exhibit a single dominant magnetic phase at low temperature with a transition temperature $T_N \approx 7$ K, indicating high crystal quality with minimal stacking faults[100]. Care was taken in mounting the crystals to minimize the introduction of additional stacking faults, as evidenced by the high reproducibility of the spectra across different crystals and experimental setups. Characterization was consistent with previous studies[68, 71, 88, 104–106].

3.2.2 Raman spectroscopy experiments.

Since Raman scattering involves a photon in and photon out, it allows one to measure both the symmetry and energy change of an excitation. Furthermore, one can choose an energy and/or symmetry channel to separate the magnetic, electronic and lattice responses[53, 55, 70, 78, 96, 107, 108]. The majority of the Raman experiments were performed with a custom built, low temperature microscopy setup[29]. A 532 nm excitation laser, whose spot has a diameter of 2 μm, was used with the power limited to 30 μW to minimize sample heating while allowing for a strong enough signal. The sample was mounted by thermal epoxy onto a copper xyz stage. At both room and base temperature the reported spectra were averaged from three spectra in the same environment to ensure reproducibility. The spectrometer had a 2400 g/mm grating, with an Andor CCD, providing a resolution of ≈ 1 cm^{-1}. Dark counts are removed by subtracting data collected with the same integration time, but with the laser off. To minimize the effects of hysteresis from the crystal structural transition, data was taken by first cooling the crystal to base temperature, and once cooled to base temperature, spectra were acquired either every 5 or 10 K by directly heating to that temperature. The absence of hysteresis effects was confirmed by taking numerous spectra at the same temperature after different thermal cycles (100 K in the middle of the hysteresis region). In addition, recent studies of the Raman spectra of $RuCl_3$ suggest an effect of the surface structure upon exposure to air[93, 104]. To minimize this, crystals were freshly cleaved and immediately placed in vacuum within three minutes. Lastly, a recently developed wavelet based approach was employed to remove cosmic rays[29, 109].

3.3 Fractional excitation and analysis

In inelastic light scattering, the measured intensity is determined by symmetry, Fermi's golden rule, and from the fluctuation-dissipation theorem, is proportional to

the Raman susceptibility (Im($\chi[\omega, T]$)) times a Bose function[107, 110]. In magnets this can produce peaks from single magnons, broad features reflecting the two-magnon joint density of states (JDos), or QES from thermal fluctuations[53, 55]. For the Kitaev QSL, Raman predominantly excites pairs of fractional particles in the energy range considered here ($\approx 0.5J_K < \hbar\omega <\approx 2J_K$), leading to the energy loss ($I_S[\omega, T]$) and gain ($I_{aS}[\omega, T]$) intensities[78, 111]:

$$I_S[\omega, T] = \text{Im}(\chi[\omega, T])(n_B[\omega, T] + 1) = JDos[\omega, T](1 - n_F[\omega/2, T])^2 \tag{3.1}$$

$$I_{aS}[\omega, T] = \text{Im}(\chi[\omega, T])(n_B[\omega, T]) = JDos[\omega, T](n_F[\omega/2, T])^2 \tag{3.2}$$

where $n_{B/F}[\omega, T]$ are the Bose/Fermi distributions and $JDos[\omega, T]$ is approximately given by the JDos from the fractional particles. For responses from non-fractional excitations, for example phonons, we expect an additional term to be added to the susceptibility, without contributions from the Fermi function.

As shown in Fig. 3.4, we collected both the Stokes and anti-Stokes spectra of bulk α-$RuCl_3$ from 10 K to 300 K. Our Rayleigh scattering half width is 2.3 meV, enabling measurement down into the low energy regime. The temperature dependent spectra show a clear magnetic excitation continuum (2.3meV $\sim$ 10 meV) below the first phonon, which mostly results from the Kitaev interaction and is consistent with previous predictions and measurements[53, 70, 78, 83]. Since the measured Raman intensity contains a Bose factor, it is best to investigate the Raman susceptibility Im$[\chi[\omega, T]]$[55, 94, 96, 107]. Using our new anti-Stokes spectra, we directly determine the susceptibility from the difference between the Stokes and anti-Stokes intensities ($I_S[\omega, T] - I_{aS}[\omega, T] =$ Im$[\chi[\omega, T]]$). This new data set, combined with minimizing the rise in temperature due to the laser, reveals the regimes in which non-Kitaev terms are relevant. Specifically, Fig. 3.5 shows the comparison of the QMC results for the pure Kitaev limit and the

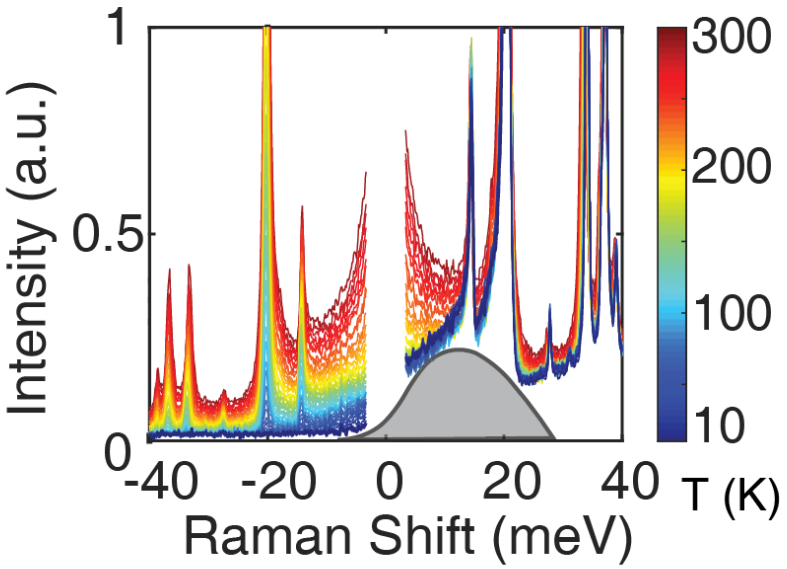

Figure 3.4: Temperature dependent Raman intensity of α-$RuCl_3$ in XY polarization. Both Stokes and anti-Stokes data are collected from 10 K to 300 K with 5 K steps below 120 K and 10 K steps above. the gray shade is indicates the magnetic continuum excitation

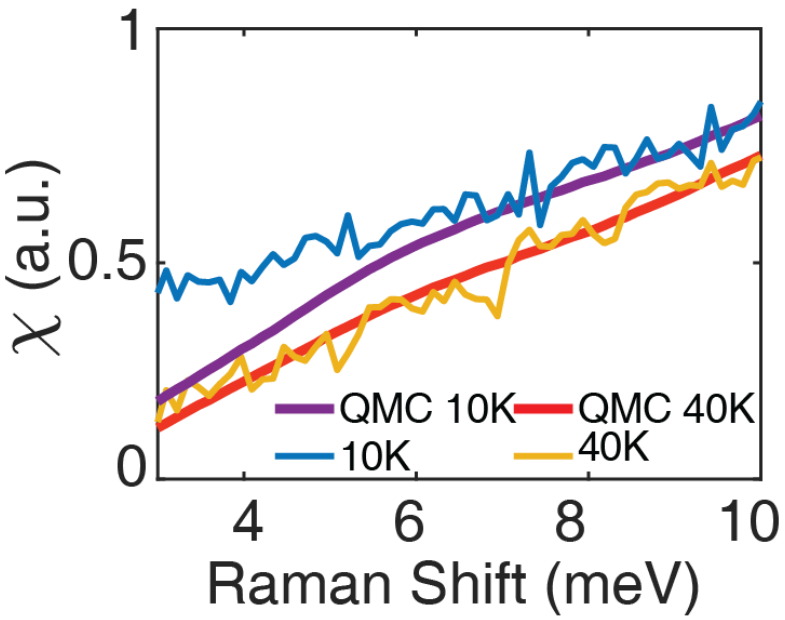

Figure 3.5: The measuredRaman susceptibility in XY polarization of α-$RuCl_3$ at 10 K (blue line) compared with the calculated result of the pure Kitaev limit (purple line) at the same temperature. The enhanced signal at low energies results from the non-Kitaev interactions in the system. By 40 K there is nearly perfect agreement between the Raman data (yellow line) and the QMC calculation (red line), indicating the non-Kitaev terms are not relevant in this energy and temperature range.

Raman susceptibility at 10 and 40 K. While excellent agreement is seen at 40 K, the data at 10 K only matches the model between 6 to 10 meV. Noting that this temperature is still above the magnetic ordering temperature of 7 K, this additional susceptibility results from non-Kitaev terms, as recently suggested by exact diagonalization (ED) calculations[84].

To further investigate the temperature and energy dependence of the non-Kitaev interactions, we consider the energy and temperature dependent colormap in Fig. 3.6. Here $\chi_\delta = \chi_{measured} - \chi_{QMC}$ is the difference between the measured Raman susceptibility and that of the pure Kitaev model (determined by the QMC calculation). The green color indicates the measured susceptibility is higher than the QMC results and

the blue color indicates regions of very good overlap between the measurement and the calculation. The black dots suggest the temperature and energy boundaries where the system perfectly resembles the pure Kitaev QSL. Specifically, there is a large χ_δ in the quarter circle area below 6 meV and 40 K, which can be explained as the region where non-Kitaev interactions become dominant in the response. The deviation above 150 K and below 8 meV results from the QES induced by thermal fluctuations in the system, which is well known in frustrated magnets[51, 53, 70, 92, 108]. The high energy deviation (>12meV) is from the low energy tail of the phonon. Nonetheless, the low energy and temperature deviation from the pure Kitaev model is consistent with the calculated intensities of recent ED results for a model with only Γ and Kitaev terms in the system (K-Γ model)[84] with $-J_K/\Gamma = 5$. Furthermore, the ED results suggest enhanced response over that expected for the pure Kitaev limit for $\omega_\Gamma \sim 2.5\Gamma$. As shown in our colormap, when the temperature is low, the disagreement occurs for $\omega_\Gamma < 6$ meV. based on the K-Γ model, this suggests $\Gamma \approx 2.4$ meV, where the Heisenberg interaction and terms beyond nearest neighbors are neglected. We note that regardless of the specific non-Kitaev terms, this can be interpreted as an upper bound on the ratio of Kitaev to non-Kitaev terms in this system. Furthermore, we find the best agreement for the pure Kitaev limit with $J_K = 10$ meV , consistent with our observed bandwidth of the continuum (Fig. 3.4) of 30 meV.[53, 111] The $\Gamma \approx 2.4$ meV we obtained here is also consistent with the results obtained from neutron scattering (2.5 meV)[73], from thermal Hall measurements (2.5 meV)[112], and from THz measurements (2.4 meV)[113].

Having established the size and extent of the non-Kitaev terms, we examine the statistics of the excitations in α-$RuCl_3$ to see if they are truly fractional. As the statistics depends on both temperature and energy, one should make sure the system is in detailed balance[107] and that laser heating is negligible, which was not quantitatively shown before. As discussed in the supplemental, the fermionic response written above is consistent with the fluctuation-dissipation theorem with the presence of time-reversal

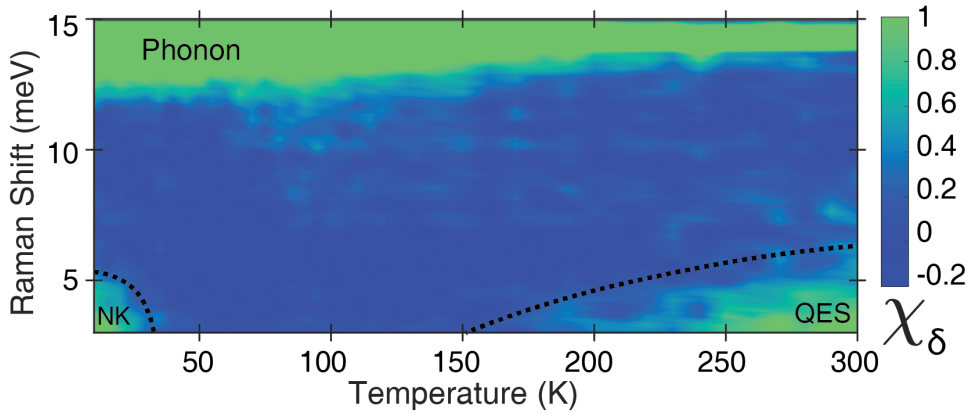

Figure 3.6: The temperature and energy dependent map of $\chi_\delta(\chi_\delta = \chi_{measured} - \chi_{QMC})$. χ_δ at low temperature and low energy range shows the temperature and energy boundary of non-Kitaev (NK) interactions in the system. χ_δ at the high temperature and low energy range indicates the quasi-elastic scattering (QES) in the system.

symmetry, requiring $I_S[\omega, T]/I_{aS}[\omega, T] = e^{\frac{\hbar\omega}{k_B T}}$[94, 107]. Previously, the discrepancy between the prediction of the Bose factor and the measured intensity at low temperatures was attributed to fractional statistics[70, 78]. However, these works did not exclude the possibility that laser induced heating kept the measured area at a fixed temperature, while the bulk was cooled. This is not unlikely, given the small specific heat and thermal conductivity of $RuCl_3$ at low temperatures[99–101, 114, 115]. Furthermore, as described in the supplemental, previous uses of the anti-Stokes responses were unreliable due to the low signal levels[53]. Most importantly, unless the temperature is well known, it is difficult to directly compare with the theoretical prediction for fractional statistics. In our current work we have made substantial improvements to the thermal anchoring and collection efficiency to allow for much higher temperature resolution and lower Raman frequency. In this way, we can observe the spectra change between different temperatures and directly compare it with the QMC results. Most importantly, due to enhanced signals and lower probing frequencies, we have been able to collect anti-Stokes response at lower temperatures to ensure that laser induced heating is not an issue. Returning

to the actual sample temperature, in Fig. 3.9, we compare the anti-Stokes intensity and Stokes intensity times a Boltzmann factor with the measured temperature. The excellent agreement between them reveals that there is nearly no heating in the laser spot and thus we can use the measured crystal temperature. Unlike previous studies[53, 70], our new quantitative comparison between Stokes and anti-Stokes limits the possibility of laser heating to explain the low temperature upturn and confirms the sample is in detailed balance.

We explore the possibility that the Raman susceptibility results from purely fermionic excitions in Fig. 3.7a. If the excitation is fractional, one expects $\mathrm{Im}[\chi(\omega,T)] \propto JDos(\omega,T) * (1-2n_F(\omega/2,T))$. This results from the particle-hole symmetry of these excitations, and that we are probing creation/annihilation processes. To cancel the constant term and focus only on the fermionic part, we show the difference of susceptibility: $\Delta Im(\chi[\omega, T \leq 150\ \mathrm{K}]) = \mathrm{Im}(\chi[\omega,T]) - \mathrm{Im}(\chi[\omega, 150\ \mathrm{K}])$. The utility of such an analysis is quite clear: the energy and temperature extent of the continuum can be directly observed - without contributions from high temperature QES fluctuations or phonons. To test the predicted fermionic response from fractional particles, we plot $\Delta n_F[\omega/2,T] = n_F[\omega/2,T] - n_F[\omega/2, 150\ \mathrm{K}]$, as contour lines on top of the data. The agreement is quite good and is further confirmed via constant temperature cuts of the data shown in Fig. 3.9, along with the calculated $\Delta n_F[\omega/2,T]$. The good agreement between the data and Fermi functions with half of the scattering energy provides strong evidence for the presence of pairs of fractional particles. We note this is done without any artificial subtraction of a bosonic background.

The approach described above, relies on a nearly temperature and energy independent $JDos[\omega,T]$, which is expected from the numerical calculations for the Kitaev system at temperatures above the flux gap[99]. This assumption appears to generally hold in our data, whose temperature and energy evolution are generally described by a Fermi function. Nonetheless, at the lowest temperatures, there is some deviation of the data for

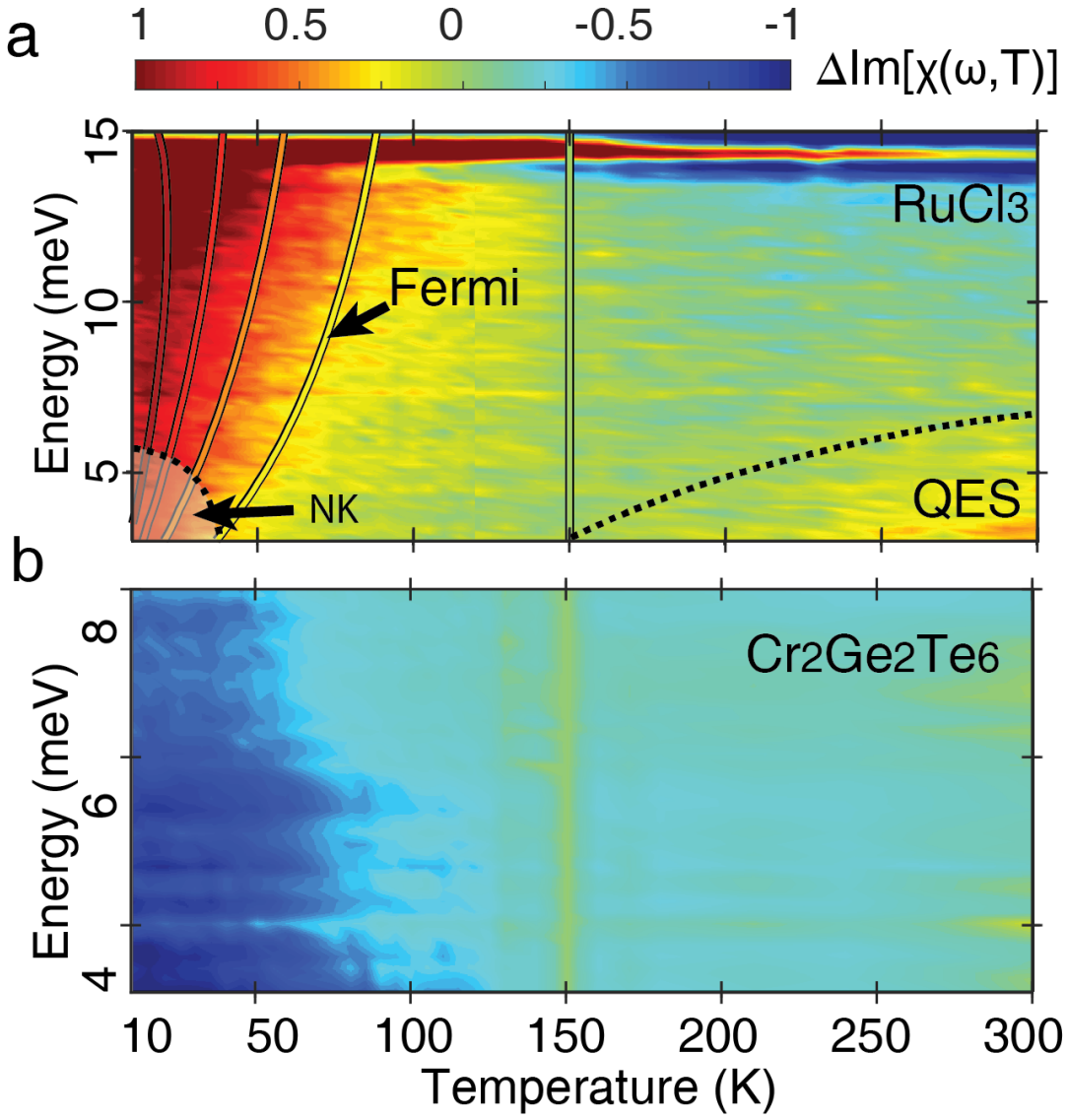

Figure 3.7: (**a**)Raman susceptibility of $RuCl_3$, $\Delta\text{Im}[\chi(\omega,T)] = \text{Im}[\chi(\omega,T)] - \text{Im}[\chi(\omega,150\text{ K})]$). The curves with black outlines are the contour plots of the Fermi function ($\Delta n_F(\omega/2,T) = n_F(\omega/2,150) - n_F(\omega/2,T)$). Both data and the prediction are normalized to their maximum values. The agreement between the two confirms that Raman creates magnetic excitations that are made of pairs of fermions. The upturn of the Raman intensity in the high temperature and low energy range results from thermal fluctuations of the magnetism (quasi-elastic scattering). (**b**) Raman susceptibility of a similar magnet, $Cr_2Ge_2Te_6$, where, opposite to α-$RuCl_3$, $\Delta Im[\chi(\omega,T)]$ is negative and does not match $n_F(\omega/2,T)$.

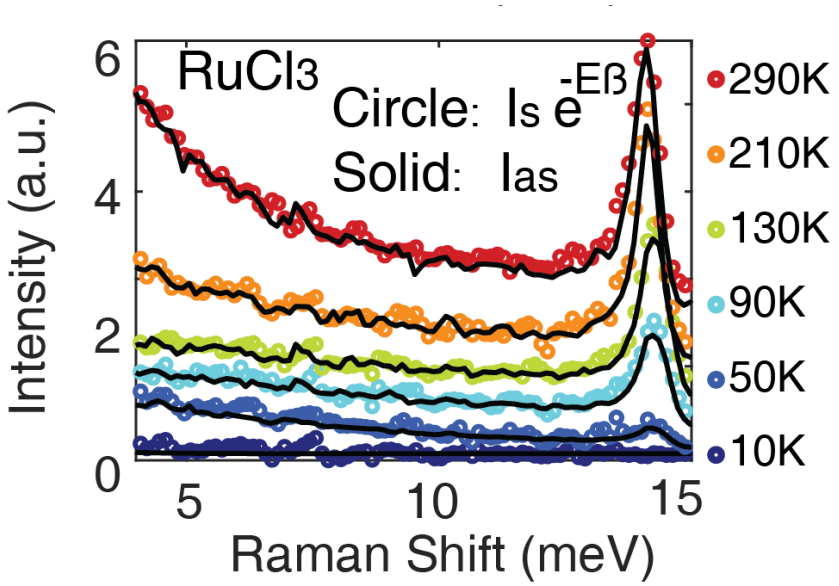

Figure 3.8: The excellent agreement between Stokes and anti-Stokes spectra of α-$RuCl_3$ when normalized by the Boltzmann factor demonstrates the absence of laser heating.

energies above 6 meV. The origin of this discrepancy is not clear, but likely results from the temperature and energy dependence of the $JDos[\omega, T]$. Additionally, we find poor agreement if the full scattering energy ($n_F[\omega, T]$) is used (not shown). We additionally performed the same analysis on another honeycomb system $Cr_2Ge_2Te_6$ (Fig. 3.7), which was grown by established methods and which is ferromagnetic below 60 K with a similar Curie-Weiss temperature as α-$RuCl_3$[108, 116]. The behavior of $Cr_2Ge_2Te_6$ is the exact opposite of α-$RuCl_3$, namely, $\Delta\text{Im}(\chi[\omega, T])$ is negative throughout the whole measured range and decreases upon cooling.

Returning to Fig. 3.7a, we have also drawn the boundary of the non-Kitaev contributions determined from the analysis in Fig. 3.6. We find the Fermi function matches the susceptibility very well, suggesting the Fermi statistics hold even when the agreement with the pure Kitaev model (see Fig. 3.7) does not. However, given the relatively large size of the Kitaev term relative to the non-Kitaev contributions, this may not be surprising and suggests the excitations in α-$RuCl_3$ are primarily fractionalized. Our analysis presented in Fig. 3.6 and Fig. 3.7 also reveals the crossover from spin

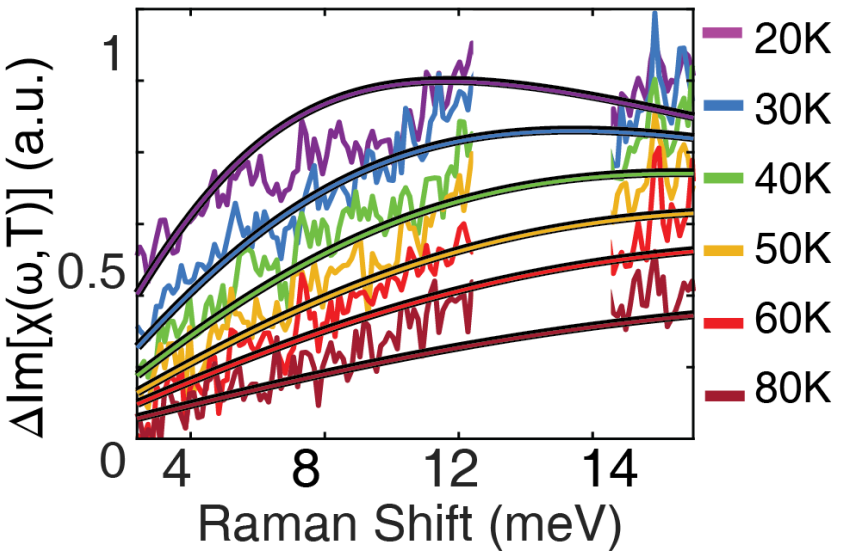

Figure 3.9: Comparison of $n_F(\omega/2, T)$ and $\Delta\text{Im}[\chi(\omega, T)]$ of $RuCl_3$ at fixed temperatures. The agreement further confirms the excitations are fermionic.

liquid-like behavior (i.e. fractional continuum) to a standard paramagnet. Indeed, $\Delta\text{Im}(\chi[\omega, 150\text{ K} \leq T \leq 200\text{ K}])$ is nearly constant, as expected for a paramagnet in this range. As discussed later, the response at higher temperatures is consistent with quasi-elastic scattering. We note that the exact temperature at which the response will set in, depends on the energy scale at which it is measured. As such the integrated response investigated in Fig. 3.10,3.11 appears to have a higher onset temperature for the QES due to the inclusion of higher energy scales. Specifically, a Lorentzian at zero energy results from thermal fluctuations of the magnetism that confirm the magnetic specific heat is consistent with a standard paramagnet at high temperatures. Lastly, this analysis also provides new insights into the phonons overlapping the continuum. Specifically, consistent with previous works we also find the phonons have a low energy tail due to their coupling with the continuum (see Fig. 3.4). However, via our new comparison with the pure Kitaev limit, it is clear the influence of the two lowest energy phonons on the continuum is limited to $\approx 12 \rightarrow 14meV$, and $\approx 15 \rightarrow 19meV$, respectively.

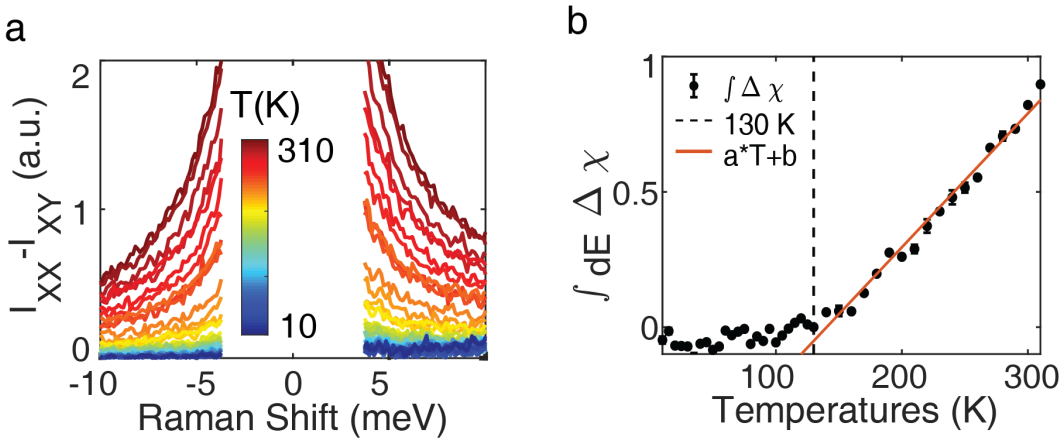

Figure 3.10: The continuum in α-$RuCl_3$ due to fractional particles is removed by taking the difference between XY and XX intensities. This confirms the continuum is consistent with predictions of the Kitaev model, and the high temperature response is from quasi-elastic scattering (i.e. Lorentzian times a Bose factor). (**b**) The integration of the Raman susceptibility(3meV - 8meV) with only the quasi-elastic scattering response, reveals a linear T behavior above 150 K and temperature independent behavior below.

Interestingly, the response in these regions still follows the prediction of the Fermi function (3.7), showing the mixing of the phonons with the fractional excitations does not significantly influence them.

To ensure our approach is self-consistent it is worthwhile to also analyze the integrated Raman response, as done previously in α-$RuCl_3$ and Li_2IrO_3.[53, 70, 78] Likewise, it is also crucial to find a reliable method to separate the QES response from the continuum such that it can be independently studied for further confirmation of the presence of Fermi statistics. This is now possible using both the polarization and Stokes minus anti-Stokes spectra (Im$[\chi[\omega, T]]$). Since the continuum has equal weight in both polarizations[53, 111] it can be removed via their difference: $\Delta I_{S/aS}[\omega, T] = I^{XX}_{S/aS}[\omega, T] - I^{XY}_{S/aS}[\omega, T]$. We also note the isotropic response of the continuum implies an isotropic Kitaev interaction.[78, 111] As seen in Fig. 3.10a, $\Delta I_{S/aS}[\omega, T]$ is consistent with thermal fluctuations (i.e. QES)[55, 92, 96], namely a Lorentzian whose amplitude is given by the magnetic specific heat ($C_m[T]$) times the

temperature and appropriately weighted Bose factors (i.e. greater Stokes than anti-Stokes intensity). We now calculate the QES amplitude via the spectral weight (SW) of the Raman susceptibility: $SW_{QES}[T] = \int \chi_{XX}^{QES}[\omega, T] - \chi_{XY}^{QES}[\omega, T] d\omega = \int dE \Delta\chi$. Here, the integration energy range is 3 to 8 meV. Consistent with direct fits of the $\Delta I_{S/aS}[\omega, T]$ (see supplemental) and robust to the limits of integration (as long as phonons are not included), we find $SW_{QES}[T] \propto T$ (see Fig. 3.10). This suggests the magnetic specific heat is nearly temperature independent, as expected for a classical paramagnet at high temperatures. Since the QES signal is nearly zero in $\chi[\omega, T < 150$ K], this confirms the Raman susceptibility (and not the intensity) naturally separates the QES from the continuum. Thus our new measurements reveal the energy and temperature range over which the excitations are fractional without contamination from other contributions.

Having isolated the QES and identified its temperature dependence, we can independently check the temperature bounds of the Fermi statistics. Specifically, we investigate the difference between the Stokes and anti-Stokes SW in a given polarization ($\Delta SW[T] = \int (I_S[\omega, T] - I_{aS}[\omega, T]) d\omega$), which includes the integrated Fermi function from the fractional excitations and the QES contribution (see supplemental). As shown in Fig. 3.11a & b for two different polarizations, the integrated weight follows the expected response for pairs of fermionic excitations ($\int (1 - 2n_f(\omega/2, T)) d\omega$) until $T \approx 150$ K where it crosses over to a linear temperature dependence from the QES. The fermionic response is equal in both polarization configurations and covers the Kitaev ranges. Thus with just three parameters, one fixed by the lowest temperature, we fully explain the SW for all energy ranges, temperatures, and polarizations. To further confirm this, we tried the same analysis on our new $Cr_2Ge_2Te_6$ data. As shown in Fig. 3.11c& d, the difference between the Stokes and anti-Stokes of $Cr_2Ge_2Te_6$ cannot be fit with a Fermi function at all. Thus the results presented in Fig. 3.11a,b provide a quantitative confirmation of the presence of fractional excitations up to high temperatures.

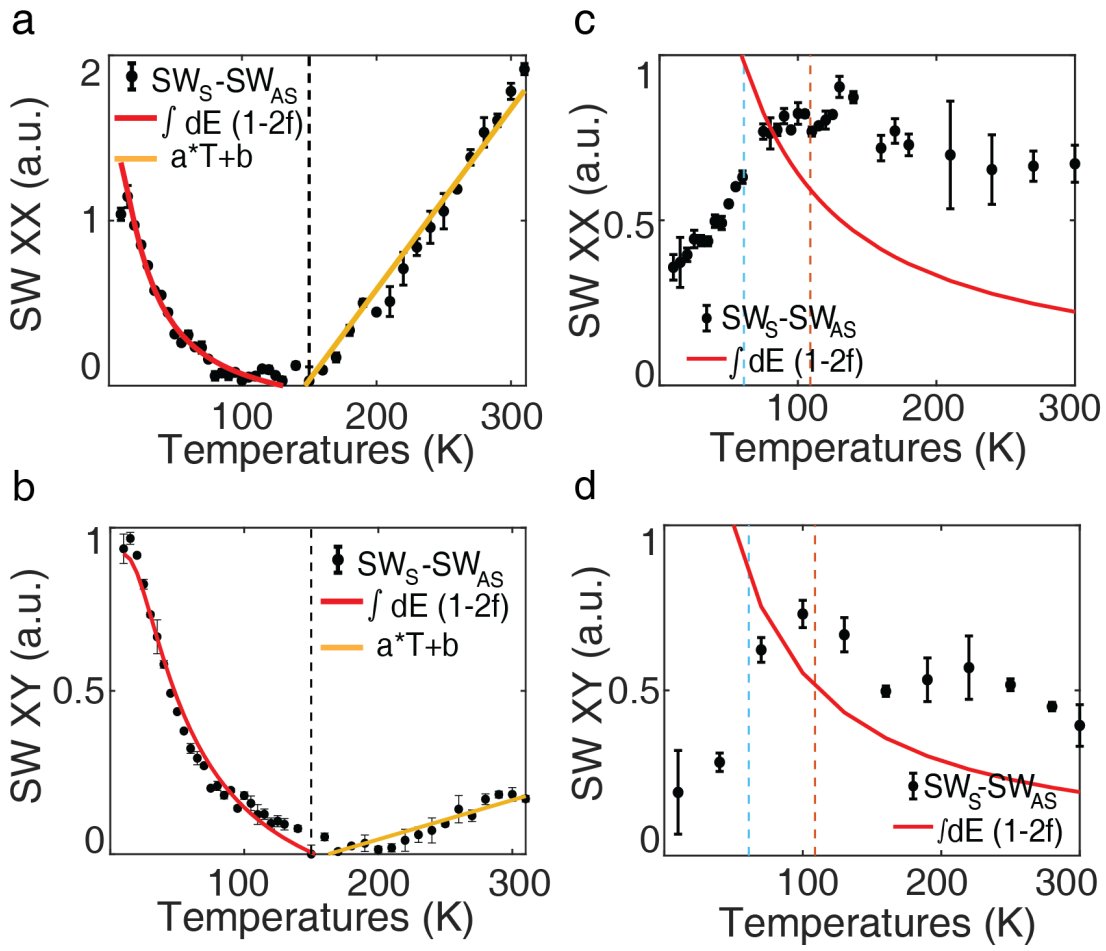

Figure 3.11: **Limit of Fermi statistics** (**a** & **b**) Integrated spectral weight(3meV - 8meV) of Im$[\chi(\omega, T)]$, reveals Fermi statistics in α-$RuCl_3$ below $\approx$100 K (solid red line) in XX and XY polarizations. Above 150 K the response is linear in temperature due to the quasi-elastic scattering (yellow lines). The spectral weight(3meV - 8meV) from $Cr_2Ge_2Te_6$ (**c** & **d**) is enhanced up to T_C (blue dashed line) but the temperature dependence above does not fit that expected for fermions (solid red line).

3.4 Summary and outlook

To conclude, our higher quality data and anti-Stokes spectra provide direct comparison of the Raman susceptibility energy and temperature dependence with QMC calculations. At higher temperatures and energies, these results are consistent with QMC calculations for the pure Kitaev limit. Consistent with ED calculations, the Raman susceptibility is enhanced over the Kitaev QSL only at low energies and temperatures due to additional non-Kitaev terms. Thus our results reveal the temperature and energy boundary of non-Kitaev interactions becoming dominant. Furthermore, via comparison of the measured Raman susceptibility and the Fermi function, the data provide concrete evidence that the magnetic excitations in α-$RuCl_3$ are fractional and follow Fermi statistics. Interestingly, these fractional excitations follow Fermi statistics even in the ranges where non-Kitaev terms become dominant. It remains to be answered whether, and how, different non-Kitaev terms compete with each other in the low temperature and energy range. Nonetheless, our approach enables a new means to extract the size and influence of non-frustrating terms in QSLs, and could be applied at finite magnetic field to confirm the fractional nature of excitations in the field induced QSL state of α-$RuCl_3$.

3.5 Appendix A: Quantum Monte Carlo Calculations.

The Hamiltonian of the Kitaev model on the honeycomb lattice is given by

$$\mathcal{H} = -J_x \sum_{\langle jk \rangle_x} S_j^x S_k^x - J_y \sum_{\langle jk \rangle_y} S_j^y S_k^y - J_z \sum_{\langle jk \rangle_z} S_j^z S_k^z$$

where $\boldsymbol{S}_j$ represents an $S = 1/2$ spin on site j, and $\langle J_K \rangle_\gamma$ stands for a nearest-neighbor (NN) $\gamma (= x, y, z)$ bond shown in Fig. 1a. In the calculation for the spectrum of the Raman scattering we adopt the Loudon-Fleury (LF) approach. The LF operator for the

Kitaev model is given by

$$\mathcal{R} = \sum_{\langle ij \rangle_\alpha} (\boldsymbol{\epsilon}_{\rm in} \cdot \boldsymbol{d}^\alpha)(\boldsymbol{\epsilon}_{\rm out} \cdot \boldsymbol{d}^\alpha) J_\alpha S_i^\alpha S_j^\alpha,$$

where $\epsilon_{\rm in}$ and $\epsilon_{\rm out}$ are the polarization vectors of the incoming and outgoing photons and $\boldsymbol{d}^\alpha$ is the vector connecting a NN α bond[91, 111]. Using this LF operator, the Raman spectrum is calculated as

$$I(\omega) = \frac{1}{N} \int_{-\infty}^{\infty} dt e^{i\omega t} \langle \mathcal{R}(t) \mathcal{R} \rangle, \tag{3.3}$$

where $\mathcal{R}(t) = e^{i\mathcal{H}t} \mathcal{R} e^{-i\mathcal{H}t}$ is the Heisenberg representation. The temperature dependence of $I(\omega)$ is numerically evaluated using the Monte Carlo simulation in the Majorana fermion representation without any approximation[58]. In the following we show the details of the calculation procedure[78].

Using the Jordan-Wigner transformation, the Hamiltonian is mapped onto the Majorana fermion model as

$$\mathcal{H} = \frac{iJ_x}{4} \sum_{(jj')_x} c_j c_k - \frac{iJ_y}{4} \sum_{(jj')_y} c_j c_k - \frac{iJ_z}{4} \sum_{(jj')_z} \eta_r c_j c_k, \tag{3.4}$$

where $(jj')_\gamma$ is the NN pair satisfying $j < j'$ on the γ bond, and η_r is a Z_2 conserved quantity defined on the z bond (r is the label for the bond), which takes ± 1. This Hamiltonian is simply written as

$$\mathcal{H} = \frac{1}{2} \sum_{jk} A_{jk}(\{\eta_r\}) c_j c_k, \tag{3.5}$$

using the Hermitian matrix $A_{jk}(\{\eta_r\})$ depending on the configuration of $\{\eta_r\}$. The LF

operator shown in Eq. (3.5) is also given by the bilinear form of the Majorana fermion:

$$\mathcal{R}(\{\eta_r\}) = \frac{1}{2}\sum_{jk} B_{jk}(\{\eta_r\})c_j c_k, \tag{3.6}$$

where $B(\{\eta_r\})$ is a Hermitian matrix. To evaluate Eq. (3.3), we separate the sum over the states into $\{c_j\}$ and $\{\eta_r\}$ parts:

$$I(\omega) = \frac{1}{Z}\sum_{\{\eta_r=\pm 1\}} \bar{I}(\omega;\{\eta_r\})e^{-\beta F_f(\{\eta_r\})}, \tag{3.7}$$

with

$$\bar{I}(\omega;\{\eta_r\}) = \frac{1}{Z_f(\{\eta_r\})}\mathrm{Tr}_{\{c_j\}}\left[\frac{1}{N}\int_{-\infty}^{\infty} dt e^{i\omega t}\mathcal{R}(t;\{\eta_r\})\mathcal{R}(\{\eta_r\})e^{-\beta\mathcal{H}(\{\eta_r\})}\right], \tag{3.8}$$

where $Z = \sum_{\{\eta_r=\pm 1\}} e^{-\beta F_f(\{\eta_r\})}$ and $Z_f(\{\eta_r\}) = e^{-\beta F_f(\{\eta_r\})} = \mathrm{Tr}_{\{c_j\}} e^{-\beta\mathcal{H}(\{\eta_r\})}$. By applying Wick's theorem to Eq. (3.8), we calculate the Raman spectrum at $\omega(\neq 0)$ for a given configuration $\{\eta_r\}$ as

$$\begin{aligned}\bar{I}(\omega;\{\eta_r\}) =& \frac{1}{N}\sum_{\lambda\lambda'}\Big[2\pi|C_{\lambda\lambda'}|^2 f(\varepsilon_\lambda)[1-f(\varepsilon_{\lambda'})]\delta(\omega+\varepsilon_\lambda-\varepsilon_{\lambda'}) \\ &+ \pi|D_{\lambda\lambda'}|^2[1-f(\varepsilon_\lambda)][1-f(\varepsilon_{\lambda'})]\delta(\omega-\varepsilon_\lambda-\varepsilon_{\lambda'}) \\ &+ \pi|D_{\lambda\lambda'}|^2 f(\varepsilon_\lambda)f(\varepsilon_{\lambda'})\delta(\omega+\varepsilon_\lambda+\varepsilon_{\lambda'})\Big],\end{aligned} \tag{3.9}$$

where $f(\varepsilon) = 1/(1+e^{\beta\varepsilon})$ is the Fermi distribution function with zero chemical potential, $\{\varepsilon_\lambda\}$ is the set of the positive eigenvalues of A with the eigenvectors $\{\boldsymbol{u}_\lambda\}$, and the matrices C and D are given by $C_{\lambda\lambda'} = 2\boldsymbol{u}_\lambda^\dagger B\boldsymbol{u}_{\lambda'}$ and $D_{\lambda\lambda'} = 2\boldsymbol{u}_\lambda^\dagger B\boldsymbol{u}_{\lambda'}^*$. In the Monte Carlo simulations, we generate a sequence of configurations of $\{\eta_r\}$ to reproduce the distribution of $e^{-\beta F_f(\{\eta_r\})}$, and hence the finite-temperature spectrum is simply computed

as

$$I(\omega) = \bar{I}(\omega; \{\eta_r\})_{\mathrm{MC}}$$

being the Monte Carlo average.

3.6 Appendix B: Correction for optical constants.

According to the Beer-Lambert Law, the intensity of the laser decreases exponentially with the depth: $I[z] = I_0 e^{-\alpha z}$, where d is the depth and α is the attenuation constant, which is a function of laser frequency and dielectric constant of the material ($\alpha = \frac{\omega}{c}\mathrm{Im}[\tilde{n}(\omega)] = -\frac{4\pi E[\omega_0]}{hc} k[\omega_0]$). Alternatively one can express this in terms of a penetration depth indicating the length scale relevant to absorption: $\delta = \frac{1}{\alpha}$. Applying this to our experiment, for a certain depth d, we find the incident laser intensity as a function of distance from the surface, $I_{in}[\omega_0, z] = I_0 e^{-\frac{4\pi E[\omega_0]}{hc} k[\omega_0] z}$. Here, ω_0 is the frequency of the excitation laser, I_0 is the initial incoming laser power in front of the sample,and δ(≈140 nm) is much shorter than the thickness of α-$RuCl_3$ bulk crystal. To properly account for the temperature dependence of the optical constants on the measured Raman signal, it is crucial to account for these absorption losses. Specifically, the measured intensity is reduced by the absorption of the outgoing Raman photons, (i.e. $I_{out}[\omega, \omega_0, z] = I_{in}[\omega_0, z] e^{-\frac{4\pi E[\omega]}{hc} k[\omega] z}$) where ω is the frequency of the scattered light. Furthermore, one should also consider the probability of transmission at the surface of α-$RuCl_3$ ($T[\omega]$), which also depends on the Raman light frequency. Applying the transmission rate to the Raman signal, we obtain the Raman intensity coming out of the sample at each point $I_{Raman}[\omega, \omega_0, z] = I_{out}[\omega, \omega_0, z] * T[\omega]$. Finally, one obtains the signal intensity by integrating the attenuated intensity of scattering point at each depth via $I_{corrected}[\omega_0, \omega] = \int_0^{d_{max}} I_{Raman}[\omega, \omega_0, z] dz$[29]. All presented Raman data in this paper are corrected by this method using the previously published optical constants[69].

CHAPTER IV

Modulation doping in Van de Waals heterostructures

4.1 Introduction

Two-dimensional (2d) nano-electronics, plasmonics, and emergent phases require clean and local charge control, calling for layered, crystalline acceptors or donors. Our Raman, photovoltage, and electrical conductance measurements combined with *ab initio* calculations establish the large work function and narrow bands of α-$RuCl_3$ enable modulation doping of exfoliated single and bilayer graphene, chemical vapor deposition (CVD) grown graphene and WSe_2, and molecular beam epitaxy (MBE) grown EuS. We further demonstrate proof of principle photovoltage devices, control via twist angle, and charge transfer through hexagonal boron nitride (hBN). Short-ranged lateral doping (≤ 65 nm) and high homogeneity are achieved in proximate materials with a single layer of α-$RuCl_3$. This leads to the best-reported monolayer graphene (mlg) mobilities ($4,900$ cm^2/Vs) at these high hole densities (3×10^{13} cm^{-2}); and yields larger charge transfer to bilayer graphene (blg) (6×10^{13} cm^{-2}).

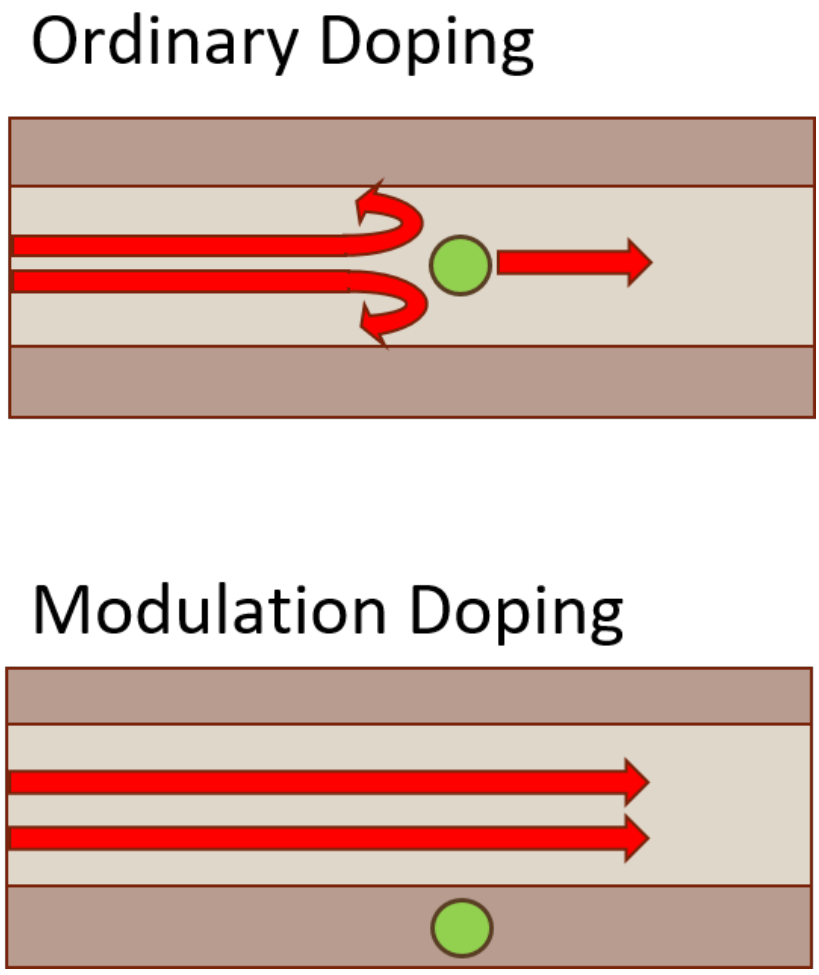

Figure 4.1: Cartoon of modulation doping, the light bring is the current channel and the green ball is the dopen, red arrow is the current flow.

Modulation doping in crystalline films[117] produced extreme carrier mobilities for fast/high power electronics [118], efficient optoelectronics [119–121], qubits [122], the fractional quantum Hall effect [123] and topological superconductivity [124]. However, two-dimensional (2d) van der Waals materials lack crystalline dopants for permanent, large, uniform, and local control of charge densities. Previous attempts utilized ionic liquid and polymer electrolyte gating [125–132], atomic/molecular intercalation, functionalization, and adsorption [133–137]. Densities exceeding 10^{14} cm^{-2} were achieved in graphene[126, 129, 133, 134, 136], though at significant cost to sample quality. Furthermore, these chemical approaches cannot be applied to air sensitive materials nor

specific layers of the heterostructure. Here, we show these limitations are circumvented with an insulating 2d material that acts as a crystalline acceptor.

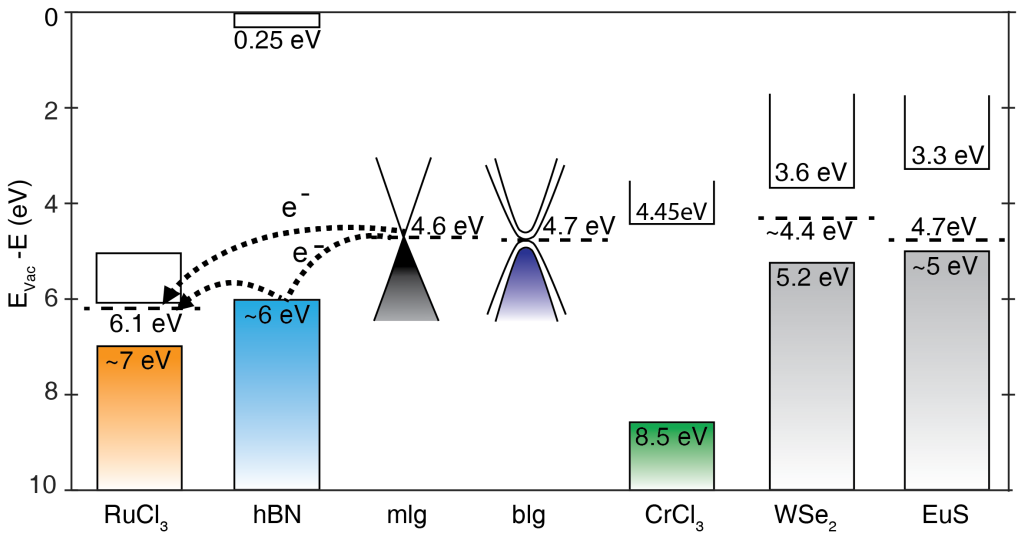

Figure 4.2: Band alignment schematic, the work function difference between α-$RuCl_3$ and other compounds yields charge transfer.

We focus on alpha-ruthenium(III) chloride (α-$RuCl_3$), a van der Waals, narrow-band Mott insulator with a deep work function of 6.1 eV (Fig. 4.2),[138] far greater than the typical work functions of layered materials ($\approx$ 4.5 eV). In α-$RuCl_3$ the onsite Coulomb repulsion (U) and strong spin-orbit coupling (λ_{SOC}) produce strongly narrowed valence and conduction bands that are just 1 eV apart with the Fermi level close to the conduction band edge [138, 139]. Taken together these properties imply α-$RuCl_3$ will accept a large density of electrons. This electronic structure also makes α-$RuCl_3$ a good insulator [140, 141], and thus is unlikely to interfere with electrical measurements. Further isolation is possible by using an hBN spacer, through which α-$RuCl_3$ still draws charge. Additionally, this unique electronic structure produces complex magnetic interactions in α-$RuCl_3$ [142, 143], placing it close to a Kitaev spin liquid phase. Thus heterostructures could enable novel magnetic states[144] and incorporate the topological excitations of α-$RuCl_3$ into devices. Lastly, for mid-IR plasmonic and optoelectronic applications,α-

$RuCl_3$ has minimal optical absorption[139] below the 1 eV gap.

4.2 Experiment methods

To establish α-$RuCl_3$ as a crystalline acceptor and bring modulation doping to 2d crystals, we employ spatially resolved Raman spectroscopy. This allows rapid probing of the induced charge, strain, homogeneity, lateral and vertical extent of the charge transfer in a variety of α-$RuCl_3$ heterostructures, without fabrication. Our results provide the first unambiguous evidence that even a single layer of α-$RuCl_3$ is able to strongly charge the target layer even when hBN is between them, including higher doping in bilayer graphene. A variety of proof of principle experiments further point to its utility: creation of a p-p' homojunction for 2D optical sensors and electronics; charge transfer to chemical vapor deposition-grown (CVD) graphene and WSe_2, as well as molecular beam epitaxy-grown EuS. In the latter case, the effect on EuS delivered a four-orders-of-magnitude reduction of the measured resistance and an induced hole density of 6.5×10^{13} cm^{-2} predicted by *ab initio* "mismatched interface theory" (MINT)[145]. Our combined Raman, transport and MINT results also point to the ability to tune the charge transfer via twist angle, with minimal induced strain, crucial for achieving clean modulation doping with short lateral extent ($\leq$ 65 nm). This rather small length scale is consistent with theoretical calculations for the formation of pn junctions in graphene due to mismatched workfunctions with metal contacts as well as recent near-field IR experiments[146]. The short range also requires careful optimization to minimize inhomogeneous charge transfer, which we find can be screened for using Raman spectroscopy, leading to clean devices with a single, highly-doped conducting channel and the highest mobilities ($4,900$ cm^2/Vs) of graphene charged to a similar level.

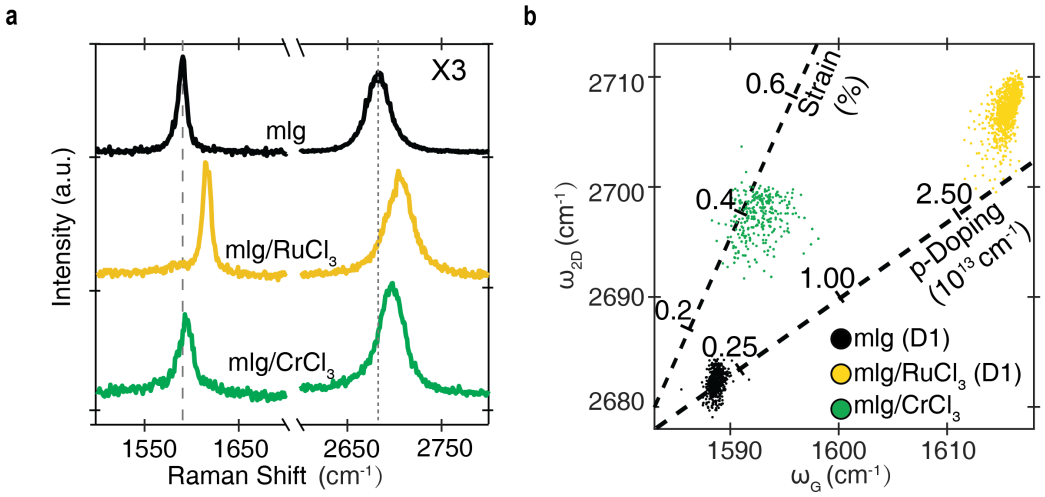

Figure 4.3: **(a)** Representative Raman spectra for mlg (black trace), mlg/$RuCl_3$ (yellow trace), and mlg/$CrCl_3$ (green trace) samples. **(b)** Correlation between the graphene G and 2D Raman mode for different mlg-based heterostructures, result of only strain or doping indicated with dashed lines.

Recently electronic transport experiments[140, 147] and first-principles calculations[145, 148] also suggested α-$RuCl_3$ can dope mlg to hole densities of a few 10^{13} cm^{-2}. However the two experiments also showed Dirac points close to zero gate voltage. Furthermore, the Hall and quantum oscillation data imply multiple carrier densities or a splitting of the Dirac cone. As we show through careful Raman studies, these features resulted from regions where the two materials do not touch. Indeed, since transport averages over the whole device it will include contributions from both the nearly charge neutral and strongly hole doped regimes. Creating uniformly doped samples is crucial for eventual device functionality and, according to electronic structure calculations, will strongly effect the electronic properties of the combined system. Beyond disorder, the lateral and vertical extent of the charge transfer, dependence on layer number and relative rotation, ability to charge dope materials beyond mlg, and prototypical devices remain unexplored.

4.3 Modulation doping in 2D heterostructures

We begin with device (D1), a single monolayer graphene sheet laid across both mono- and bilayer α-$RuCl_3$, all supported by a SiO_2/Si substrate. This and the other structures measured in this work represent a new class of devices, incorporating α-$RuCl_3$- or hBN-supported graphene that either lack contacts or have etched contacts at the graphene edge [149]. This ensures that the interface between graphene and α-$RuCl_3$ is not affected by the presence of metallic leads. The room-temperature Raman spectra is shown in Fig. 4.3 for D1 of the pure mlg and mlg/$RuCl_3$ regions. In the former, we observe G and 2D Raman peaks whose positions $(\omega_G^0, \omega_{2D}^0) = (1581.6 \pm 0.2 \text{ cm}^{-1}, 2676.9 \pm 0.7 \text{ cm}^{-1})$ lie within the range of accepted values for intrinsic graphene with small amounts of local strain and doping from the SiO_2 substrate [150–152]. In clear contrast, in device regions containing graphene in contact with α-$RuCl_3$, the G and 2D peaks are both significantly blue shifted by 30 cm^{-1} and 22 cm^{-1}, respectively, indicating sizable charge transfer.

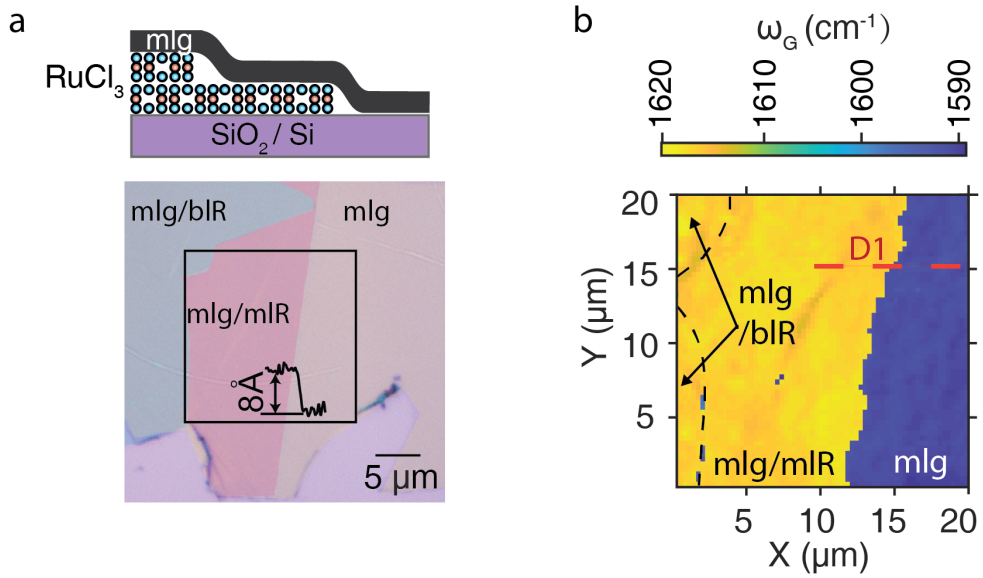

Figure 4.4: **(a)** False-color optical micrograph of D1, mlR is monolayer $RuCl_3$, blR is bilayer $RuCl_3$ and R means $RuCl_3$. Atomic force microscope of monolayer α-$RuCl_3$ step height (Inset). The black square marks the area scanned in **(b)**Raman maps of the graphene G peak frequency for different α-$RuCl_3$ heterostructures, with schematics of each heterostructure above their respective maps.

4.3.1 Doping level

The doping and strain corresponding to the G and 2D peak shifts are determined following a well established procedure[151, 152]. In Fig. 4.3b, we plot the established calibrations for pure strain and doping along with the distributions of peak shifts for the pure mlg and mlg/$RuCl_3$ regions in D1, taken from a spatially-resolved Raman map (Fig. 4.4b). The observed peak shifts in mlg/$RuCl_3$ indicate an induced average carrier density of $\sim 3 \times 10^{13}$ cm^{-2}, similar to previous reports [140, 147] and predictions [145, 148]. The charge density variations in each device are smaller than the differences between the average values. As discussed below, we associate this with the (uncontrolled) relative twist angle between the graphene and α-$RuCl_3$. To determine the strain, we assumed it was uniaxial since i) MINT[145] calculations indicate it is dominant, and ii) this provides

better agreement with experiment compared to a biaxial strain model. No correlation is found between doping and strain, with the latter being quite small ($< 0.2\%$).

To determine whether this charge transfer capability is unique to α-$RuCl_3$ or is generic to all layered halides, we investigate devices incorporating $CrCl_3$, a magnetic semiconductor with a similar lattice structure to α-$RuCl_3$. Our DFT calculations show the conduction band of $CrCl_3$ is quite close to the Dirac point of graphene (Fig. 4.3), suggesting it cannot drive a large charge transfer. As expected, the measured Raman spectra (Fig. 4.3a) together with a scatter plot of the peak positions (Fig. 4.3b) from a SiO_2/$CrCl_3$/mlg/hBN stack reveal shifts of the 2D peak alone, while the G peak remains essentially unchanged. Thus $CrCl_3$ primarily produces a strain in the adjacent graphene layer, confirming that charge transfer is not a generic feature of layered halides.

4.3.2 Thickness dependence

Next we turn to the thickness dependence of the charge transfer between α-$RuCl_3$ and graphene layers. First we studied the spatially-resolved map of the Raman G peak frequency for device D1 shown in Fig. 4.4, since this mode has the strongest dependence on the carrier density in mlg. Surprisingly, there is no noticeable change in the G peak frequency of graphene when the laser spot crosses from monolayer α-$RuCl_3$ to bilayer α-$RuCl_3$, indicating a single monolayer is sufficient to induce the large hole density.

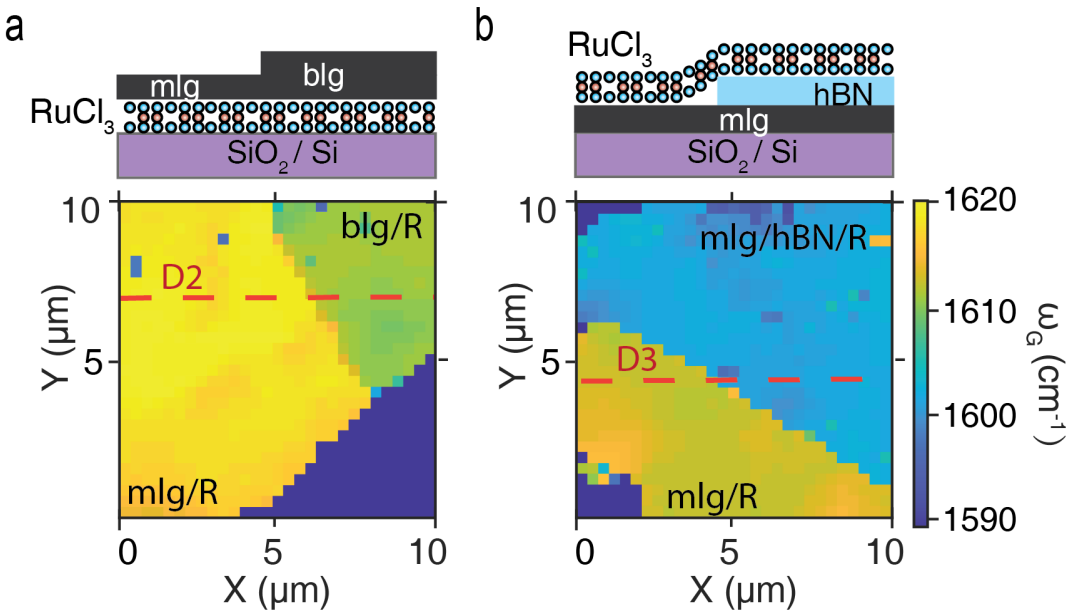

Figure 4.5: Raman maps of the graphene G peak frequency for different α-$RuCl_3$ heterostructures, with schematics of each heterostructure above their respective maps.

The same is not true for graphene, where we find that bilayer is more heavily doped than mlg. Specifically, we measured a heterostructure device (D2) having contiguous mono- and bilayer graphene, each partially covering the same flake of α-$RuCl_3$. We compare the G-peak frequency of the blg/$RuCl_3$ and mlg/$RuCl_3$ regions in a map (Fig. 4.4b) and the G/2D distributions in (Fig. 4.10). Both show the G and 2D peak shifts are smaller in blg/$RuCl_3$ than in mlg/$RuCl_3$. However, the density of states is larger in blg, and thus the G peak shift for the same carrier density will be less as it depends on the Fermi level. We find the resulting average carrier density in blg (6×10^{13} cm^{-2}) is higher than in mlg (3×10^{13} cm^{-2}). In tandem, we perform self-consistent density-functional theory (DFT) calculations for blg/α-$RuCl_3$ implemented for AA- and AB-stacked blg. In both cases we find a larger charge transfer from α-$RuCl_3$ into blg than mlg (Fig. 4.12e).

Inspired by traditional modulation doping that employs an intermediate insulating

layer to separate donors/acceptors from the charged layer, we explored a third device design. Device D3 contains three regions of bare mlg, mlg and α-$RuCl_3$ in direct contact, as well as mlg and $RuCl_3$ separated by ≈3-nm-thick hBN. As the valence band maximum of hBN is closely aligned with the work function of α-$RuCl_3$ (Fig. 4.2), we anticipate the insulating barrier will reduce—but not entirely eliminate—charge transfer from the mlg. Indeed, the spatially resolved G peak map of D3 (Fig. 4.5a, along with the distribution of 2D and G peak positions (Fig. 4.10), are consistent with the hBN spacer lowering the induced hole density in mlg to 0.6×10^{13} cm^{-2}. Our DFT calculations of mlg/hBN/$RuCl_3$ heterostructures suggest this doping is tunable via an inverse relation between the charge transfer and the intermediate hBN thickness (Fig. 4.5b).

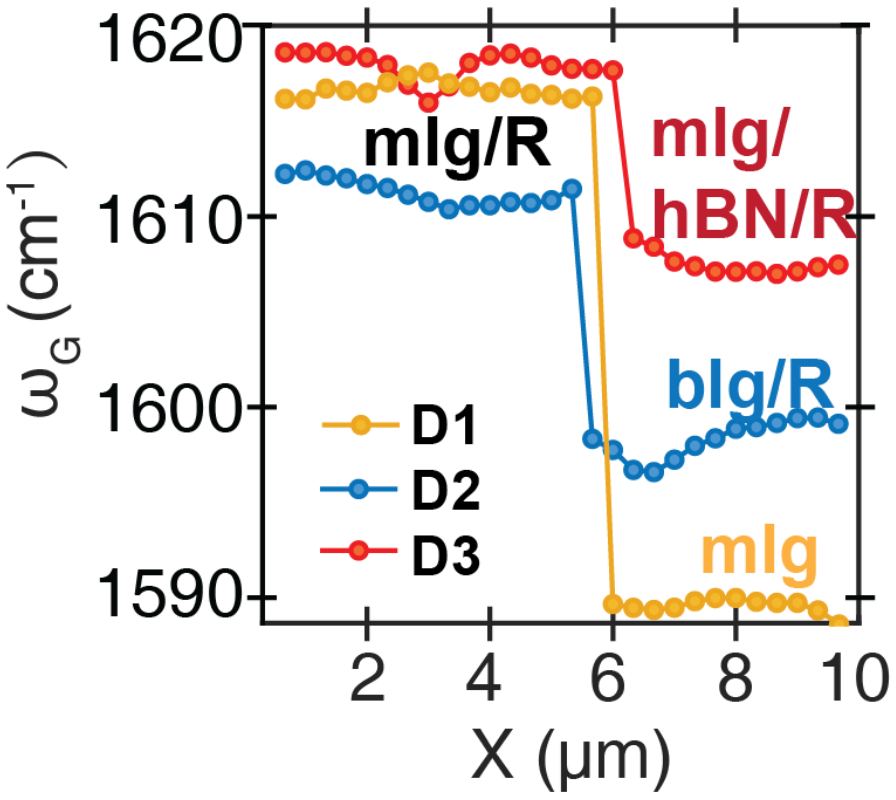

Figure 4.6: Horizontal linecuts of the G peak frequency across the lines indicated in previous devices, revealing the sharp doping change.

The G peak maps of devices D1, D2, and D3 all indicate the lateral charge transfer

is short, changing abruptly across the α-$RuCl_3$ boundary. This is illustrated via the linecuts in Fig. 4.6, which reveal the doping transition is shorter than the 0.3 μm scanning resolution.

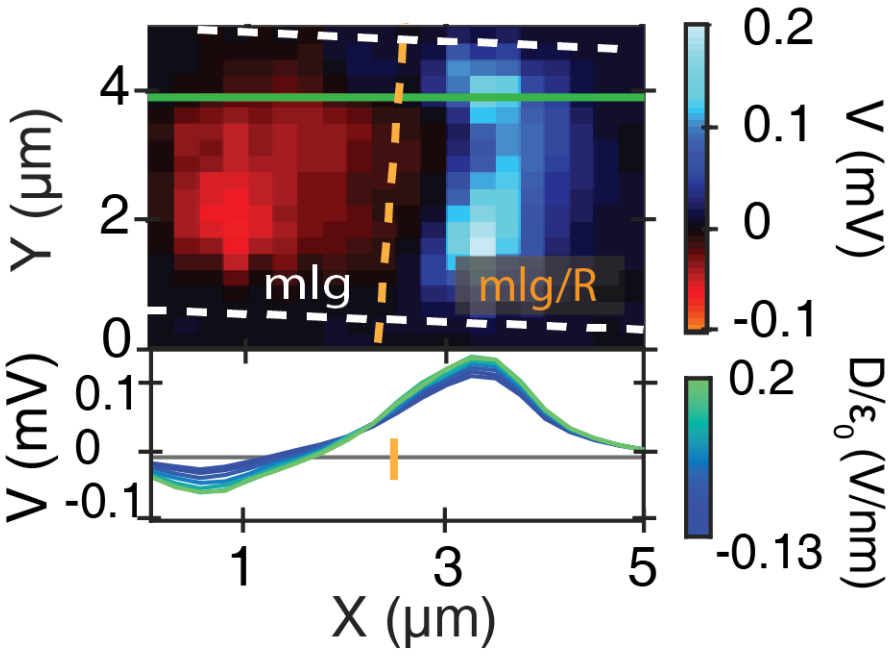

Figure 4.7: Top, scanning photovoltage map of mlg/α-$RuCl_3$ heterostructure acquired at room-temperature with a 532 nm laser. Mlg is between the white dashed lines, while right of the orange dashed line is covered by α-$RuCl_3$. Bottom, Gate voltage dependence of the photovoltage along the green linecut in the scanned photovoltage map, consistent with a p-p' lateral junction.

The potential utility of this sharp doping profile is demonstrated in room temperature photovoltage measurements shown in Fig. 4.7 for device D4, a graphene channel partially covered with α-$RuCl_3$. The photovoltage map shows a clear photoresponse at the boundary of the $RuCl_3$ region, indicating the presence of a p-p' junction leading to a photovoltaic effect. The width of the response is consistent with the spot size of our laser ($\approx 1\mu$m) suggesting a sharp doping profile. We ruled out photothermal effects[153] by testing both the polarization dependence and the minimal effect of a displacement field D (line scans in Fig. 4.7). The response seen in graphene not covered by α-$RuCl_3$ is likely due to inhomogenous local doping. Indeed, the photovoltage from the uncovered

region is suppressed by D, whereas the α-$RuCl_3$ covered region response is insensitive to D. As such these results show the potential of α-$RuCl_3$ in creating homojunctions of different carrier densities for optoelectronic devices.

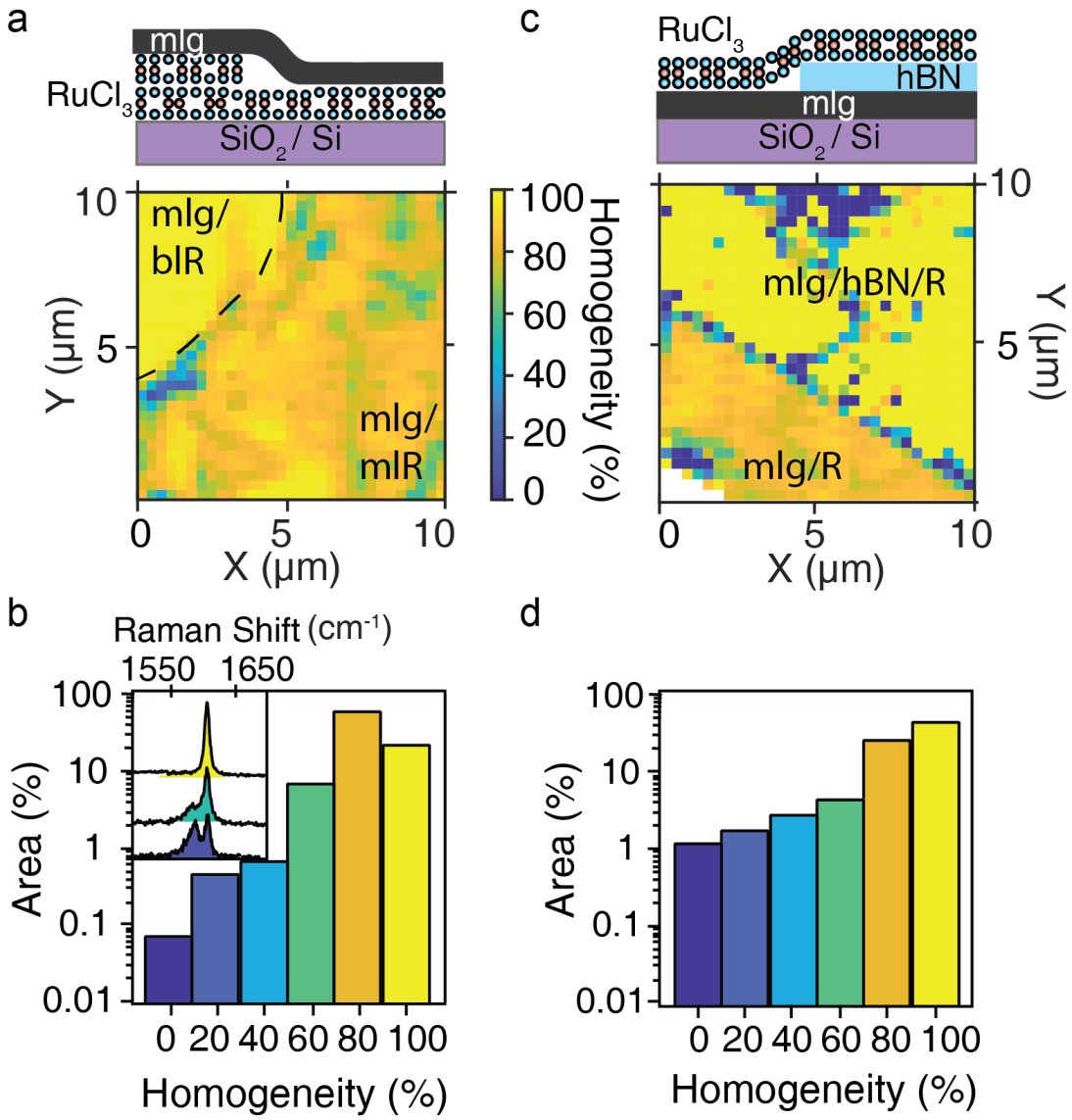

Figure 4.8: **(a & c)** Spatially-resolved homogeneity maps for D1 & D3, respectively, with stacking schematics depicted above. **(b & d)** Histograms of the homogeneity values for each map. B Inset, three representative Raman spectra from D1 with varying weights of shifted and unshifted peaks, showing the different homogeneity.

Similarly crucial is the homogeneity of the induced charge. Given the short lateral

extent, regions where the α-$RuCl_3$ is not in good contact with graphene could have little to no induced charge, yielding a Raman spectra with both shifted and unshifted peaks, as shown by the spectra at three different locations of device D1 (inset of Fig. 4.8b). A combination of shifted and unshifted G peaks indicates the presence of both fully doped and charge neutral regions, which likely occurred in previously reported devices. We confirmed this by applying a gate voltage, which moved the center of the unshifted peaks, but not the shifted G peaks as they come from regions with large carrier density. The relative size of each region within the laser spot is correlated to the spectral weight of the shifted and unshifted peaks, with some spectra (yellow shaded trace in Fig. 4.8b inset) revealing no neutral regions. Whether unshifted peaks are present or not, the shifted peaks always appear at the same energy. This is consistent with extremely short-ranged lateral charge transfer, leading to undoped puddles within doped regions with nearly constant induced density. Note that if the chemical potential in α-$RuCl_3$ were spatially inhomogeneous, we would expect a corresponding distribution of doping in graphene that is not seen in the G peak shifts.

4.3.3 Doping homogeneity

To quantify the uniformity, we define homogeniety to be 100% when only a shifted G peak is present, whereas 0% homogeneous regions exhibit shifted and unshifted peaks with equal spectral weight. We then quantify the device homogeneity as $(2 \times I_{\text{norm}}) - 1$, where I_{norm} is the intensity of the shifted G peak normalized by the sum of intensities of both peaks. The map of sample D1's homogeneity, shown in Fig. 4.8a, reveals a sub-micron spatial variation. We find some regions with 95% homogeneity, indicative of neutral regions $\leq$65 nm in radius, given our 300 nm resolution. The homogeneity improves for graphene in contact with bilayer vs. monolayer α-$RuCl_3$ due to better mitigation of the surface roughness of the underlying SiO_2 substrate. Further consistency with our picture that the interface quality is crucial to uniform doping is provided by

device D3 (4.8c). Here regions with atomically-flat hBN show improved homogeneity, also revealed in histograms of the homogeneity values for D1 and D3 (see Fig. 4.8b & d. These results imply that Raman spectroscopy can be used to pre-screen samples, enabling the deterministic fabrication of clean and homogeneous devices.

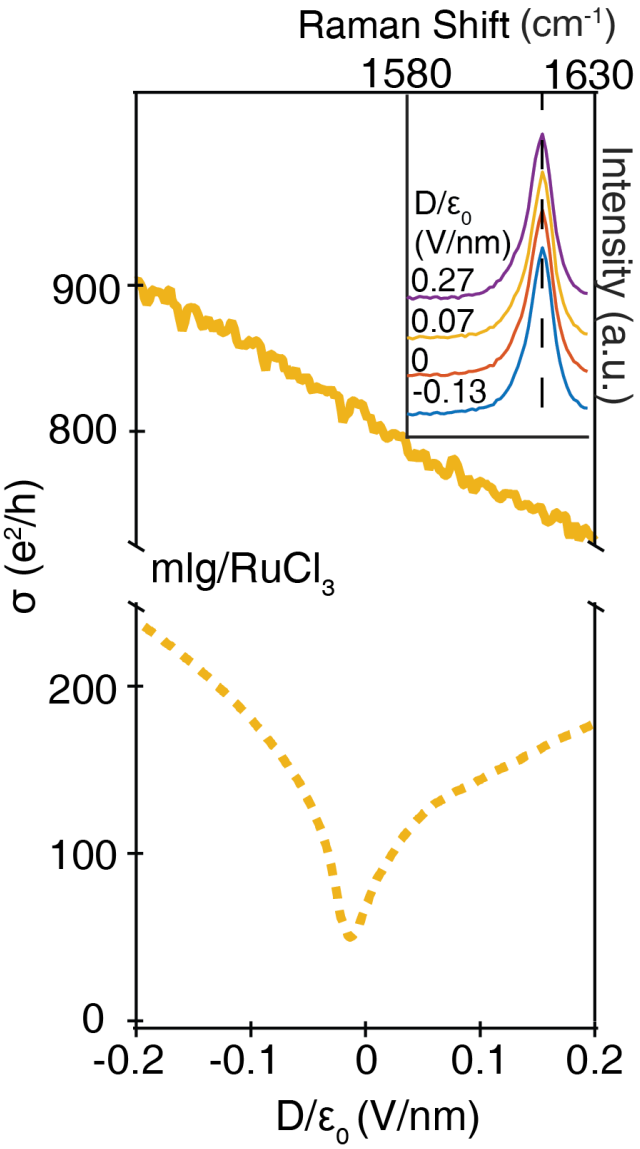

Figure 4.9: Comparison of conductivity versus displacement field for a $RuCl_3$/mlg/SiO_2 device with surface contacts between the mlg and α-$RuCl_3$ (dashed) and a fully encapsulated, edge-contacted hBN/mlg/$RuCl_3$ device (solid) device. Inset, D-dependence of mlg/$RuCl_3$ Raman G peak.

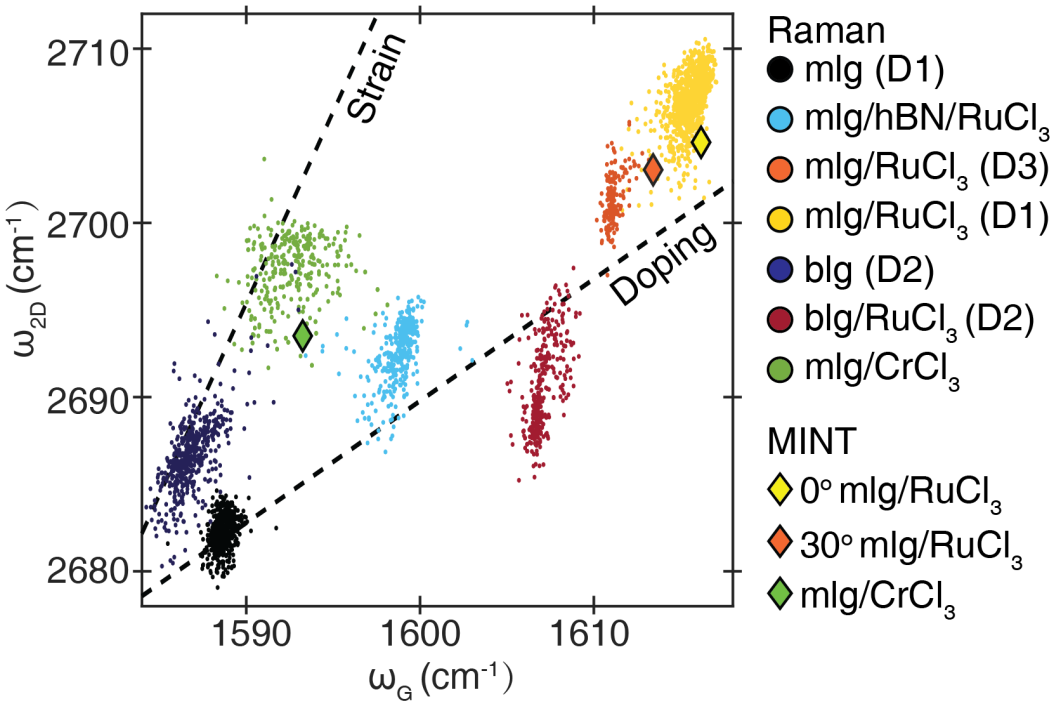

Figure 4.10: Correlation between the graphene G and 2D Raman mode for all samples discussed in the text (dots), as well as converted MINT results (diamonds) for different twist angles.

These observations resolve outstanding issues in mlg/α-$RuCl_3$ devices. Specifically the appearance of a Dirac point near zero gate voltage in otherwise extremely conductive and highly-hole-doped graphene (Fig. 4.9). The Raman maps for these devices exhibit lesser homogeneity (Fig. 4.4a & 4.8a) due to numerous neutral regions (unshifted G peak). In contrast, Raman maps in our new devices with smoother interfaces reveal improved homogeneity measured by the absence of neutral regions (4.8c). Meanwhile, the conductivity minimum is lacking in similar devices, as seen in the solid yellow transport trace shown in Fig. 4.9. Here the Shubnikov-de Haas oscillations show a single population of holes with no additional charge carrier populations. Transport in device D5 in Fig. 4.9 yields the largest mobility, $4,900$ cm^2/Vs, for single band transport in graphene at correspondingly large densities (3×10^{13} cm^{-2}). Competing

doping methods, in particular solid electrolyte gating, produce higher densities but result in significant disorder and lower mobilities (see Supplemental Table 1). Preliminary measurements suggest that increasing the distance between the α-$RuCl_3$ and graphene yields improved sample mobility at the expense of induced charge in the graphene, analogous to conventional modulation doping in 2d electron gases [117]. Further studies are required and will be the subject of future work.

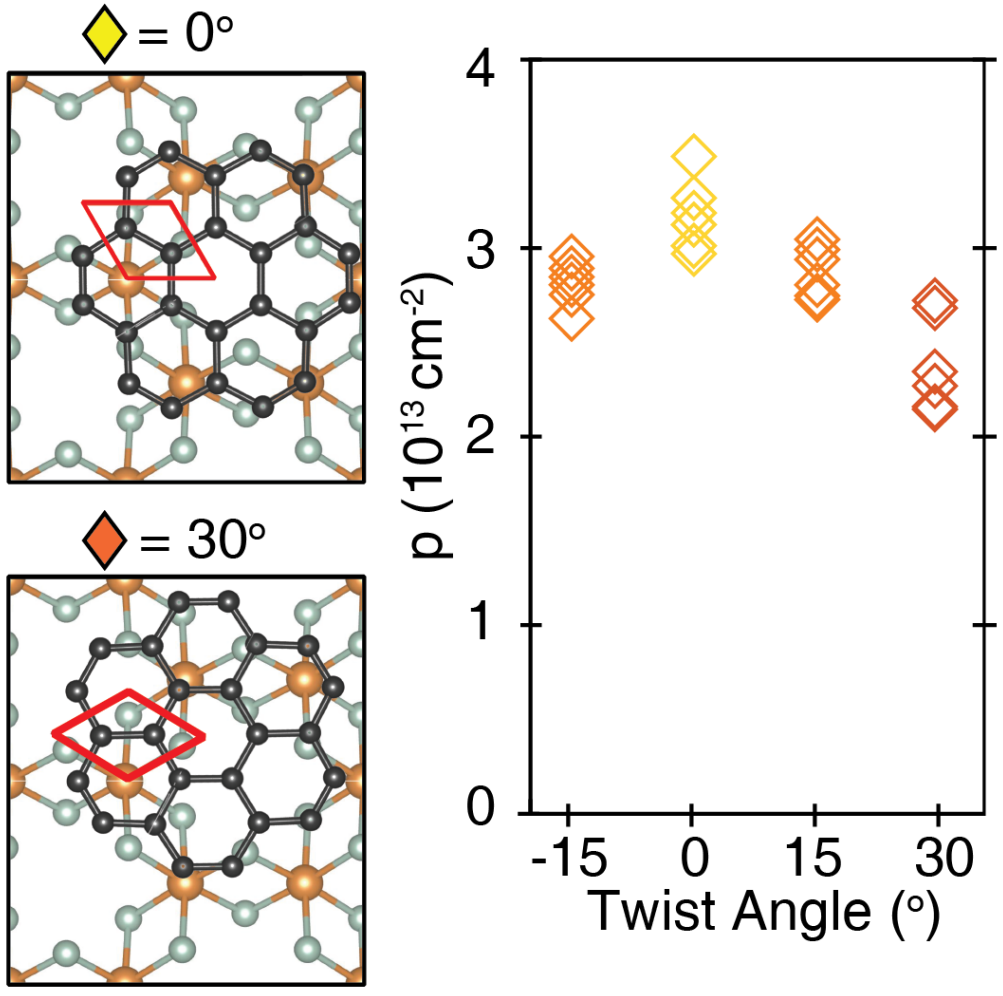

Figure 4.11: **(a)**Representative MINT supercell alignments for 0° (top) and 30° (bottom) mlg/$RuCl_3$ twist angles. **(b)** MINT-calculated mlg doping levels for six graphene supercell positions at different relative twist angles.

4.3.4 Angular dependence of the doping level

Lastly we explain the range of charge transfer in α-$RuCl_3$ heterostuctures via the relative twist angle. Our devices and previous reports indicate a large variation in hole densities over 2–4 $\times$ 10^{13} cm^{-2} [140, 147], far greater than the spread within a single device ($\delta p \approx$ 1–5 $\times$ 10^{12} cm^{-2}) (Fig. 4.10). Rotating the layers relative to one another changes the overlap between the Ru d and p orbitals, impacting the charge transfer. To this end, Fig. 4.11 shows MINT results for charge transfer at specific angles of the graphene relative to α-$RuCl_3$. The largest (smallest) charge transfer occurs at an angle of 0° (30°). The calculated carrier densities and strains for these two angles, converted to G and 2D peak frequencies, are plotted in Fig. 4.10a as orange and yellow diamonds, respectively, in close correspondence to the results for devices D1 and D3. The MINT results for a range of angles, shown in Fig. 4.11, indicate continuous tuning of the charge transfer due to a change in orbital overlap.

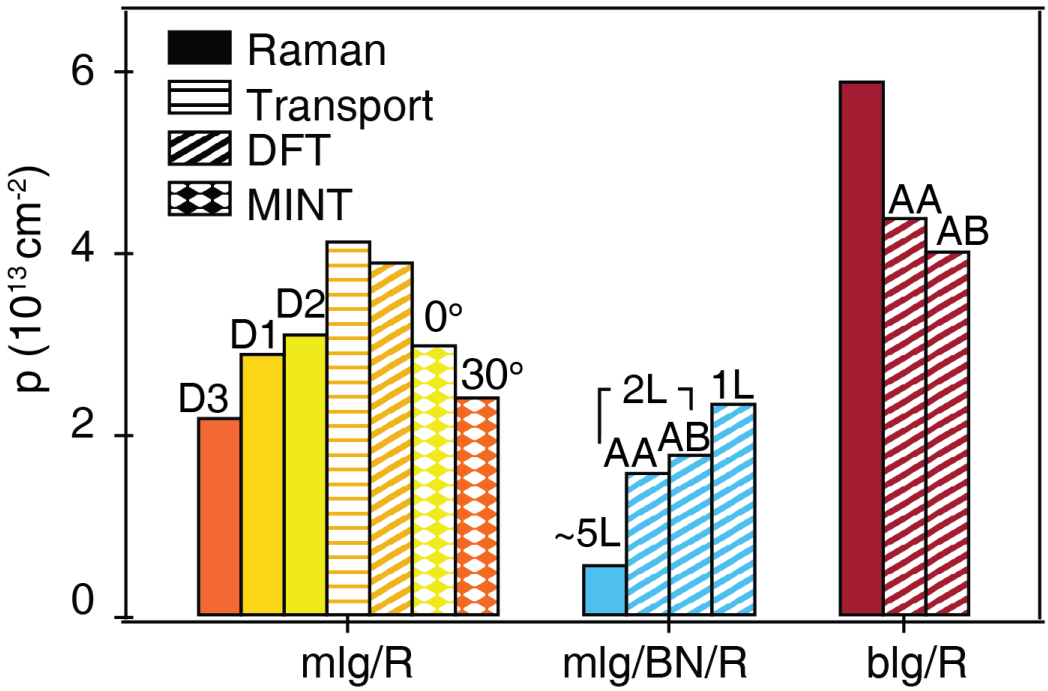

Figure 4.12: Doping levels calculated from Raman spectroscopy (filled bars), transport (horizontally striped bars), DFT (diagonally striped bars), and MINT (diamond-checkered bars).

4.4 Summary and outlook

In principle, similar effects could emerge from a low work function material acting as a 2D crystalline donor. As such, modulation doping can be introduced into 2d heterostructures with far reaching implications. For example, one can uniformly or locally charge a 2D material by controlling the regions over which it touches a crystalline acceptor or donor. This enables a new regime of 2d plasmonics, improved electrical transparency of contacts by locally doping the contacted layer, and the creation of lateral pn junctions. Such devices will require expanding the doping to a wider set of 2d materials, as suggested by Fig. 4.2, our preliminary MBE EuS, CVD graphene and WSe_2 results. Furthermore, the large and local electric fields in α-$RuCl_3$ will break inversion symmetry. As such they should enable new nonlinear responses in 2d materials and

tune the spin-orbit coupling. Thus, when combined with magnetic 2d atomic crystals, α-$RuCl_3$ could provide new spintronic devices and topological phases such as skyrmion lattices and spin liquids. Indeed an important question for future studies is the interplay between the magnetism and charge transfer in α-$RuCl_3$ heterostructures.

CHAPTER V

One magnon non-Loudon-Fleury Raman scattering in the Kitaev magnet

5.1 Introduction

We investigate the magnetic excitations of the hyperhoneycomb Kitaev magnet β-Li_2IrO_3 by means of inelastic Raman scattering. The spectra exhibit a coexistence of a broad scattering continuum and two sharp low-energy peaks at 2.5 meV and 3 meV, with a distinctive polarization dependence. While the continuum is suggestive of fractional quasi-particles emerging from a proximate quantum spin liquid phase, the sharp peaks provide the first experimental signature of the 'non-Loudon- Fleury' one-magnon scattering processes proposed recently[154]. The corresponding microscopic mechanism is similar to the one leading to the symmetric off-diagonal exchange interaction Γ (as it involves a combination of both direct and ligand-mediated exchange paths), but is otherwise completely unexpected within the traditional Loudon-Fleury theory of Raman scattering. Here we focus on β-Li_2IrO_3, which is the simplest of the 3D harmonic honeycomb structures. As shown in Fig. 5.1, β-Li_2IrO_3 is in Fddd space group and the Ir atoms are connected by zigzag bonds along c-axis orienting alternetively along **(a-b,a-b)** and **(a+b,a+b)** directions. At zero field, the system orders magnetically below T_c =38K. We present the temperature dependent Raman on this compound. In the

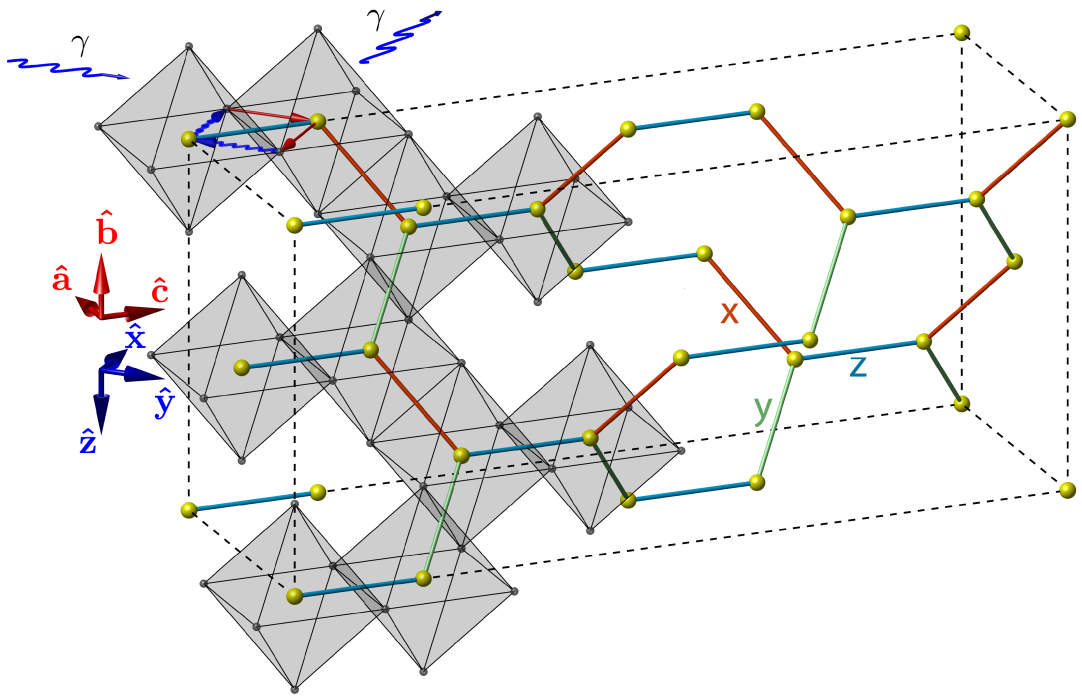

Figure 5.1: (a) Hyperhoneycomb network of Ir^{4+} ions (yellow spheres) in β-Li_2IrO_3. Each octahedron denotes a IrO_6 cage.

Raman susceptibility, we observe two kind of magnon scattering below T_c, the spectral weight(SW) shift from one to the other with temperature rising, which suggest the phase transition from spiral to zigzag. The Raman susceptibility also show a broad continuum at the same temperature range resulting from fractiona excitations, indicating the co-existance of magnons and spinons scattering.

In this study, we investigate the magnetic excitation spectrum in the ordered state of β-Li_2IrO_3 using Raman scattering. Our results reveal the first observation of the magnon and fractional excitations co-exsistence in spin $\frac{1}{2}$ frustrated 3D system and the temperature dependent phase transition between commensurate and incommensurate ordered states. The magnons also show the transition from spiral state to zigzag state.

5.2 Crystal growth, handling and characterization.

High-quality single crystals of β-Li_2IrO_3 were grown by a vapor transport technique. Ir (99.9$\%$ purity, BASF) and Li_2CO_3 (99.999 $\%$ purity, Alfa-Aesar) powders were ground and pelletized at 3,000 psi in the molar ratio of 1:1.05. The pellets were placed in an alumina crucible, reacted for 12 h at 1,050°C, and then cooled down to room temperature at 2 °C/h to yield single crystals which were then extracted from the reacted powder. β-Li_2IrO_3 crystallizes in the orthorhombic Fddd space group.

5.3 Raman spectroscopy setup.

The Raman spectra presented here were obtained on a custom built, low temperature microscopy setup [29, 143, 155]. A 532 nm excitation laser, whose spot has a diameter of 2 μm, was used with the power limited to 10 μW to minimize sample heating while allowing for a strong enough signal. The absence of laser induced heating was crucial to ensure the ordered state is achieved, and is confirmed via stokes/antistokes analysis as well as the appearance of magnons at the appropriate temperature. The single crystal was mounted by silver paint onto a copper sample holder and vacuum transferred onto *xyz* stage in in the cryostat [29]. At both room and base temperature (10 K), the reported spectra were averaged from three spectra in the same environment to ensure reproducibility. The spectrometer had a 2400 g/mm grating, with an Andor CCD, providing a resolution of $\approx 1\,\mathrm{cm}^{-1}$. Dark counts are removed by subtracting data collected with the same integration time with the laser blocked. To minimize the effects of hysteresis from the crystal structural transition, data was taken by first cooling the crystal to base temperature and then heating to the target temperature.

5.4 Experiment results

Fig.5.1 shows the crystal structure of β-Li_2IrO_3. The Ir atoms are connected by red and green zigzag bonds orienting alternetively along **(a-b,a-b)** or **(a+b,a+b)** directions. We choose these crystal surface because it is a natural crystal face and we can avoid artifacts of polishing the surface. Adjacent zigzag chains are stacked along c-axis connected by blue bonds. Different bond color suggest different direction dependent Kitaev interactions, which holds infinite degenerate state. A small perturbation from Kitaev interaction may induce various ordered magnetic states, such as commensurate zigzag order and incommensurate spiral order. The incommensurate state is unstable and can be replaced by commensurate by applying magnetic field along b-axis[156–158]. However, it is still unclear what is the temperature dependent relationship between them without external magnetic field.

Raman scattering is a powerful tool to study different state in β-Li_2IrO_3. It can preform high energy resolution and low noise level, which make it possible to observe small temperature dependent spectral change. In Fig.5.2, we show the Raman susceptibility measured at 10K. Via Stokes and anti-Stokes susceptibility ratio, we confirm the sample is in detailed balance without laser heating(see supplemental). The notation **(a-b,a-b)** and **(c,a-b)** refer to the incident and scattering beam polarization in the crystal structure frame. In both polarizations, the spectra show sharp phonons overlap on a broad continuum. The phonons follow the selection rule of *Fddd* space group and the continuum was characterized as fractional paricle excitations before, resulting from spin $\frac{1}{2}$ QSL system[78, 142, 159, 160]. As the Kitaev interactions in β-Li_2IrO_3 is anisotropic, $K_x \approx K_y \neq K_z$[157, 158], the continuum show overall higher intensity when the incoming light is **a-b** polarization. Besides the phonons and continuum, we note there are two well-defined sharp peaks at very low energy in **(c,a-b)**polarization.

To better understand these sharp features, we focus on polarization **(c,a-b)** and preform small step temperature dependent Raman. Shown in Fig.5.3b, two peaks

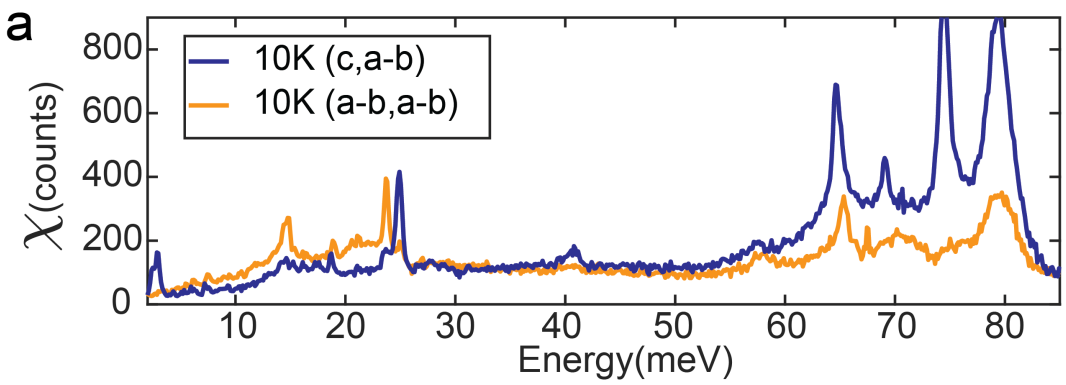

Figure 5.2: (a) Raman susceptibility of β-$LiIrO_3$ at 10 K, orange line shows (**a-b, a-b**) polarization, blue line is (**c, a-b**) polarization.

resolve at 2.5 meV(M1) and 3 meV(M2) at 10K. From 10K to 29K, M2 intensity decreases with temperature and merged into the high energy tail of M1, while M1 increases below 20K and start decreasing and softening when the temperature is around 25K and then disappear once the temperature reaches the T_C. Similar to QSL 1-D and 2-D examples[142, 161], these two peaks can be explained as magnons. Two different behavior magnons indicate two kinds of magnetic order and can be assigned to single-magnon excitation process. Two-magnon process from zone boundary is excluded because energetically the two-magnon feasure is predicted to be around 15meV and have no polarization dependence, which is also observed(Shown in supplemental). Furthermore, comparing the magnon peak with spinon dispersion at Γ point [158], one can decide $0.9\omega \approx$15meV, which is the zone boundary two-magnon energy. Then $0.3\omega \approx 3$ meV, which is the single-magnon energy and in good agreement with the Raman susceptibility result. As for the two kinds of magnetic order, it was showed by X-ray scattering that they can transit from one to the other with small field and their intensities follow the sum rule[156]. The incommensurate has higher energy and not as stable, we thereby can conclude M1 is related to commensurate state and M2 is incommensurate state signal. Without external magnetic field, two ordered phase co-exist below 25K, incommensurate state transit to commensurate state when temperature

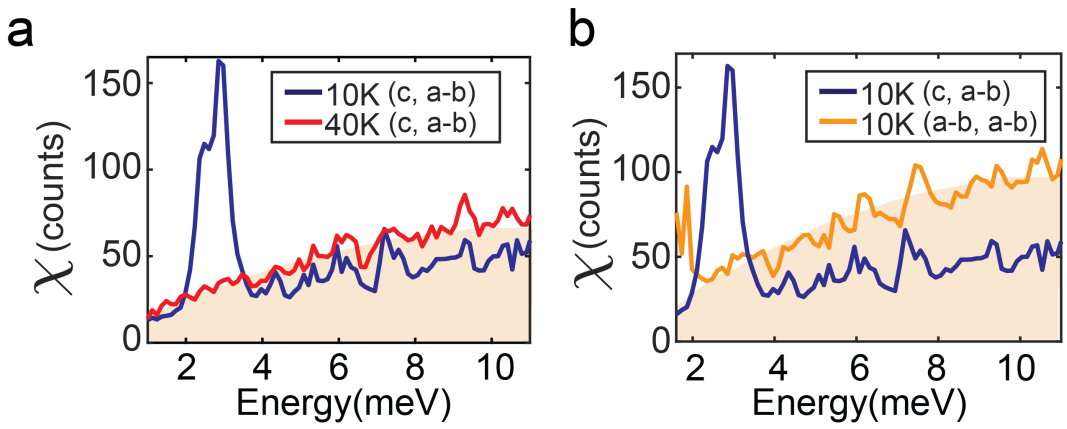

Figure 5.3: (a) Comparison of Raman susceptibility in the (**c,a-b**) channel at 10 K (blue) and 40 K (red).(b) Temperature dependence of the two low-energy peaks M1 and M2 seen in the (**c, a-b**) channel

.

rising.

The softening of M1 above 25K suggest a large magnon decay process and breaks down into the broad continuum at the end. Shown in Fig.5.3a, we plot both 10K and 40K of **(c,a-b)**. At 10K, the magnon and broad continuum coexist, while at 40K only broad continuum show up in the Raman susceptibility. The purple shade indicate the broad continuum from fractional excitations at 40K, and it is clearly stronger than the broad continuum at 10K.

The fact that the two low-energy peaks only exist below T_I implies that they can be assigned to magnons. To establish this we employ the recently revised theory of Raman scattering discussed in Ref. [154], the non-Fluery Loudon terms of β-Li_2IrO_3 give rise to a sharp, one-magnon peak in the (**a-c**) channel. Figure 5.4 shows this peak for the present case of (**c,a-b**) polarization. As discussed in Yang's paper, at the level of linear spin-wave (LSW) theory (dashed black line), the position of the peak is centered around $\omega_2 \simeq 2.8$ meV, close to the positions of the observed peaks M1 and M2. The same calculation for the **(a-b, a-b)** channel shows no peak at this energy range, consistent with the experimental results. This agreement on the position of the peak and its polarization

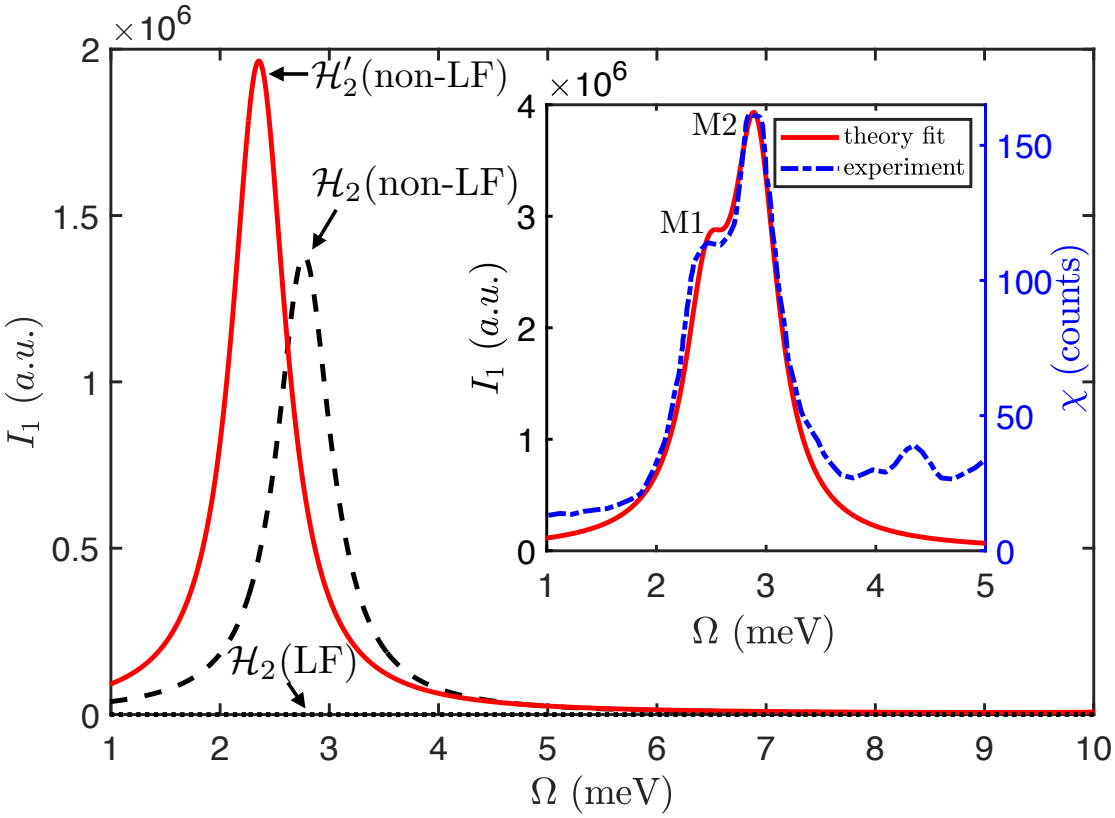

Figure 5.4: The one-magnon Raman response computed within the non-LF theory, at the level of linear spin wave theory (black dashed line) or with magnons renormalized by the quartic interactions $\mathcal{H}_4$ only (red solid line) [see detailed discussion in the SM], shows one low-energy sharp peak feature in the $(\mathbf{c}, \mathbf{a}-\mathbf{b})$ polarization channel. In contrast, the LSW theory with the LF Raman operator gives no low-energy features (black dotted line, not visible because the intensity vanishes). The inset shows the fit of the low-energy peaks M1 and M2 to the phenomenological model discussed in the SM .

dependence gives strong support to the one-magnon origin of one of the two peaks.

As the AF order in the low-temperature phase is reduced with increasing temperture towards TN one expects the spinon continuum to fill in at lower energies. It is therefore useful to consider the prerequisites for magnon break- down in the presence of the strongly anisotropic interactions.

Then we start talking about the integrations. In Fig.5.5a, we show the integration of different energy range of **(c,a-b)** polarization. For 1 to 4 meV, we include two of the magnons and 4.5 to 7.5 meV, we intensionally choose a similar integration energy

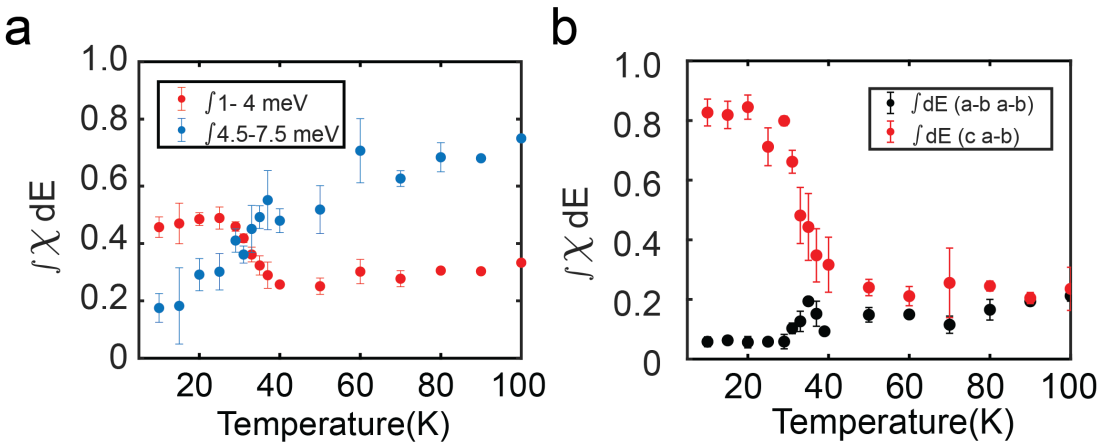

Figure 5.5: (a) The SW in (**c, a-b**) polarization: The red dots show the SW from 1 to 4 meV, which includes both M1 and M2 modes; the blue dots represent the SW from 4.5 to 7.5 meV, which incorporates a 3 meV interval of the broad continuum with no magnon contribution. (b) The SW from 2 to 4 meV vs T for (**a-b, a-b**) (black) and (**c, a-b**) (red) polarizations.

interval to the magnons, but in the only broad continuum energy range. We can see that in the figure, for the magnons part, the SW decrease with temperature and there is a turing point at 39K, which is the ordered temperature. While for the integration of only the broad continuum, the SW is keep increasing with temperature and there is also a turn point at Tc. For the Sw of the broad continuum , the temperature dependent behavior is intergration range independent(see supplemental.) After the Tc, both SW of magnon and continuum are parallel.magnon scattering at long wavelengths is strongly sensitive to cooling through TN , in stark contrast to the continuum

In Fig.5.5b, we show the integration of different polarizations. there is no magnon show up in the **(a-b,a-b)**, so we can only see the continuum behavior, but for **(c,a-b)**, it contains both continuum and magnon behavior.

5.5 Summary

In conclusion, our Raman scattering on the 3D frustrated Kitaev QSL β-Li_2IrO_3 demonstrates clearly the existence of both magnons and the broad continuum from

fractional excitations. We observed shift of intensity from M2 to M1 is consistent with the non-Fluery Loudon theory.

CHAPTER VI

Conclusions and outlook

6.1 Conclusions

In this dissertation, we have investigate the collective modes in charge density wave and multiple magnetic systems. In Chapter 2, we first reported the light pathway study of CDW Higgs mode in RTe_3 using Raman spectroscopy. In cross polarization channel, the asymmetric 2-fold intensity was observed, which was taken as the evidence of scattering pathway interference. The high intensity polarization angle indicated the constructive interference and the low intensity polarization angle indicated the destructive interference. With the band mixing from the 3D rare earth structure, the CDW vector could connects the p orbitals from the same or different bands. This resulted in the momenta change in the excitation pathway, which interfered with non momenta change excitation pathways. This result suggested the Higgs mode can be axial, which was only considered as a scalar for decades.

In Chapter 3 and 5, we discussed the temperature dependent Raman scattering in 2D and 3D spin liquid candidate systems, α-$RuCl_3$ and β-Li_2IrO_3 . In α-$RuCl_3$, the continuum from the fractional excitation was observed. The Raman susceptibility was fitted to Fermi statistics and also the QMC calculation, the agreement and divation suggested the Kitaev interaction range in temoerature and energy. In β-Li_2IrO_3 , the one magnon scattering was demonstrated below the Neel transition. The one magnon

can melt into the fractional excitaion transitions at higher tempertures. In addition to that, the one magnon process is different to the traditional Fluery-Loudon theory.

In Chapter 4, the application of the phonon mode was showed. In priciple, charge can flow from a high work function material to a low work function material. By stacking α-$RuCl_3$ with monolayer graphene, a large amount of electrons are transferred to α-$RuCl_3$, which has an extrmely deep work function. This process provides a clean way to highly p dope the graphene and can provide the carrier density as high as 3 X $10^{13} cm^{-2}$. As the dopens are not in the accepters, this process can be considered as modulation doping in 2D materials and has far reaching implications. For example, one can uniformly or locally charge a 2D material by controlling the regions over which it touches a crystalline acceptor or donor. This enables a new field of 2D material applications, such as generating plasmons, reducing electrode resistance and fabrication high quality p-n junctions.

6.2 Outlook

The work presented in this thesis can be naturally extended along many different directions. On one hand, the electronic Raman symmetry study can be applied to more CDW materials. In the RTe_3 series, there only exists one CDW when the center atom is ligter than Gd and one more CDW order perpendicular to the original one will show up at lower temperature when the central atom gets heavier, such as $ErTe_3$. This second CDW order could potentially lead to the symmetry change of the original CDW. For materials not included in the RTe_3 series, such as $NbSe_2$, the CDW Higgs mode symmetry is still a mystery. One can even add strain to destroy one of the CDW orders in this material and try to observe the changes of the other two.

On the other hand, the magnetic excitation in α-$RuCl_3$ and β-Li_2IrO_3 , can be extended or applied to other QSL candidate materials. Such as external magnetic field can tune the QSL candidate to gapless phase and Raman scattering could help to

characterize the new phases. Further experiment of other QSLs can also be performed in other 2D or 3D systems where the Neel transition temperature could be different.

In a more general perspective, the modulation doping in 2D heterostructures can be widely used. This thesis stacked α-$RuCl_3$ on one side of graphene but this can be extended to a sandwich structure, like $RuCl_3$/graphene/$RuCl_3$ structure, which could possibly double the carrier densities in graphene channel. In the area of device fabrication, the contact resistance is very important. Stacking $RuCl_3$ could provide contact with much lower resistance. In addition to that, patterned $RuCl_3$ could in principle provide periodic doping in other 2D materials.

Collective mode detection in quantum could lead to new physics insights and to the new emergent physics as well as a wide range of applications

ACKNOWLEDGEMENTS

Turn off the lasers, walk out of Higgins, enjoy the moonlight and the cherry blossoms on the hill. Yes, another day in the lab has come to end, the last day of my grad student life. Now, let me write down this section to extend all my deepest gratitude.

First of all I would like to acknowledge my advisor, Professor Kenneth S. Burch. Thank you for giving me the chance and trusting in my capabilities as a scientist. Thanks for your patience, time and efforts. Thanks for your precious advices throughout all these six years, on how to do things efficiently, how to communicate with others, how to give a presentation, on showing me how to write a scientific article word by word, how to select a project and so on, which will be useful for my whole life. I got the opportunity to learn and also got enough freedom to challenge myself. I really appreciate to work with you.

In addition to Ken, I would like to thank all the professors who are on my dissertation committee. Professor Ilija Zeljkovic, Professor Ying Ran, and Professor Fazel F. Tafti. During my time here each of you have been giving with your time and advices.

I could not have made all of this without the help of all Burch lab members. Thank you Gavin Osterhoult for your scientific advices and conversations on the fundamental physics concepts. Thank you Mason Gray for your practical help and training. Thank you Vincent Plisson, thanks for your patience and help, we spent a lot of time working together, fixing the setup, dealing with different technical and physics issues. Let's make more Montana coffee in the future. Thank you Narendra Kumar. I really learned a lot from you, not limit to all the nano-fabrication details. When I am exhausted, you are

the only one in the lab always convincing me to go home and have a rest and it turns out you are absolutely right on this. Thank you Mike Geiwitz, I really enjoy working and traveling you. Also thanks to Gabriel Natale. I have been lucky enough to have worked with and mentored several talented undergraduate student Grant McNamara, Tiffany Wang, Marisa Romanelli during my time at Boston College.

I am grateful to the many collaborators I have worked with during my PhD. In particular, Erik Henriksen and Jesse Balgley for study a lot of projects together, Leslie Shoop and Shiming Lei for providing us with many high quality crystals, Eun Ah Kim, and Eli Gerber for the computation help and Prineha Narang for the excellent theory work and the very helpful career guidance.

Then I would like to thank Boston College physics friends Dyler Dogde, Bryan Rachmilowitz, Faranak Bahrami, He Zhao, Xu Yang, Tong Yang.

In particular, Victoria Gabriele, my only classmate for six years. We share the same office in the physics department. I can still clearly remember the days we studied the comp exam and the days you asked me to try my first beer and first shot. But most important, research is not always easy, you are the one always encouraging me to trust myself.

Of course, I will thank my physics "Honor of Kings" team, Xiaodong Hu, Hong Li and Hanchen Liu. Although we always lost the game, sometimes 100 % defeated, we still got a lot of fun.

I extend my thanks to the administrative staff of the Boston College physics department. Scott Bortolotto, Nancy Chevry, Jane Carter. I thank Pual Dee and Robert Snee for machining a lot of important small parts for me. And I thank Walter for always telling me to smile and for keeping the department environment clean.

Next, I would like to thank all my friends who have been very supportive over the last six years. Wenhua Song, Yishu Wang, Xiaonan Jiang, Leqi Zhang, Qianwei Zhu, Xiyue Wu, Yu Wang, Jianing Xu, Siqi Chen, Xi Wang.

Lastly, I would thank my parents. Thanks for your love, support and understanding.

Doctoral studies pave a way for becoming a scientist. It really takes four to seven years, and for me, it is six. But I really don't feel it like that long and I will miss this six years all my life.

BIBLIOGRAPHY

[1] D. B. Franzosi, G. Cacciapaglia, H. Cai, A. Deandrea, and M. Frandsen, "Vector and axial-vector resonances in composite models of the higgs boson", Journal of High Energy Physics **2016**, 76 (2016).

[2] R. Shimano and N. Tsuji, "Higgs mode in superconductors", Annual Review of Condensed Matter Physics **11**, 103–124 (2020).

[3] D. Pekker and C. Varma, "Amplitude/higgs modes in condensed matter physics", Annual Review of Condensed Matter Physics **6**, 269–297 (2015).

[4] S. Klemenz, A. K. Hay, S. M. L. Teicher, A. Topp, J. Cano, and L. M. Schoop, "The role of delocalized chemical bonding in square-net-based topological semimetals", Journal of the American Chemical Society **142**, 6350–6359 (2020).

[5] V. Brouet, W. L. Yang, X. J. Zhou, Z. Hussain, R. G. Moore, R. He, D. H. Lu, Z. X. Shen, J. Laverock, S. B. Dugdale, N. Ru, and I. R. Fisher, "Angle-resolved photoemission study of the evolution of band structure and charge density wave properties in RTe_3 (R = Y, La, Ce, Sm, Gd, Tb, and Dy)", Phys. Rev. B **77**, 235104 (2008).

[6] S. Lei, J. Lin, Y. Jia, M. Gray, A. Topp, G. Farahi, S. Klemenz, T. Gao, F. Rodolakis, J. L. McChesney, C. R. Ast, A. Yazdani, K. S. Burch, S. Wu, N. P. Ong, and L. M. Schoop, "High mobility in a van der waals layered antiferromagnetic metal", Science Advances **6**, 10.1126/sciadv.aay6407 (2020).

[7] D. Podolsky, A. Auerbach, and D. P. Arovas, "Visibility of the amplitude (Higgs) mode in condensed matter", Physical Review B **84**, 174522 (2011).

[8] A. Zeilinger, R. Gähler, C. G. Shull, W. Treimer, and W. Mampe, "Single- and double-slit diffraction of neutrons", Rev. Mod. Phys. **60**, 1067–1073 (1988).

[9] Y. Zhang, Y.-W. Tan, H. L. Stormer, and P. Kim, "Experimental observation of the quantum hall effect and berry's phase in graphene", Nature **438**, 201–204 (2005).

[10] D.-X. Qu, Y. S. Hor, J. Xiong, R. J. Cava, and N. P. Ong, "Quantum oscillations and hall anomaly of surface states in the topological insulator Bi_2Te_3", Science **329**, 821–824 (2010).

[11] C. Ryu, E. C. Samson, and M. G. Boshier, "Quantum interference of currents in an atomtronic squid", Nature Communications **11**, 3338 (2020).

[12] J.-P. Cleuziou, W. Wernsdorfer, V. Bouchiat, T. Ondarçuhu, and M. Monthioux, "Carbon nanotube superconducting quantum interference device", Nature Nanotechnology **1**, 53–59 (2006).

[13] F. Giazotto, J. T. Peltonen, M. Meschke, and J. P. Pekola, "Superconducting quantum interference proximity transistor", Nature Physics **6**, 254–259 (2010).

[14] S. Mittal, V. V. Orre, E. A. Goldschmidt, and M. Hafezi, "Tunable quantum interference using a topological source of indistinguishable photon pairs", Nature Photonics **15**, 542–548 (2021).

[15] S. Wall, D. Brida, S. R. Clark, H. P. Ehrke, D. Jaksch, A. Ardavan, S. Bonora, H. Uemura, Y. Takahashi, T. Hasegawa, H. Okamoto, G. Cerullo, and A. Cavalleri, "Quantum interference between charge excitation paths in a solid-state mott insulator", Nature Physics **7**, 114–118 (2011).

[16] S. Barik, A. Karasahin, C. Flower, T. Cai, H. Miyake, W. DeGottardi, M. Hafezi, and E. Waks, "A topological quantum optics interface", Science **359**, 666–668 (2018).

[17] S. Popescu, "Dynamical quantum non-locality", Nature Physics **6**, 151–153 (2010).

[18] J. Chang, E. Blackburn, A. T. Holmes, N. B. Christensen, J. Larsen, J. Mesot, R. Liang, D. A. Bonn, W. N. Hardy, A. Watenphul, M. v. Zimmermann, E. M. Forgan, and S. M. Hayden, "Direct observation of competition between superconductivity and charge density wave order in $YBa_2Cu_3O_{6.67}$", Nature Physics **8**, 871–876 (2012).

[19] M. Lavagnini, L. Tassini, B. Muschler, R. Hackl, R. Monnier, J.-H. Chu, I. R. Fisher, and L. Degiorgi, "Raman scattering evidence for a cascade evolution of the charge-density-wave collective amplitude mode", Phys. Rev. B **81**, 081101 (2010).

[20] A. Kogar, A. Zong, P. E. Dolgirev, X. Shen, J. Straquadine, Y.-Q. Bie, X. Wang, T. Rohwer, I.-C. Tung, Y. Yang, R. Li, J. Yang, S. Weathersby, S. Park, M. E. Kozina, E. J. Sie, H. Wen, P. Jarillo-Herrero, I. R. Fisher, X. Wang, and N. Gedik, "Light-induced charge density wave in late3", Nature Physics **16**, 159–163 (2020).

[21] R. V. Yusupov, T. Mertelj, J.-H. Chu, I. R. Fisher, and D. Mihailovic, "Single-particle and collective mode couplings associated with 1- and 2-directional electronic ordering in metallic RTe_3 ($R = \mathrm{Ho}, \mathrm{Dy}, \mathrm{Tb}$)", Phys. Rev. Lett. **101**, 246402 (2008).

[22] H. Y. Liu, I. Gierz, J. C. Petersen, S. Kaiser, A. Simoncig, A. L. Cavalieri, C. Cacho, I. C. E. Turcu, E. Springate, F. Frassetto, L. Poletto, S. S. Dhesi, Z.-A. Xu, T. Cuk, R. Merlin, and A. Cavalleri, "Possible observation of parametrically amplified coherent phasons in $K_{0.3}MoO_3$ using time-resolved extreme-ultraviolet angle-resolved photoemission spectroscopy", Physical Review B **88**, 045104 (2013).

[23] D. A. Zocco, J. J. Hamlin, K. Grube, J.-H. Chu, H.-H. Kuo, I. R. Fisher, and M. B. Maple, "Pressure dependence of the charge-density-wave and superconducting states in $GdTe_3$, $TbTe_3$, and $DyTe_3$", Phys. Rev. B **91**, 205114 (2015).

[24] X. Xi, L. Zhao, Z. Wang, H. Berger, L. Forró, J. Shan, and K. F. Mak, "Strongly enhanced charge-density-wave order in monolayer $NbSe_2$", Nature Nanotechnology **10**, 765–769 (2015).

[25] N. Yoshikawa, H. Suganuma, H. Matsuoka, Y. Tanaka, P. Hemme, M. Cazayous, Y. Gallais, M. Nakano, Y. Iwasa, and R. Shimano, "Ultrafast switching to an insulating-like metastable state by amplitudon excitation of a charge density wave", Nature Physics, 10.1038/s41567-021-01267-3 (2021).

[26] I. Vaskivskyi, J. Gospodaric, S. Brazovskii, D. Svetin, P. Sutar, E. Goreshnik, I. A. Mihailovic, T. Mertelj, and D. Mihailovic, "Controlling the metal-to-insulator relaxation of the metastable hidden quantum state in 1T-TaS_2", Science Advances **1**, e1500168 (2015).

[27] A. Mohammadzadeh, A. Rehman, F. Kargar, S. Rumyantsev, J. M. Smulko, W. Knap, R. K. Lake, and A. A. Balandin, "Room temperature depinning of the charge-density waves in quasi-two-dimensional 1T-TaS_2 devices", Applied Physics Letters **118**, 223101 (2021).

[28] M. J. Gray, N. Kumar, R. O'Connor, M. Hoek, E. Sheridan, M. C. Doyle, M. L. Romanelli, G. B. Osterhoudt, Y. Wang, V. Plisson, S. Lei, R. Zhong, B. Rachmilowitz, H. Zhao, H. Kitadai, S. Shepard, L. M. Schoop, G. D. Gu, I. Zeljkovic, X. Ling, and K. S. Burch, "A cleanroom in a glovebox", Review of Scientific Instruments **91**, 073909 (2020).

[29] Y. Tian, A. A. Reijnders, G. B. Osterhoudt, I. Valmianski, J. G. Ramirez, C. Urban, R. Zhong, J. Schneeloch, G. Gu, I. Henslee, and K. S. Burch, "Low vibration high numerical aperture automated variable temperature raman microscope", Review of Scientific Instruments **87**, 043105 (2016).

[30] M. V. Klein, "Theory of raman scattering from charge-density-wave phonons", Phys. Rev. B **25**, 7192–7208 (1982).

[31] Y. Wang, G. B. Osterhoudt, Y. Tian, P. Lampen-Kelley, A. Banerjee, T. Goldstein, J. Yan, J. Knolle, H. Ji, R. J. Cava, J. Nasu, Y. Motome, S. E. Nagler, D. Mandrus, and K. S. Burch, "The range of non-kitaev terms and fractional particles in α-$RuCl_3$", npj Quantum Materials **5**, 14 (2020).

[32] T. P. Devereaux and R. Hackl, "Inelastic light scattering from correlated electrons", Rev. Mod. Phys. **79**, 175–233 (2007).

[33] J. Ralston, R. Wadsack, and R. Chang, "Resonant cancelation of raman scattering from cds and si", Phys. Rev. Lett. **25**, 814 (1970).

[34] M. Cardona, *Light scattering in solids 1* (Springer Berlin Heidelberg, 1975).

[35] J. A. Koningstein and O. S. Mortensen, "Electronic Raman Spectra IV: Relation between the Scattering Tensor and the Symmetry of the Crystal Field", Journal of the Optical Society of America **58**, 1208 (1968).

[36] C.-F. Chen, C.-H. Park, B. W. Boudouris, J. Horng, B. Geng, C. Girit, A. Zettl, M. F. Crommie, R. A. Segalman, S. G. Louie, and F. Wang, "Controlling inelastic light scattering quantum pathways in graphene", Nature **471**, 617–620 (2011).

[37] P. Rivera, J. R. Schaibley, A. M. Jones, J. S. Ross, S. Wu, G. Aivazian, P. Klement, K. Seyler, G. Clark, N. J. Ghimire, J. Yan, D. G. Mandrus, W. Yao, and X. Xu, "Observation of long-lived interlayer excitons in monolayer $MoSe_2$-WSe_2 heterostructures", Nature Communications **6**, 6242 (2015).

[38] J. Friedman and R. M. Hochstrasser, "Interference effects in resonance raman spectroscopy", Chemical Physics Letters **32**, 414–419 (1975).

[39] C. Chen, Y.-Y. Yin, and D. S. Elliott, "Interference between optical transitions", Phys. Rev. Lett. **64**, 507–510 (1990).

[40] C. D. Malliakas and M. G. Kanatzidis, "Divergence in the behavior of the charge density wave in $ReTe_3$ (Re = rare-earth element) with temperature and re element", Journal of the American Chemical Society **128**, 12612–12613 (2006).

[41] H.-M. Eiter, M. Lavagnini, R. Hackl, E. A. Nowadnick, A. F. Kemper, T. P. Devereaux, J.-H. Chu, J. G. Analytis, I. R. Fisher, and L. Degiorgi, "Alternative route to charge density wave formation in multiband systems", Proceedings of the National Academy of Sciences **110**, 64–69 (2013).

[42] M. Maschek, D. A. Zocco, S. Rosenkranz, R. Heid, A. H. Said, A. Alatas, P. Walmsley, I. R. Fisher, and F. Weber, "Competing soft phonon modes at the charge-density-wave transitions in $\mathrm{DyTe_3}$", Phys. Rev. B **98**, 094304 (2018).

[43] R. C. Powell, *Symmetry, group theory, and the physical properties of crystals*, Vol. 824 (Springer, 2010).

[44] Y. Chen, P. Wang, M. Wu, J. Ma, S. Wen, X. Wu, G. Li, Y. Zhao, K. Wang, L. Zhang, L. Huang, W. Li, and M. Huang, "Raman spectra and dimensional effect on the charge density wave transition in gdte3", Applied Physics Letters **115**, 151905 (2019).

[45] X.-G. Wen, "Colloquium: zoo of quantum-topological phases of matter", Rev. Mod. Phys. **89**, 041004 (2017).

[46] Z. Nussinov and J. van den Brink, "Compass models: theory and physical motivations", Rev. Mod. Phys. **87**, 1–59 (2015).

[47] K. S. Burch, D. Mandrus, and J.-G. Park, "Magnetism in two-dimensional van der waals materials", Nature **563**, 47–52 (2018).

[48] S. K. Takahashi, J. Wang, A. Arsenault, T. Imai, M. Abramchuk, F. Tafti, and P. M. Singer, "Spin Excitations of a Proximate Kitaev Quantum Spin Liquid Realized in Cu_2IrO_3", Physical Review X **9**, 031047 (2019).

[49] P. A. Lee, "An end to the drought of quantum spin liquids", Science **321**, 1306–1307 (2008).

[50] L. Savary and L. Balents, "Quantum Spin Liquids", Reports on progress in physics. Physical Society (Great Britain) **80**, 016502 (2016).

[51] T.-H. Han, J. S. Helton, S. Chu, D. G. Nocera, J. A. Rodriguez-Rivera, C. Broholm, and Y. S. Lee, "Fractionalized excitations in the spin-liquid state of a kagome-lattice antiferromagnet", Nature **492**, 406–410 (2012).

[52] A. Catuneanu, Y. Yamaji, G. Wachtel, Y. B. Kim, and H.-Y. Kee, "Path to stable quantum spin liquids in spin-orbit coupled correlated materials", npj Quantum Materials **3**, 23 (2018).

[53] L. J. Sandilands, Y. Tian, K. W. Plumb, Y.-J. Kim, and K. S. Burch, "Scattering continuum and possible fractionalized excitations in $\alpha-\mathrm{RuCl_3}$", Phys. Rev. Lett. **114**, 147201 (2015).

[54] A. Banerjee, C. A. Bridges, J.-Q. Yan, A. A. Aczel, L. Li, M. B. Stone, G. E. Granroth, M. D. Lumsden, Y. Yiu, J. Knolle, S. Bhattacharjee, D. L. Kovrizhin, R. Moessner, D. A. Tennant, D. G. Mandrus, and S. E. Nagler, "Proximate kitaev quantum spin liquid behaviour in a honeycomb magnet", Nature Materials **15**, 733–740 (2016).

[55] D. Wulferding, P. Lemmens, P. Scheib, J. R$\acute{}$oder, P. Mendels, S. Chu, T. Han, and Y. S. Lee, "Interplay of thermal and quantum spin fluctuations in the kagome lattice compound herbertsmithite", Physical Review B **82**, 144412 (2010).

[56] A. Kitaev, "Anyons in an exactly solved model and beyond", Annals of Physics **321**, 2–111 (2006).

[57] M. Vojta, A. K. Mitchell, and F. Zschocke, "Kondo impurities in the kitaev spin liquid: numerical renormalization group solution and gauge-flux-driven screening", Phys. Rev. Lett. **117**, 037202 (2016).

[58] J. Nasu, M. Udagawa, and Y. Motome, "Vaporization of kitaev spin liquids", Phys. Rev. Lett. **113**, 197205 (2014).

[59] M. Becker, M. Hermanns, B. Bauer, M. Garst, and S. Trebst, "Spin-orbit physics of $j = \frac{1}{2}$ mott insulators on the triangular lattice", Physical Review B **91**, 155135 (2015).

[60] U. F. P. Seifert, T. Meng, and M. Vojta, "Fractionalized fermi liquids and exotic superconductivity in the kitaev-kondo lattice", Phys. Rev. B **97**, 085118 (2018).

[61] K. Kitagawa, T. Takayama, Y. Matsumoto, A. Kato, R. Takano, Y. Kishimoto, S. Bette, R. Dinnebier, G. Jackeli, and H. Takagi, "A spin-orbital-entangled quantum liquid on a honeycomb lattice", Nature **554**, 341–345 (2018).

[62] G. Jackeli and G. Khaliullin, "Mott insulators in the strong spin-orbit coupling limit: from heisenberg to a quantum compass and kitaev models", Phys. Rev. Lett. **102**, 017205 (2009).

[63] Y. Singh and P. Gegenwart, "Antiferromagnetic mott insulating state in single crystals of the honeycomb lattice material Na_2IrO_3", Physical Review B **82**, 064412 (2010).

[64] M. Abramchuk, C. Ozsoy-Keskinbora, J. W. Krizan, K. R. Metz, D. C. Bell, and F. Tafti, "Cu_2IrO_3 : A New Magnetically Frustrated Honeycomb Iridate", Journal of the American Chemical Society **139**, 15371–15376 (2017).

[65] S. Matern and M. Hermanns, "Entanglement in 3d kitaev spin liquids", Journal of Statistical Mechanics: Theory and Experiment **2018**, 063101 (2018).

[66] R. Comin, G. Levy, B. Ludbrook, Z.-H. Zhu, C. N. Veenstra, J. A. Rosen, Y. Singh, P. Gegenwart, D. Stricker, J. N. Hancock, D. van der Marel, I. S. Elfimov, and A. Damascelli, "Na_2IrO_3 As a novel relativistic mott insulator with a 340-mev gap", Phys. Rev. Lett. **109**, 266406 (2012).

[67] K. Modic, T. E. Smidt, I. Kimchi, N. P. Breznay, A. Biffin, S. Choi, R. D. Johnson, R. Coldea, P. Watkins-Curry, G. T. McCandless, et al., "Realization of a three-dimensional spin–anisotropic harmonic honeycomb Iridate", Nature communications **5**, 4203 (2014).

[68] K. W. Plumb, J. P. Clancy, L. J. Sandilands, V. V. Shankar, Y. F. Hu, K. S. Burch, H.-Y. Kee, and Y.-J. Kim, "$\alpha - RuCl_3$: a spin-orbit assisted mott insulator on a honeycomb lattice", Phys. Rev. B **90**, 041112 (2014).

[69] L. J. Sandilands, C. H. Sohn, H. J. Park, S. Y. Kim, K. W. Kim, J. A. Sears, Y.-J. Kim, and T. W. Noh, "Optical probe of heisenberg-kitaev magnetism in $\alpha-RuCl_3$", Phys. Rev. B **94**, 195156 (2016).

[70] A. Glamazda, P. Lemmens, S.-H. Do, Y. S. Kwon, and K.-Y. Choi, "Relation between kitaev magnetism and structure in $\alpha - RuCl_3$", Phys. Rev. B **95**, 174429 (2017).

[71] J. Zheng, K. Ran, T. Li, J. Wang, P. Wang, B. Liu, Z.-X. Liu, B. Normand, J. Wen, and W. Yu, "Gapless spin excitations in the field-induced quantum spin liquid phase of $\alpha-RuCl_3$", Phys. Rev. Lett. **119**, 227208 (2017).

[72] H.-S. Kim and H.-Y. Kee, "Crystal structure and magnetism in $\alpha - RuCl_3$: an ab initio study", Phys. Rev. B **93**, 155143 (2016).

[73] S. M. Winter, K. Riedl, P. A. Maksimov, A. L. Chernyshev, A. Honecker, and R. Valentí, "Breakdown of magnons in a strongly spin-orbital coupled magnet", Nature Communications **8**, 1152 (2017).

[74] S.-H. Do, S.-Y. Park, J. Yoshitake, J. Nasu, Y. Motome, Y. Kwon, D. T. Adroja, D. J. Voneshen, K. Kim, T.-H. Jang, J.-H. Park, K.-Y. Choi, and S. Ji, "Majorana fermions in the kitaev quantum spin system a-rucl3", Nature Physics **13**, 1079–1084 (2017).

[75] L. J. Sandilands, Y. Tian, A. A. Reijnders, H.-S. Kim, K. W. Plumb, Y.-J. Kim, H.-Y. Kee, and K. S. Burch, "Spin-orbit excitations and electronic structure of the putative kitaev magnet $\alpha - RuCl_3$", Phys. Rev. B **93**, 075144 (2016).

[76] X. Zhou, H. Li, J. A. Waugh, S. Parham, H.-S. Kim, J. A. Sears, A. Gomes, H.-Y. Kee, Y.-J. Kim, and D. S. Dessau, "Angle-resolved photoemission study of the kitaev candidate $\alpha - RuCl_3$", Phys. Rev. B **94**, 161106 (2016).

[77] A. Koitzsch, C. Habenicht, E. Müller, M. Knupfer, B. Büchner, H. C. Kandpal, J. van den Brink, D. Nowak, A. Isaeva, and T. Doert, "J_{eff} Description of the honeycomb mott insulator $\alpha-RuCl_3$", Phys. Rev. Lett. **117**, 126403 (2016).

[78] J. Nasu, J. Knolle, D. L. Kovrizhin, Y. Motome, and R. Moessner, "Fermionic response from fractionalization in an insulating two-dimensional magnet", Nature Physics **12**, 912–915 (2016).

[79] S. Yan, D. A. Huse, and S. R. White, "Spin-liquid ground state of the s = 1/2 kagome heisenberg antiferromagnet", Science **332**, 1173–1176 (2011).

[80] J. Knolle, G.-W. Chern, D. L. Kovrizhin, R. Moessner, and N. B. Perkins, "Raman Scattering Signatures of Kitaev Spin Liquids in $A_2\mathrm{IrO}_3$ Iridates with $A = \mathrm{Na}$ or Li", Phys. Rev. Lett. **113**, 187201 (2014).

[81] J. ř. Chaloupka, G. Jackeli, and G. Khaliullin, "Kitaev-heisenberg model on a honeycomb lattice: possible exotic phases in iridium oxides $A_2\mathrm{IrO}_3$", Phys. Rev. Lett. **105**, 027204 (2010).

[82] Y. Kasahara, T. Ohnishi, Y. Mizukami, O. Tanaka, S. Ma, K. Sugii, N. Kurita, H. Tanaka, J. Nasu, Y. Motome, T. Shibauchi, and Y. Matsuda, "Majorana quantization and half-integer thermal quantum hall effect in a kitaev spin liquid", Nature **559**, 227–231 (2018).

[83] A. Banerjee, J. Yan, J. Knolle, C. A. Bridges, M. B. Stone, M. D. Lumsden, D. G. Mandrus, D. A. Tennant, R. Moessner, and S. E. Nagler, "Neutron scattering in the proximate quantum spin liquid α-rucl3", Science **356**, 1055–1059 (2017).

[84] I. Rousochatzakis, S. Kourtis, J. Knolle, R. Moessner, and N. B. Perkins, "Quantum spin liquid at finite temperature: proximate dynamics and persistent typicality", Phys. Rev. B **100**, 045117 (2019).

[85] I. A. Leahy, C. A. Pocs, P. E. Siegfried, D. Graf, S.-H. Do, K.-Y. Choi, B. Normand, and M. Lee, "Anomalous thermal conductivity and magnetic torque response in the honeycomb magnet $\alpha-\mathrm{RuCl}_3$", Phys. Rev. Lett. **118**, 187203 (2017).

[86] N. Jansa, A. Zorko, M. Gomilsek, M. Pregelj, K. W. Krämer, D. Biner, A. Biffin, C. Rüegg, M. Klanjsek, A. Banerjee, P. Lampen-Kelley, J. Knolle, C. Balz, A. A. Aczel, B. Winn, Y. Liu, D. Pajerowski, J. Yan, C. A. Bridges, A. T. Savici, B. C. Chakoumakos, M. D. Lumsden, D. A. Tennant, R. Moessner, D. G. Mandrus, and S. E. Nagler, "Observation of two types of fractional excitation in the kitaev honeycomb magnet", Nature Physics **14**, 786–790 (2018).

[87] R. Yadav, N. A. Bogdanov, V. M. Katukuri, S. Nishimoto, J. van den Brink, and L. Hozoi, "Kitaev exchange and field-induced quantum spin-liquid states in honeycomb a-rucl3", Scientific Reports **6**, 37925 (2016).

[88] Z. Wang, S. Reschke, D. Hüvonen, S.-H. Do, K.-Y. Choi, M. Gensch, U. Nagel, T. Rõõm, and A. Loidl, "Magnetic excitations and continuum of a possibly field-induced quantum spin liquid in $\alpha-\mathrm{RuCl}_3$", Phys. Rev. Lett. **119**, 227202 (2017).

[89] N. Jansa, A. Zorko, M. Gomilsek, M. Pregelj, K. W. Krämer, D. Biner, A. Biffin, C. Rüegg, and M. Klanjsek, "Observation of two types of fractional excitation in the kitaev honeycomb magnet", Nature Physics **14**, 786–790 (2018).

[90] G. F. Reiter, "Light scattering from energy fluctuations in magnetic insulators", Phys. Rev. B **13**, 169–173 (1976).

[91] P. A. Fleury and R. Loudon, "Scattering of light by one- and two-magnon excitations", Phys. Rev. **166**, 514–530 (1968).

[92] K. Kim, S. Y. Lim, J.-U. Lee, S. Lee, T. Y. Kim, K. Park, G. S. Jeon, C.-H. Park, J.-G. Park, and H. Cheong, "Suppression of magnetic ordering in xxz-type antiferromagnetic monolayer nips3", Nature Communications **10**, 345 (2019).

[93] B. Zhou, Y. Wang, G. B. Osterhoudt, P. Lampen-Kelley, D. Mandrus, R. He, K. S. Burch, and E. A. Henriksen, "Possible structural transformation and enhanced magnetic fluctuations in exfoliated α-rucl3", Journal of Physics and Chemistry of Solids **128**, Spin-Orbit Coupled Materials, 291–295 (2019).

[94] O. V. Misochko, S. Tajima, C. Urano, H. Eisaki, and S. Uchida, "Raman-scattering evidence for free spinons in the one-dimensional spin-½ chains of $\mathrm{Sr_2cuO_3}$ and $\mathrm{srcuO_2}$", Phys. Rev. B **53**, R14733–R14736 (1996).

[95] H. Kuroe, J.-i. Sasaki, T. Sekine, N. Koide, Y. Sasago, K. Uchinokura, and M. Hase, "Spin fluctuations in $\mathrm{CuGeO_3}$ probed by light scattering", Phys. Rev. B **55**, 409–415 (1997).

[96] Y. Nakamura, R. Kato, and H. Kishida, "Study of magnetic excitation in pd(dmit)2 salts by raman scattering spectroscopy", Journal of the Physical Society of Japan **84**, 044715 (2015).

[97] H. Gretarsson, N. H. Sung, M. Höppner, B. J. Kim, B. Keimer, and M. Le Tacon, "Two-magnon raman scattering and pseudospin-lattice interactions in $\mathrm{Sr_2IrO_4}$ and $\mathrm{Sr_3Ir_2O_7}$", Phys. Rev. Lett. **116**, 136401 (2016).

[98] S. M. Winter, K. Riedl, D. Kaib, R. Coldea, and R. Valentıé, "Probing $\alpha - \mathrm{RuCl_3}$ beyond magnetic order: effects of temperature and magnetic field", Phys. Rev. Lett. **120**, 077203 (2018).

[99] J. Nasu, M. Udagawa, and Y. Motome, "Thermal fractionalization of quantum spins in a kitaev model: temperature-linear specific heat and coherent transport of majorana fermions", Phys. Rev. B **92**, 115122 (2015).

[100] H. B. Cao, A. Banerjee, J.-Q. Yan, C. A. Bridges, M. D. Lumsden, D. G. Mandrus, D. A. Tennant, B. C. Chakoumakos, and S. E. Nagler, "Low-temperature crystal and magnetic structure of $\alpha - \mathrm{RuCl_3}$", Phys. Rev. B **93**, 134423 (2016).

[101] D. Hirobe, M. Sato, Y. Shiomi, H. Tanaka, and E. Saitoh, "Magnetic thermal conductivity far above the néel temperature in the kitaev-magnet candidate $\alpha-\mathrm{RuCl_3}$", Phys. Rev. B **95**, 241112 (2017).

[102] C. Wellm, J. Zeisner, A. Alfonsov, A. U. B. Wolter, M. Roslova, A. Isaeva, T. Doert, M. Vojta, B. Büchner, and V. Kataev, "Signatures of low-energy fractionalized excitations in $\alpha-\mathrm{RuCl_3}$ from field-dependent microwave absorption", Phys. Rev. B **98**, 184408 (2018).

[103] B. N. Figgis, J. Lewis, F. E. Mabbs, and G. A. Webb, "Magnetic properties of some iron(iii) and ruthenium(iii) low-spin complexes", J. Chem. Soc. A, 422–426 (1966).

[104] S. Mashhadi, D. Weber, L. M. Schoop, A. Schulz, B. V. Lotsch, M. Burghard, and K. Kern, "Electrical transport signature of the magnetic fluctuation-structure relation in α-rucl3 nanoflakes", Nano Letters **18**, 3203–3208 (2018).

[105] M. Majumder, R. S. Manna, G. Simutis, J. C. Orain, T. Dey, F. Freund, A. Jesche, R. Khasanov, P. K. Biswas, E. Bykova, N. Dubrovinskaia, L. S. Dubrovinsky, R. Yadav, L. Hozoi, S. Nishimoto, A. A. Tsirlin, and P. Gegenwart, "Breakdown of magnetic order in the pressurized kitaev iridate $\beta-\mathrm{Li_2IrO_3}$", Phys. Rev. Lett. **120**, 237202 (2018).

[106] A. Little, L. Wu, P. Lampen-Kelley, A. Banerjee, S. Patankar, D. Rees, C. A. Bridges, J.-Q. Yan, D. Mandrus, S. E. Nagler, and J. Orenstein, "Antiferromagnetic resonance and terahertz continuum in $\alpha-\mathrm{RuCl_3}$", Phys. Rev. Lett. **119**, 227201 (2017).

[107] T. P. Devereaux and R. Hackl, "Inelastic light scattering from correlated electrons", Rev. Mod. Phys. **79**, 175–233 (2007).

[108] Y. Tian, M. J. Gray, H. Ji, R. J. Cava, and K. S. Burch, "Magneto-elastic coupling in a potential ferromagnetic 2d atomic crystal", 2D Materials **3**, 025035 (2016).

[109] Y. Tian and K. S. Burch, "Automatic spike removal algorithm for raman spectra", Applied Spectroscopy **70**, PMID: 27754871, 1861–1871 (2016).

[110] P. N. Butcher and N. R. Ogg, "Fluctuation-dissipation theorems for driven nonlinear media at optical frequencies", Proceedings of the Physical Society **86**, 699–708 (1965).

[111] J. Knolle, G.-W. Chern, D. L. Kovrizhin, R. Moessner, and N. B. Perkins, "Raman scattering signatures of kitaev spin liquids in $A_2\mathrm{IrO_3}$ iridates with $A = \mathrm{Na}$ or li", Phys. Rev. Lett. **113**, 187201 (2014).

[112] Y. Kasahara, K. Sugii, T. Ohnishi, M. Shimozawa, M. Yamashita, N. Kurita, H. Tanaka, J. Nasu, Y. Motome, T. Shibauchi, and Y. Matsuda, "Unusual thermal hall effect in a kitaev spin liquid candidate $\alpha-\mathrm{RuCl_3}$", Phys. Rev. Lett. **120**, 217205 (2018).

[113] L. Wu, A. Little, E. E. Aldape, D. Rees, E. Thewalt, P. Lampen-Kelley, A. Banerjee, C. A. Bridges, J.-Q. Yan, D. Boone, S. Patankar, D. Goldhaber-Gordon, D. Mandrus, S. E. Nagler, E. Altman, and J. Orenstein, "Field evolution of magnons in $\alpha-\mathrm{RuCl_3}$ by high-resolution polarized terahertz spectroscopy", Phys. Rev. B **98**, 094425 (2018).

[114] M. Majumder, M. Schmidt, H. Rosner, A. A. Tsirlin, H. Yasuoka, and M. Baenitz, "Anisotropic $\mathrm{Ru^{3+}}4d^5$ magnetism in the $\alpha-\mathrm{RuCl_3}$ honeycomb system: susceptibility, specific heat, and zero-field nmr", Phys. Rev. B **91**, 180401 (2015).

[115] J.-U. Lee, D. Yoon, H. Kim, S. W. Lee, and H. Cheong, "Thermal conductivity of suspended pristine graphene measured by raman spectroscopy", Phys. Rev. B **83**, 081419 (2011).

[116] H. Ji, R. A. Stokes, L. D. Alegria, E. C. Blomberg, M. A. Tanatar, A. Reijnders, L. M. Schoop, T. Liang, R. Prozorov, K. S. Burch, N. P. Ong, J. R. Petta, and R. J. Cava, "A ferromagnetic insulating substrate for the epitaxial growth of topological insulators", Journal of Applied Physics **114**, 114907 (2013).

[117] D. Natelson, *Nanostructures and nanotechnology* (Cambridge University Press, 2015).

[118] M. Gonschorek, J.-F. Carlin, E. Feltin, M. Py, and N. Grandjean, "High electron mobility lattice-matched al in n/ ga n field-effect transistor heterostructures", Appl. Phys. Lett **89**, 062106 (2006).

[119] Y. Li, F. Qian, J. Xiang, and C. M. Lieber, "Nanowire electronic and optoelectronic devices", Materials today **9**, 18–27 (2006).

[120] J. S. Ross, P. Klement, A. M. Jones, N. J. Ghimire, J. Yan, D. G. Mandrus, T. Taniguchi, K. Watanabe, K. Kitamura, W. Yao, D. H. Cobden, and X. Xu, "Electrically tunable excitonic light-emitting diodes based on monolayer wse2 p–n junctions", Nature Nanotechnology **9**, 268–272 (2014).

[121] K. F. Mak and J. Shan, "Photonics and optoelectronics of 2d semiconductor transition metal dichalcogenides", Nature Photonics **10**, 216–226 (2016).

[122] M. Eriksson, S. Coppersmith, and M. Lagally, "Semiconductor quantum dot qubits", MRS Bull **38**, 794 (2013).

[123] D. C. Tsui, H. L. Stormer, and A. C. Gossard, "Two-dimensional magnetotransport in the extreme quantum limit", Phys. Rev. Lett. **48**, 1559–1562 (1982).

[124] J. Shabani, M. Kjaergaard, H. J. Suominen, Y. Kim, F. Nichele, K. Pakrouski, T. Stankevic, R. M. Lutchyn, P. Krogstrup, R. Feidenhans'l, S. Kraemer, C. Nayak, M. Troyer, C. M. Marcus, and C. J. Palmstrøm, "Two-dimensional epitaxial superconductor-semiconductor heterostructures: a platform for topological superconducting networks", Phys. Rev. B **93**, 155402 (2016).

[125] A. Pachoud, M. Jaiswal, P. K. Ang, K. P. Loh, and B. Özyilmaz, "Graphene transport at high carrier densities using a polymer electrolyte gate", EPL (Europhysics Letters) **92**, 27001 (2010).

[126] J. Ye, M. F. Craciun, M. Koshino, S. Russo, S. Inoue, H. Yuan, H. Shimotani, A. F. Morpurgo, and Y. Iwasa, "Accessing the transport properties of graphene and its multilayers at high carrier density", Proceedings of the National Academy of Sciences **108**, 13002–13006 (2011).

[127] A. Das, S. Pisana, B. Chakraborty, S. Piscanec, S. K. Saha, U. V. Waghmare, K. S. Novoselov, H. R. Krishnamurthy, A. K. Geim, A. C. Ferrari, and A. K. Sood, "Monitoring dopants by raman scattering in an electrochemically top-gated graphene transistor", Nature Nanotechnology **3**, 210–215 (2008).

[128] M. Bruna, A. K. Ott, M. Ijäs, D. Yoon, U. Sassi, and A. C. Ferrari, "Doping Dependence of the Raman Spectrum of Defected Graphene", ACS Nano **8**, 7432–7441 (2014).

[129] D. K. Efetov and P. Kim, "Controlling electron-phonon interactions in graphene at ultrahigh carrier densities", Phys. Rev. Lett. **105**, 256805 (2010).

[130] F. Chen, Q. Qing, J. Xia, J. Li, and N. Tao, "Electrochemical Gate-Controlled Charge Transport in Graphene in Ionic Liquid and Aqueous Solution", Journal of the American Chemical Society **131**, 9908–9909 (2009).

[131] A. Browning, N. Kumada, Y. Sekine, H. Irie, K. Muraki, and H. Yamamoto, "Evaluation of disorder introduced by electrolyte gating through transport measurements in graphene", Applied Physics Express **9**, 065102 (2016).

[132] C.-F. Chen, C.-H. Park, B. W. Boudouris, J. Horng, B. Geng, C. Girit, A. Zettl, M. F. Crommie, R. A. Segalman, S. G. Louie, and F. Wang, "Controlling inelastic light scattering quantum pathways in graphene", Nature **471**, 617–620 (2011).

[133] W. Zhao, P. H. Tan, J. Liu, and A. C. Ferrari, "Intercalation of few-layer graphite flakes with fecl3: raman determination of fermi level, layer by layer decoupling, and stability", Journal of the American Chemical Society **133**, 5941–5946 (2011).

[134] A. Grüneis, C. Attaccalite, A. Rubio, D. V. Vyalikh, S. L. Molodtsov, J. Fink, R. Follath, W. Eberhardt, B. Büchner, and T. Pichler, "Angle-resolved photoemission study of the graphite intercalation compound KC_8: a key to graphene", Phys. Rev. B **80**, 075431 (2009).

[135] J. A. Elias and E. A. Henriksen, "Unexpected Hole Doping of Graphene by Osmium Adatoms", Annalen der Physik **532**, 1900294 (2020).

[136] J. L. McChesney, A. Bostwick, T. Ohta, T. Seyller, K. Horn, J. González, and E. Rotenberg, "Extended van hove singularity and superconducting instability in doped graphene", Phys. Rev. Lett. **104**, 136803 (2010).

[137] X. Zhang, A. Hsu, H. Wang, Y. Song, J. Kong, M. S. Dresselhaus, and T. Palacios, "Impact of Chlorine Functionalization on High-Mobility Chemical Vapor Deposition Grown Graphene", ACS Nano **7**, 7262–7270 (2013).

[138] A. Koitzsch, C. Habenicht, E. Müller, M. Knupfer, B. Büchner, H. C. Kandpal, J. van den Brink, D. Nowak, A. Isaeva, and T. Doert, "J_{eff} Description of the honeycomb mott insulator $\alpha-\mathrm{RuCl_3}$", Phys. Rev. Lett. **117**, 126403 (2016).

[139] L. J. Sandilands, C. H. Sohn, H. J. Park, S. Y. Kim, K. W. Kim, J. A. Sears, Y.-J. Kim, and T. W. Noh, "Optical probe of heisenberg-kitaev magnetism in $\alpha-\mathrm{RuCl_3}$", Phys. Rev. B **94**, 195156 (2016).

[140] B. Zhou, J. Balgley, P. Lampen-Kelley, J.-Q. Yan, D. G. Mandrus, and E. A. Henriksen, "Evidence for charge transfer and proximate magnetism in graphene-α-$RuCl_3$heterostructures", Phys. Rev. B **100**, 165426 (2019).

[141] S. Mashhadi, D. Weber, L. M. Schoop, A. Schulz, B. V. Lotsch, M. Burghard, and K. Kern, "Electrical transport signature of the magnetic fluctuation-structure relation in α-rucl3 nanoflakes", Nano letters **18**, 3203–3208 (2018).

[142] A. Banerjee, J. Yan, J. Knolle, C. A. Bridges, M. B. Stone, M. D. Lumsden, D. G. Mandrus, D. A. Tennant, R. Moessner, and S. E. Nagler, "Neutron scattering in the proximate quantum spin liquid $\alpha-\mathrm{RuCl_3}$", Science **356**, 1055–1059 (2017).

[143] Y. Wang, G. B. Osterhoudt, Y. Tian, P. Lampen-Kelley, A. Banerjee, T. Goldstein, J. Yan, J. Knolle, H. Ji, R. J. Cava, J. Nasu, Y. Motome, S. E. Nagler, D. Mandrus, and K. S. Burch, "The range of non-Kitaev terms and fractional particles in α-RuCl3", npj Quantum Materials **5**, 14 (2020).

[144] W.-C. Lee and A. H. MacDonald, "Modulation doping near mott-insulator heterojunctions", Phys. Rev. B **74**, 075106 (2006).

[145] E. Gerber, Y. Yao, T. A. Arias, and E.-A. Kim, "Ab initio mismatched interface theory of graphene on $\alpha-\mathrm{RuCl_3}$: doping and magnetism", Phys. Rev. Lett. **124**, 106804 (2020).

[146] D. J. Rizzo, B. S. Jessen, Z. Sun, F. L. Ruta, J. Zhang, J.-Q. Yan, L. Xian, A. S. McLeod, M. E. Berkowitz, K. Watanabe, T. Taniguchi, S. E. Nagler, D. G. Mandrus, A. Rubio, M. M. Fogler, A. J. Millis, J. C. Hone, C. R. Dean, and D. N. Basov, "Charge-transfer plasmon polaritons at graphene/α-rucl3 interfaces", Nano Letters **20**, 8438–8445 (2020).

[147] S. Mashhadi, Y. Kim, J. Kim, D. Weber, T. Taniguchi, K. Watanabe, N. Park, B. Lotsch, J. H. Smet, M. Burghard, and K. Kern, "Spin-split band hybridization in graphene proximitized with α-rucl3 nanosheets", Nano Letters **19**, 4659–4665 (2019).

[148] S. Biswas, Y. Li, S. M. Winter, J. Knolle, and R. Valentıé, "Electronic properties of $\alpha-\mathrm{RuCl_3}$ in proximity to graphene", Phys. Rev. Lett. **123**, 237201 (2019).

[149] L. Wang, I. Meric, P. Y. Huang, Q. Gao, Y. Gao, H. Tran, T. Taniguchi, K. Watanabe, L. M. Campos, D. A. Muller, J. Guo, P. Kim, J. Hone, K. L. Shepard, and C. R. Dean, "One-dimensional electrical contact to a two-dimensional material", Science **342**, 614–617 (2013).

[150] A. Das, B. Chakraborty, S. Piscanec, S. Pisana, A. K. Sood, and A. C. Ferrari, "Phonon renormalization in doped bilayer graphene", Phys. Rev. B **79**, 155417 (2009).

[151] J. E. Lee, G. Ahn, J. Shim, Y. S. Lee, and S. Ryu, "Optical separation of mechanical strain from charge doping in graphene", Nature Communications **3**, 1024 (2012).

[152] S. T. Gill, J. H. Hinnefeld, S. Zhu, W. J. Swanson, T. Li, and N. Mason, "Mechanical control of graphene on engineered pyramidal strain arrays", ACS Nano **9**, 5799–5806 (2015).

[153] N. M. Gabor, J. C. W. Song, Q. Ma, N. L. Nair, T. Taychatanapat, K. Watanabe, T. Taniguchi, L. S. Levitov, and P. Jarillo-Herrero, "Hot Carrier-Assisted Intrinsic Photoresponse in Graphene", Science **334**, 648– (2011).

[154] Y. Yang, M. Li, I. Rousochatzakis, and N. B. Perkins, "Non-loudon-fleury raman scattering in spin-orbit coupled mott insulators", Phys. Rev. B **104**, 144412 (2021).

[155] G. B. Osterhoudt, Y. Wang, C. A. C. Garcia, V. M. Plisson, J. Gooth, C. Felser, P. Narang, and K. S. Burch, "Evidence for dominant phonon-electron scattering in weyl semimetal $\mathrm{WP_2}$", Phys. Rev. X **11**, 011017 (2021).

[156] A. Ruiz, A. Frano, N. P. Breznay, I. Kimchi, T. Helm, I. Oswald, J. Y. Chan, R. J. Birgeneau, Z. Islam, and J. G. Analytis, "Correlated states in β-Li2IrO3 driven by applied magnetic fields", Nature Communications **8**, 961 (2017).

[157] I. Rousochatzakis and N. B. Perkins, "Magnetic field induced evolution of intertwined orders in the Kitaev magnet $\beta-\mathrm{Li_2IrO_3}$", Phys. Rev. B **97**, 174423 (2018).

[158] S. Ducatman, I. Rousochatzakis, and N. B. Perkins, "Magnetic structure and excitation spectrum of the hyperhoneycomb Kitaev magnet $\beta-\mathrm{Li_2IrO_3}$", Phys. Rev. B **97**, 125125 (2018).

[159] A. Glamazda, P. Lemmens, S. .-. Do, Y. S. Choi, and K. .-. Choi, "Raman spectroscopic signature of fractionalized excitations in the harmonic-honeycomb iridates β- and γ-Li2IrO3", Nature Communications **7**, 12286 (2016).

[160] L. J. Sandilands, Y. Tian, K. W. Plumb, Y.-J. Kim, and K. S. Burch, Phys. Rev. Lett. **114**, 147201 (2015).

[161] M. Pregelj, O. Zaharko, U. Stuhr, A. Zorko, H. Berger, A. Prokofiev, and D. Arčon, "Coexisting spinons and magnons in the frustrated zigzag spin- 12 chain compound β-TeVO4", Physical Review B **98**, 10.1103/PhysRevB.98.094405 (2018).